Combining acoustic P- and S-wave measurements and microstructural analysis to determine the in-situ state of stress of a porous sandstone reservoir

T.E. Bosch BSc.
MSc. Thesis
26-04-2018
Earth Structure and Dynamics
Utrecht University
1st supervisor: Dr. S.J.T. Hangx
2nd supervisor: Dr. B.A. Verberne

Utrecht University

Abstract

Stress changes within a porous sandstone reservoir due to gas extraction may lead to reservoir compaction and corresponding subsidence, as observed for the Groningen gas field. Therefore, a good understanding of the field stress state is necessary for an accurate prediction of reservoir compaction. This study addresses the question if the in-situ state of stress of a porous sandstone reservoir can be determined by measuring acoustic wave velocities during true triaxial experiments. Experiments are performed on Bleurswiller sandstone (~25% porosity). P- and S-wave velocities are monitored during two loading cycles, with an initial deviatoric loading- and unloading stage (σ_{1max} = 85 MPa, $\sigma_2 = \sigma_3$ = 15 MPa), to induce permanent deformation and create a stress imprint, succeeded by hydrostatic loading- and unloading ($\sigma_{1max} = \sigma_2 = \sigma_3$ = 117 MPa). Acoustic data are combined with microstructural analysis of sectioned samples, to quantify microcrack densities and orientations before and after deformation. Whereas microcrack analysis does not show increased crack densities after the experimental procedure, extreme porosity reduction indicates pore collapse as possible responsible mechanisms for most observed inelastic deformation. During hydrostatic loading, the previously applied maximum stress is characterized by stable minimum S-wave velocity anisotropy values, together with P-wave and S-wave velocity anisotropy rate of change values showing minima approaching zero. This result indicates that the maximum stress of the applied deviatoric stress during triaxial loading can be retrieved by introducing a subsequent hydrostatic stress. Adopting the same procedure, core damage from a Rotliegend sample can be minimized during hydrostatic loading and the in-situ state of stress of the Rotliegend reservoir can be determined.

Contents

1. Introduction

1.1 Subsidence and induced seismicity of the Groningen gas field: the problem

The Groningen gas field, located in the Northern Netherlands, was discovered in 1959 and is the largest onshore natural gas field of Europe with a diameter of roughly 30 km. The hydrocarbon reservoir, the Rotliegend sandstone, has a porosity of 10-20%, a thickness of about 100 to 200 meters and lies at around 3 km depth (*Doornhof et al. 2006*). Since the onset of gas production in 1963, more than 75% of the estimated 2.800 trillion m^3 gas in place has been extracted and produced from the reservoir. This gas production is expected to continue until 2080 (*van Thienen-Visser and Breunese 2015*). However, stress changes within a porous sandstone reservoir due to gas- or oil extraction can lead to reservoir compaction and corresponding subsidence or induced seismicity, also observed in the Groningen area. Since 1963, elevation surveys recorded a maximum surface subsidence of about 32 centimeters in Loppersum, Groningen. The observed subsurface formation compaction shows a linear increase with pressure decline in the reservoir (*Doornhof et al. 2006*). Furthermore, over 1000 induced earthquakes have been recorded in the Groningen area. Surface subsidence and induced seismicity are of main concern for oil- and gas industries due to the impact on the environment and society. Consequently, the topic of reservoir deformation has become extremely popular, resulting in a substantial increase of our knowledge.

1.2 Reservoir state of stress and compaction

A reservoir within the subsurface carries a substantial amount of weight due to overlying sediments, which increases with depth. Not only solid rock supports stresses caused by the overburden, pressurized fluid within the pores of the rock also supports a substantial amount of the overburden pressure (*Doornhof et al. 2006*). Therefore, the stress affecting the behaviour of a solid material depends on the vertical overburden stress and the pore fluid pressure, defined as the compressive vertical effective stress $\sigma_e = \sigma_v - P_f$. Gas production can lead to changes in the effective stress state of the porous reservoir. During production, the gas pressure in the pores decreases whereas the overburden stress stays constant, leading to an increase in the compressive vertical effective stress σ_e of the reservoir.

Under compressive stresses, microcracks and pore spaces present in the rock can be elastically closed. Both pores and microcracks can be sites where tensile stress concentrations occur when an overall compressive stress is applied (*Wong and Baud 2012*). When the compressive stress becomes high enough, new crack damage is generated by inelastic processes and permanent deformation of the rock can occur (*Browning et al. 2017*). Microstructural observations and recorded audible acoustic emissions of sandstones deformed at high stresses support the role of grain fracturing during enhanced compaction (*Brzesowsky 1995; Hangx et al. 2010; Hol et al. 2015*). Besides grain breakage, other mechanisms operating on grain-scale can also play an important role on the time-independent compaction behaviour of sandstone, involving grain rearrangement coupled with elastic deformation (*Brzesowsky 1995*). Consequently, addressed changes in the reservoir properties can lead to reservoir compaction. Compaction is observed for the Groningen gas field, with a vertical reservoir stress of ~65 MPa and a gas pressure decrease from ~35 MPa to ~8 MPa after roughly 55 years of gas production (*Spiers et al. 2017*). Reservoir compaction can express itself as surface subsidence and can furthermore lead to slip along faults due to shear stress changes, leading to seismic events (*van Thienen-Visser and Breunese 2015*).

1.3 Research question: in-situ state of stress determination by P- and S-wave monitoring

Rock density changes can be monitored by looking at the velocity of acoustic P- and S-waves. Their velocity in sandstones vary strongly with stress due to discontinuities within the rock, such as pores, microcracks and grain boundaries (*Sayers 2002*). Acoustic velocities are mostly influenced by two competitive mechanisms: the formation of microcracks and porosity reduction (*Fortin et al. 2007*). For example, grain crushing and porosity reduction can lead to velocity increase due to an increased number of highly stresses point-to-point grain contacts, whereas fracturing can cause velocities to decrease *(Scott et al. 1993*). Additionally, anisotropy in the applied stress field creates microcracks with a preferred orientation parallel to the maximum applied stress. Therefore, changes in ultrasonic wave velocities greatly depend on the applied stress field creating a very useful tool for studying microcrack formation and closure in sandstones (*Sayers et al 1990*).

Intensive work has been done on many aspects relating to reservoir compaction, including operating time-dependent and time-independent mechanisms (*e.g. Hol et al. 2015*) and the effect of chemical environment, grain size and effective stress (*e.g. Brzesowsky et al. 2014; Schutjens 1991*). Nevertheless, more research is needed to improve our understanding of reservoir deformation and production-induced surface subsidence and seismicity. Research is currently being undertaken to understand the processes controlling reservoir compaction and driving induced seismicity (*Spiers et al, 2017*). *Hettema et al.* (*2000*) concluded that compaction behaviour of sandstone reservoirs greatly depends on the horizontal stress development during depletion. To further improve gas field management and to improve future predictions related to reservoir compaction, a more comprehensive and well based understanding of the field state of stress is necessary.

Upon retrieval of rock samples from the subsurface, rapid changes in the stress state acting on the material can lead to the opening of cracks, resulting in so-called 'core-damage'. The main objective of this study is to investigate if the in-situ state of stress of a reservoir can be determined by measuring P- and S-wave velocities during true triaxial experiments, as the imposed stress on the sample is increased, thereby removing pre-existing core damage. This will be done by combining acoustic wave measurements during triaxial loading with microstructural analysis. Since samples of the Groningen Rotliegend reservoir are valuable, the approach will be tested on analogue material of the porous Bleurswiller sandstone (porosity ~25%). First, we will address the question if acoustic wave measurements during triaxial experiments can be used to reveal the previously imposed state of stress of the sample. True triaxial experiments together with monitoring P- and S-wave velocities will be performed in two main steps: (1) simulating core damage by inducing permanent rock deformation at known conditions during deviatoric loading, followed by (2) the application of a hydrostatic load to retrieve the previous maximum applied stress. Subsequently, we will combine the acoustic data with microstructural analysis to obtain more information about microcrack densities and orientations prior to- and after deformation. Ultimately, we will address the question if the results can contribute to our knowledge of the in-situ state of stress of the Rotliegend sandstone.

2. Methodology

Sample material was obtained from a large block of Bleurswiller sandstone, originating from the Vosges mountain in Eastern France (*Baud et al. 2015*) with a porosity of ~25% comparable to the Rotliegend sandstone of the Slochteren reservoir. Multiple experimental studies on mechanical compaction have been performed on the Bleurswiller sandstone. In the study by *Baud et al.* (*2015*), two different blocks of Bleurswiller sandstone are being used, showing variations in both porosity (with average values between 23.0 and 25.3%), grain size and mineral composition (mostly quartz, feldspar and clay). Other authors also recorded varying rock properties (*e.g. Fortin et al. 2007; Fortin et al. 2005*). Since our ultimate goal is to have the data contributing to our knowledge of the in-situ state of stress of the Rotliegend sandstone, a clear image of the exact porosity, average grain size and distributed mineral composition of the tested Bleurswiller samples is desired to generate a good comparison between the two rock types. Additionally, before performing the true triaxial experiments, separate test experiments are performed to determine the moment of failure of the specific Bleurswiller samples to construct suitable stress paths.

2.1 Material description: composition, grain size and porosity

Average grain size of the Bleurswiller sandstone is determined via optical microscopy, together with the mineral composition. To ensure that possible heterogeneity of the sample will be taken into account, thin sections of multiple Bleurswiller samples are analysed and both the average grain size and mineral composition are determined over a broad sample area. The identified mineral composition is afterwards compared with results obtained by X-ray diffraction (XRD) analysis to verify and specify the observed composition. Porosity is calculated using the Saturation method suggested by the International Society of Rock Mechanics (*ISRM 1979*), by determination of the difference between a saturated specimen and it's oven-dry mass. The saturated mass, M_{sat}, is determined by saturating the sample with water immersion in a vacuum, followed by oven-drying the specimen at 50°C to determine the dry mass, M_{dry}. The dry- and wet mass of each sample is measured three times and eventually averaged, to ensure a more accurate porosity determination. Subsequently, porosity is expressed as the mass difference between saturated and dried specimens, per unit weight of water:

$$\varphi = \frac{(M_{sat} - M_{dry})}{V_{sample} \cdot \rho_{water}} \cdot 100\% \qquad (1)$$

The porosity of four cubic and six cylindrical samples, all originating from the same block of Bleurswiller sandstone, are measured and listed in **Table 1**. With an average porosity of ~24,4%, the values are in the same range as porosities reported by *Fortin et al.* (*2007*) and *Baud et al.* (*2015*) of around ~23.0 - 25.3%. Thin section analysis of an undeformed Bleurswiller sample (BW-00) shows that, similar to observations done by *Fortin et al.* (*2005*) and *Baud et al.* (*2015*), pore space is heterogeneous distributed throughout the sample and porosity clusters are present. The grain matrix has a relatively homogeneous composition with locally well-cemented quartz and feldspar grains, and a small amount of clay- and mica lamina. Grains are subrounded- to angular in shape and fairly uniform in size, mostly in the range of 0.15 – 0.25 mm. This is in agreement with observations done by *Baud et al.* (*2015*) and *Fortin et al.* (*2007*), listing grain sizes in the range of 0.08 – 0.22 mm. Quartz is most abundant throughout the thin section, occasionally containing intragranular cracks. Feldspar is also abundant and is mostly present in an extremely altered form,

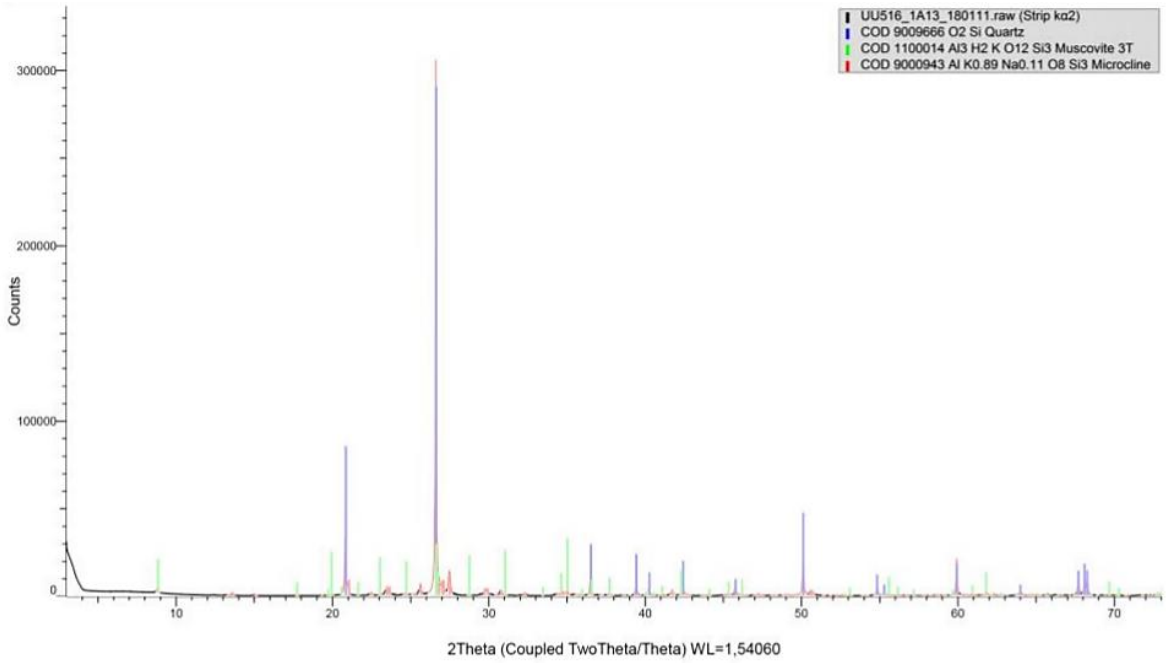

Figure 1. *XRD results of the Bleurswiller sandstone, indicating quartz, feldspar (microcline) and clay as the most abundant minerals.*

sometimes creating secondary macropores due to grain dissolution. Their original grain boundaries are occasionally still present as Fe-oxide rims. Clay particles and Fe-oxide are present in small amounts in the pore spaces. Performed X-Ray diffraction (XRD) analysis of the mineral phases present in the Bleurswiller sandstone confirms the composition observed in thin section of mainly quartz, feldspar (microcline) and clays (**Figure 1**). Since XRD analysis is not suitable for quantitative measurements, the amount of each mineral present is estimated during thin section analysis and listed in **Table 1**.

2.2 Conventional triaxial experiments

Before performing the true triaxial experiments at the Christian-Albrechts University of Kiel, separate experiments were performed at Utrecht University with the help of Dr. S.J.T. Hangx and L.B. Hunfeld MSc. at the High Pressure and Temperature Laboratory. Experiments were conducted to quantify the failure strength of dry- and wet Bleurswiller samples (respectively samples BW-06 and BW-10) under the conditions employed during the true triaxial experiments. Additionally, microstructural analysis is performed on both samples, to observe differences in microstructures between experimentally dry- and

Property	Value
Average porosity	24.0 – 24.7%
Mineral composition	50% qtz, 35% fspar, 12% micas/clays, 3% Fe-oxide
Average grain size	~0.15 - 0.25 mm

Table 1. *Bleurswiller sandstone properties. Average porosity is calculated using the Saturation method (ISRM, 1979), mineral composition and average grain size are estimated during microstructural analysis.*

wet deformed samples. A detailed description of the triaxial apparatus is given by *Peach and Spiers* (*1996*) and others (*e.g. Hangx et al. 2010*).

2.2.1 Experimental setup

As described by *Hangx et al.* (*2010*), the triaxial machine consists of a furnace-clad main pressure vessel, containing a cylindrical sample, a linked auxiliary pressure vessel and a yoke/piston loading assembly which is driven by a motor/gearbox/ball-screw arrangement (**Figure 2**). The machine is externally heated and as confining medium, silicon oil is used. The sample volume change is measured using a linear potentiometer, recording the piston displacement of a servo-controlled volumometer pump connected to both pressure vessels. The confining pressure is measured using a Jensen pressure transducer (100 MPa range; resolution ±0.02 MPa). A differential variable reluctance transformer (DVRT)-based, semi internal load cell at the top of the vessel measures the axial load (400 kN range; resolution ±0.035 kN). Furthermore, the piston displacement is measured at the yoke using a high-precision linear variable differential transformer (LVDT; 100 mm range, resolution ±0.8µm). Pressure was measured using a diaphragm-type transducer, of 100 MPa full scale, and servo-controlled to 0.01 MPa (±0.005 MPa) by the volumometer system (*Hangx et al. 2010*). Temperature is controlled using a PID (proportional-/integral/derivative) process controller (resolution, ±0.02°C; 400°C range) and a thermocouple situated in the external furnace's windings. The sample temperature is measured midway along the sample surface using two K-type thermocouples. During the wet experiment, pore fluid pressure is introduced into the sample. The fluid enters the sample via ports in the load cell block, using tubes connected to inlets at the top and bottom of the sample assembly. A volumometer pump and linear potentiometer record piston displacement and pore volume changes (*Hangx et al. 2010*). Pore fluid pressure was again measured using a Jensen pressure transducer (50 MPa range; resolution, ±0.02 MPa).

2.2.2 Sample assembly

Experiments were performed on two cylindrical shaped samples of 24,7 mm in diameter and ~70 mm in length. The cylindrical surfaces were polished to obtain parallelism, reducing friction and minimalizing uneven load distribution during the experimental procedure. Before being placed in between the two pistons, samples were jacketed using an inner- and an outer plastic sleeve sealed against the top and bottom pistons, to reduce the risk of rupture during deformation and to prevent pore fluid from leaking. Thin

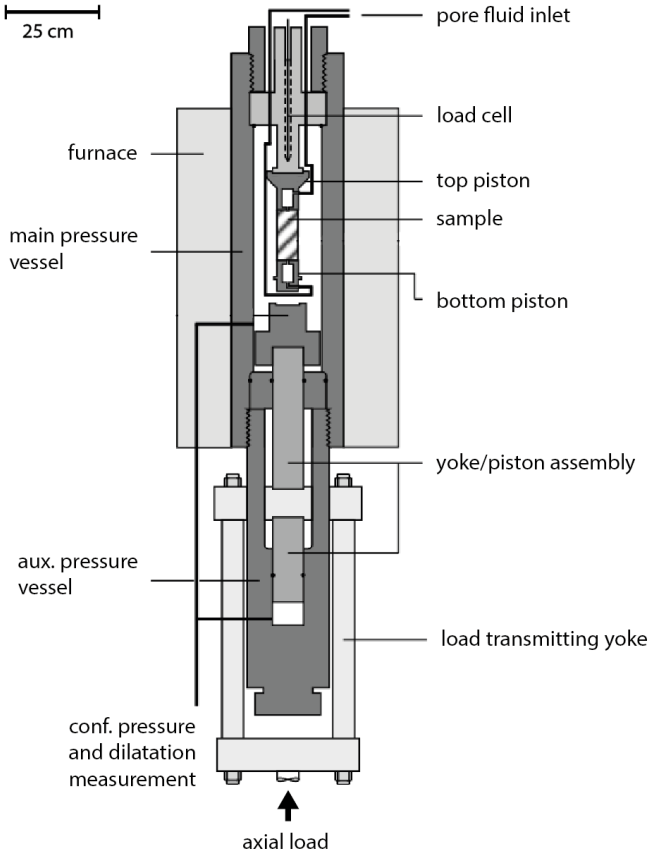

***Figure 2**. Heard triaxial apparatus experimental set-up, after Hangx et al. (2010).*

Teflon sheets were placed between the sample and the piston surfaces, to reduce the effect of friction. During the wet experiment, the Teflon sheets were perforated to permit pore fluid to enter the sample and pore pressure was kept constant at a value of ~10 MPa.

2.2.3 Experimental procedure

To determine the moment of failure and to construct suitable stress paths for the true triaxial experiments, conventional triaxial loading experiments are performed on dry- and wet Bleurswiller samples at room temperature. After placing the sample in the apparatus, the pistons are brought in position by slowly moving them towards the sample until contact between the pistons and sample is observed. From this point, the experimental procedure begins. During loading, the applied force is slowly increased leading to an increase in applied stress. Since the confining pressure is kept at a constant value, differential stress ($\sigma_1 - \sigma_3$) also increases. The effective confining pressure ($\sigma_3 - P_f$) was set at a value of 15 MPa, representing the effective horizontal stress before depletion based on a stress path analysis of the Groningen field performed by *Hettema et al.* (*2000*). This value will also be used as the effective pressures in the true triaxial experiments performed in Kiel. During the wet experiments, pore pressure was kept constant at a value of ~10 MPa. During the experimental procedure, differential stress was increased with a strain rate of 10^{-5} s^{-1} until a large strain drop was observed and sample failure occurred. After failure, the sample was unloaded and prepared for microstructural analysis.

2.2.4 Data acquisition and processing

Piston displacement is measured and used as reference for the sample axial length change, whereas measured internal load represents axial compressive stress σ_1. Since confining pressure and pore fluid pressure were maintained constant, changing oil volume or pore fluid volume are representative of the volumetric change of the sample. Signals were logged at time intervals of 0.1s (dry) and 0.5s (wet), using a PC equipped with a 16 bit National Instruments VI Logger system (*Hangx et al. 2010*). The procedure was first applied to an oven-dried Bleurswiller sample and repeated with a wet sample, using a fixed pore pressure of 10 MPa and confining pressure of 25 MPa to keep 15 MPa effective pressure.

After the experimental procedure and before final processing of the results, apparatus corrections for the volumetric distortion and the apparatus stiffness must be taken into account. During the triaxial loading experiments, sample deformation is accompanied by minor elastic apparatus deformation. Calibrations have been done on the Heard Triaxial apparatus at 15 MPa (January 2015), showing a linear trend of both volume change (mL) and apparatus distortion (mm) with increasing internal force (kN) at room temperature. Therefore, measured volume- and displacement changes must be corrected to exclude any apparatus distortion and volume changes are additionally corrected to include influences of temperature fluctuation. Subsequently, all corrected output values are normalized with respect to starting values and are eventually processed to yield the differential stress, axial strain and volumetric strain. Differential stress ($\sigma_1 - \sigma_1$) can be calculated by dividing the normalized Internal Load by the sample area F_{int}/A. Axial strain is calculated by dividing sample axial length changes by the original sample length, $\Delta X/L_0$, and volumetric strain by dividing volumetric changes of the sample by the original sample volume, $\Delta V/V_0$.

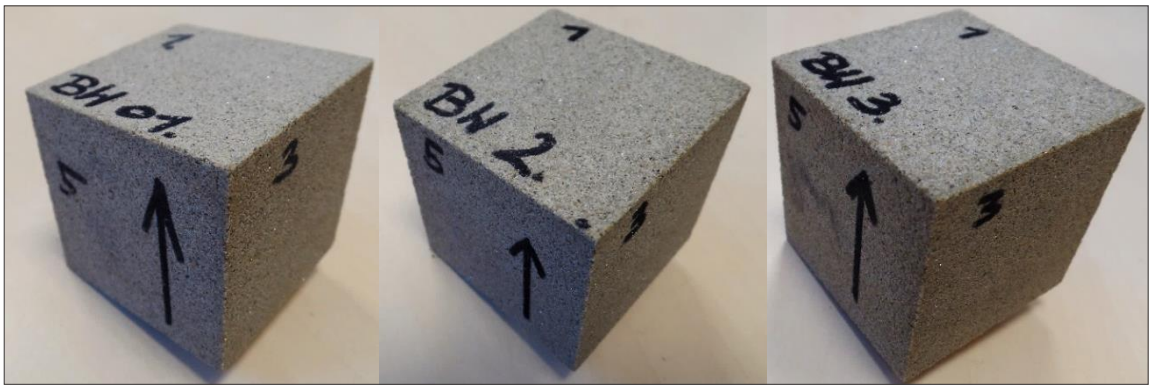

Figure 3. *Cubic samples BW-01, BW-02 and BW-03, used for the experimental procedure in the multianvil apparatus at the Christian-Albrechts University. All cubes have a diameter of ~43 mm, arrows indicate the bedding direction.*

2.3 True triaxial experiments

True triaxial experiments in a multi-anvil apparatus are performed at the Christian-Albrechts University of Kiel, under supervision and guidance of Dr. H. Bahadur Motra. The experiments in this study will build upon the proof of concept tests on low porosity (6%) Beberthal sandstone (MSc research performed by *A. Rachmi Trahwiwit, 2017*). Detailed description of the apparatus is given by *Kern et al.* (*1997*). During the experimental procedure, P- and S- wave travel times are monitored and velocities are calculated to provide information about rock density changes.

2.3.1 Triaxial apparatus description Christian-Albrechts University of Kiel: experimental setup

The multianvil pressure apparatus with piston-sample-transducer arrangement is described by *Kern* (*1982*). In the apparatus, six pyramidal pistons in three orthogonal directions can be pressed against a cubic sample to achieve the desired state of stress. Temperature is measured using thermocouples, situated at the end of each piston close to the specimen, and the opposite side of each piston is water-cooled (*Kern and Fakhimi 1975*). From the piston displacement, additional length and volume changes are obtained and are further used for strain values to quantify the sample deformation (*Kern 2011*). The precision of the time measurements is ~5ns, and the accuracy is believed to be ~0.5% (*Kern and Wenk 1990*). Pressure in all main directions can reach values up to 600 MPa and temperature can be increased up to 700 °C.

2.3.2 Sample assembly

Bleurswiller samples are cut into cubes with a diameter of 43 mm (**Figure 3**) and are coated with graphite to maximize the piston-sample contact and increase conductivity. They are oven-dried for several hours and subsequently rested for a few days outside the oven. The cubes are placed in between the six pistons of the triaxial apparatus with the sedimentary bedding perpendicular to the maximum principal stress, σ_1. To minimalize uneven load distribution during the experimental procedure, the sample is levelled with the pistons to obtain parallelism.

2.3.3 Acoustic P- and S-wave velocity measurements

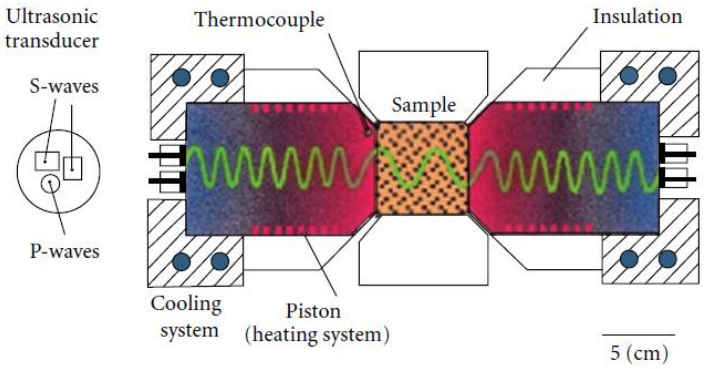

Figure 4. *The piston-sample-transducer arrangement of the multianvil apparatus in Kiel (Kern 2011).*

The piston-sample-transducer arrangement of the multi-anvil apparatus, illustrated in **Figure 4**, allows simultaneous P- and S- wave travel time measurements and directional differences in all three principal directions (X. Y and Z). During the experiments, S- and P-wave travel times will be measured at each stress step using the ultrasonic pulse transmission technique with ultrasonic transducers operating at 2 MHz for P-waves and at 1 MHz for S-waves (*Kern 1997*). A voltage pulse is applied to a circular polarized barium titanate ceramic transducer plate of 20 mm in diameter. The pulse is transmitted through the piston, sample and the subsequent coaxial piston. A receiver transducer converts the mechanical signal to a pulse which is amplified and eventually displayed on an oscilloscope. The pulse travel time through the sample is retrieved from the difference between the time needed for the pulse to travel through the pistons to- and from the sample, and the total time measured by the transducers. Velocity measurements are believed to be accurate within ~1.0% and are corrected for changes in sample length with pressure and temperature (*Kern and Wenk 1990*).

Initial velocity anisotropy and induced changes in wave velocity of the sample have to be taken into account. Therefore, all measurements are simultaneously carried out in the three principal stress directions. These directions are indicated as X, Y and Z, with the Z-direction normal to the bedding (i.e. parallel to σ_1) and the X- and Y-directions orthogonal to the normal and each other (i.e. σ_2 and σ_3, respectively, see **Figure 5**). The polarization of S- waves in two directions (referred to as shear wave splitting) is measured for each propagation direction by two sets of oriented transducers with perpendicular planes (*Kern 1997*). Therefore, velocity measurements will consist of three P-wave velocities denoted as Vp_i, and six S-wave velocities denoted as Vs_{ij} (**Figure 5**). The first subscript, i, indicates the direction of the wave propagation, whereas j indicates the S-wave polarization direction.

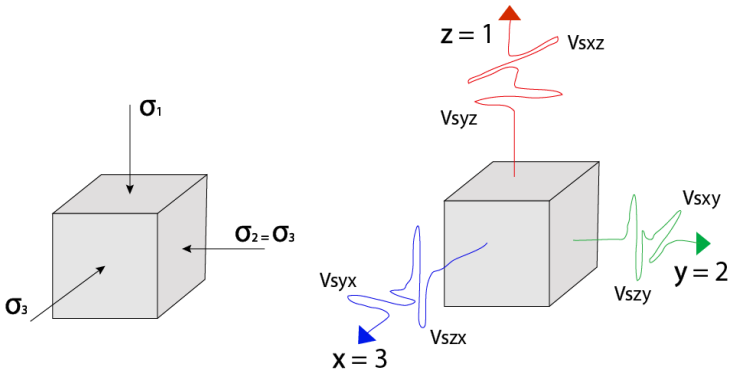

Figure 5. *Reference system of the true triaxial experiments and corresponding direction-dependent velocity measurements in the cubic samples, based on Kern (2011).*

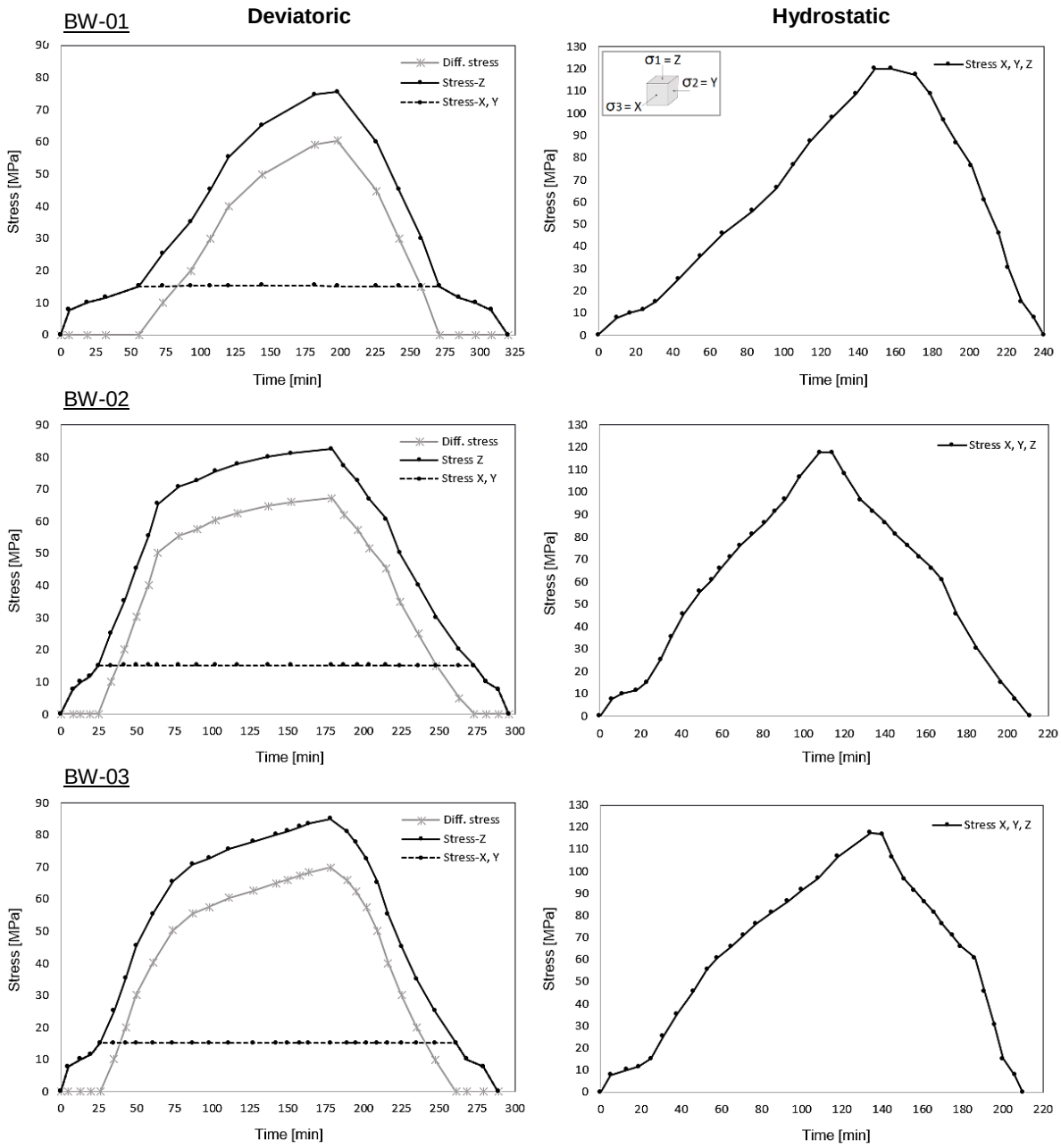

Figure 6. *Stress paths for samples BW-01, BW-02 and BW-03. Left: deviatoric loading- and unloading whereas $\sigma_1 > \sigma_2 = \sigma_3$. Right: subsequent hydrostatic unloading and unloading with $\sigma_1 = \sigma_2 = \sigma_3$.*

2.3.4 Experimental procedure

Similarly to previous experiments performed by *A. Rachmi Trahwiwit* (*2017*), each experiment will be performed in two main steps and will be repeated on three cubic samples. A suitable stress path was determined by previously described conventional triaxial loading at Utrecht University. Before starting the experimental procedure, the pistons are slowly displaced and brought into position, until contact between all pistons and the sample is observed. After the sample is levelled, the experimental procedure begins. The first experimental step includes deviatoric loading of the sample, to induce permanent deformation by

opening of new microcracks, without inducing failure. Preceding the deviatoric loading step, the sample will be brought back to 15 MPa hydrostatic stress. A near-hydrostatic stress state can be achieved by pressing six pistons simultaneously in three orthogonal directions onto the cubic samples (*Kern 1997*) exerting three equal principal stresses (σ_1, σ_2 and σ_3). The value of 15 MPa is reached by increasing the pressure in four steps of ~2-3 MPa. After reaching a near-hydrostatic stress state, a deviatoric stress ($\sigma_1 > \sigma_2 = \sigma_3$) will be exerted on the sample. During this stage, σ_2 and σ_3 will be kept at 15 MPa, whereas σ_1 will be slowly to obtain higher differential stress. The deviatoric loading stage is followed by an unloading stage, first reducing σ_1 to 15 MPa in multiple steps, followed by full unloading of all principal stresses to 0 MPa. After deviatoric unloading, the second main step includes hydrostatic loading. During hydrostatic loading, all three principal stresses are simultaneously increased ($\sigma_1 = \sigma_2 = \sigma_3$) towards values exceeding previous applied maximum stress, again followed by complete unloading after reaching its maximum assigned value. During both the deviatoric- and hydrostatic stages, pressure is increased stepwise. The stress paths used for each sample somewhat differ from each other but follow roughly the same trend (**Figure 6**).

2.3.5 Data acquisition and processing

Maximum and minimum principal stresses of the conventional triaxial experiments are denoted as σ_1 and σ_3, respectively, with σ_2 and σ_3 being equal to the confining pressure P_c and differential stress $Q = \sigma_1 - \sigma_3$. During the experimental procedure, sample length and volume changes are obtained by measuring the piston displacement in all principal directions. Pressure and piston displacement signals were logged at time intervals of 1.0s and are further corrected for apparatus stiffness and distortion (*Kern 2011*). Sample length changes in all directions at the end of each stress step are used for calculating linear strains in the X, Y and Z directions ($\Delta X/L_0$). Volumetric strains are calculated as $(V_0 - \Delta V) / V_0 * 100$ (%), with ΔV being all three axial strains multiplied. The travel times of the P- and S-waves through the sample in all principal directions are measured at the end of each stress step. After stress is increased or decreased with several MPa, sample displacement has to reach stable values (creep is minimalized) before the P- and S-wave travel times are recorded. Pulse travel times are corrected to the travel time through the pistons by calculating the time it needs to travel through a steel column of known length (*Kern and Fakhimi 1975*) and are further corrected for changes in sample length with pressure and temperature (*Kern and Wenk 1990*). From the corrected travel times, P- and S-wave velocities can be calculated by dividing the distanced travelled through the sample by the measured travel time ($\Delta x/\Delta t$). Strain measurements reveal the amount of deformation in each sample during loading- and unloading, whereas P- and S-wave measurements are used to track rock density changes.

Besides direct monitoring of P- and S-wave velocities, new insights can be obtained by combining P- and S-wave velocity data in all structural directions. Since wave velocities are measured along three orthogonal directions and all cubic samples are oriented in the same way, the velocity anisotropy evolution throughout the experiment can be visualised. P-wave velocity anisotropy (A-Vp) is defined by the percent differences between maximum and minimum velocity with respect to mean velocity, and calculated as $(V_{max} - V_{min})/V_{av} * 100$ (*Kern 2011; Kern and Wenk 1990*) . Anisotropy can also be calculated for the splitted shear waves, whereas the S-wave anisotropy in one principal direction (A-Vs X, A-Vs Y and AVs-Z) can be defined as the percent difference between the splitted shear waves with respect to the mean velocity in that direction (e.g.

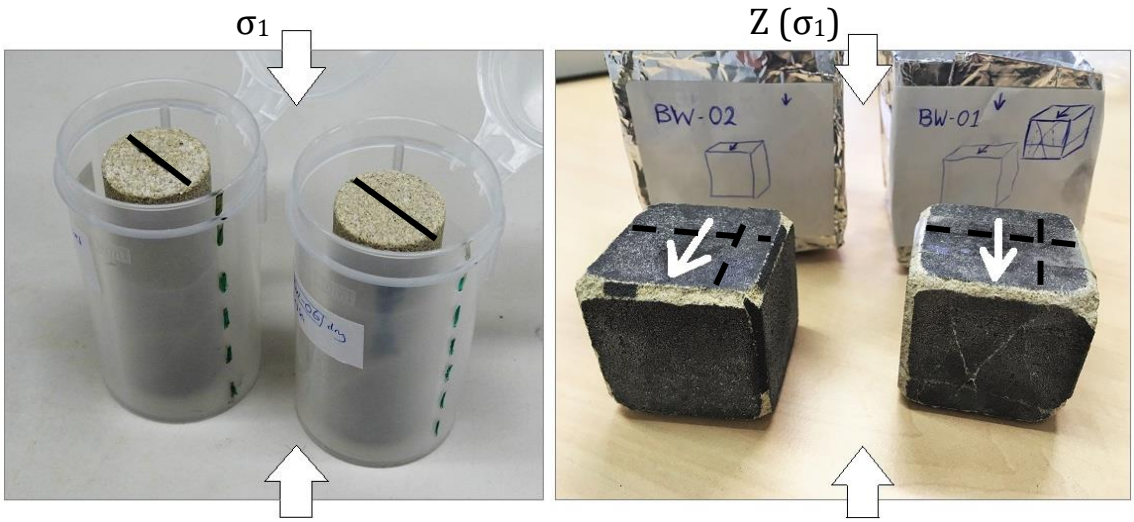

Figure 7. *Experimentally deformed samples prior to impregnation. The large white arrows indicate the compression direction σ_1, with a) conventional triaxially deformed samples BW-10 (left) and BW-06 (right) with the black line representing thin section orientation perpendicular to σ_1, and b) true triaxially deformed samples BW-02 (left) and BW (right), with the black line representing thin section orientation in two directions perpendicular to each other and to σ_1. During impregnation, Araldite resin was poured around the samples leaving ~0.5 of the top uncovered.*

*A-Vs X = (ΔVs-X)/Vs-X_{av} * 100*). Furthermore, the rate at which this velocity anisotropy changes during each stress step can be calculated, providing information about the speed at which the A-Vp and A-Vs in the sample increase or decrease. The anisotropy rate of change is *A-V/Δσ_1* (%/MPa).

2.4 Microstructural analysis

Microstructural analysis has been performed using the Leica DRX polarizing light microscope with image analysis QWIN Pro, at Utrecht University. The microstructural results will be coupled to the experimental results to quantify microcrack densities of the samples prior to- and after deformation, and to derive microcrack orientations.

2.4.1 Thin section preparation

Experimentally deformed and undeformed Bleurswiller samples were impregnated using Araldite 2020 epoxy resin. Mixing of two Araldite components (ratio 1 : 0.3 of respectively component A : B) is done in a beaker placed on a 30°C hotplate, lowering the viscosity of the liquid. Subsequently, the Araldite resin is mixed with OilBlue pigment (using 1.5 g pigment per 100 mL Araldite) to enhance contrast between pore space and grain frameworks in the sectioned sample using transmitted light in a light microscope. Samples were placed in plastic- or aluminium cups and resin was poured around the samples leaving ~0.5 of the top uncovered (**Figure 7**). After rapidly placing them in a vacuum-oven for ~10-15 minutes to stimulate penetration of the Araldite in the sample pores, sample were complete covered with Araldite resin.

After the samples were air-dried for about three to four days, thin section (~30 μm thick) were prepared at the Rock Preparation lab of Utrecht University and of the University of Southampton. All prepared sections are oriented perpendicular to the experimental σ_1 direction of the conventional triaxial

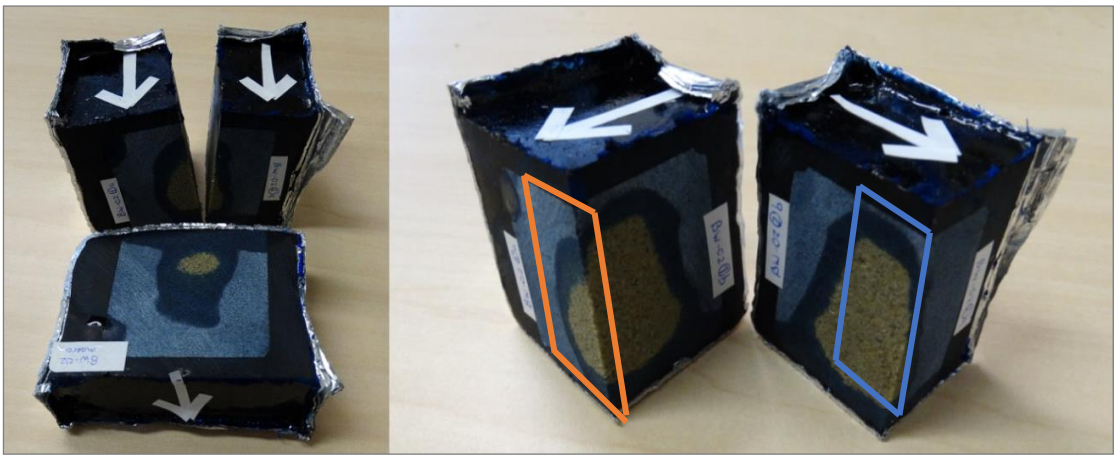

Figure 8. *Sample BW-02, cut into three pieces after a first impregnation attempt. The white arrows correspond to the white arrows indicated in* ***Figure 7****. Chosen surfaces for further thin section analysis are indicated: BW-02-1-a (red) and BW-02-2-b (blue), oriented perpendicular to each other and to the experimental Z-direction.*

experiments, corresponding to the experimental Z-direction during the true triaxial experiments. One section has been prepared of both the conventional triaxially deformed samples BW-06 and BW-10, whereas two sections were made of each true triaxially deformed sample (BW-01 and BW-02). After cutting the cubic BW-02 sample, two surfaces are chosen which are oriented perpendicular to the sample bedding (and experimental Z-direction) and parallel to the experimental X- and Y-directions. The interior of the cube reveals that the Araldite resin did not penetrated the entire sample and therefore the chosen surfaces were further impregnated. After maximum impregnation was obtained, two sections BW-02-1-a and BW-02-2-b were prepared (**Figure 8**). In a similar way, thin sections of sample BW-01 are constructed (**Figure 9**).

Figure 9. *Sample BW-01, cut after a first impregnation attempt. The white arrows correspond to the white arrows indicated in* ***Figure 7****. Chosen surfaces for further thin section analysis are indicated: BW-01-1-a (red) and BW-01-2-b (blue), oriented perpendicular to each other and to the experimental Z-direction.*

2.4.2 Acquisition and pre-processing of optical microscopy images

Optical microscopic images of all sections are obtained using the Leica DRX polarizing light microscope with image analysis QWIN Pro, at Utrecht University. Images are acquired in the centre of the prepared sections or at specific regions of interest (e.g. around fault planes), avoiding sample boundaries where possible damage is produced during thin section preparation. Image mosaics have been made by recording multiple thin section images at a 5x magnification with 25% horizontal- and 33% vertical overlap between the images, which are subsequently stitched using the open Microsoft software *Image Composite Editor* to create a final two-dimensional image mosaic over a disclosed area of known size. When unwanted shadows are present in the mosaic due to uneven lightning, mosaics are pre-processed using the *'subtract background'* function of open source image processing software *ImageJ (Schindelin et al. 2012)*. The function removes smooth continuous background from images based on the "rolling ball" algorithm (light background, using a radius of 30.0 pixels), creating a uniform background which can be used for further analysis (**Figure 10**). Using the *'color threshold'* function (Default method, B&W threshold colour and HSB

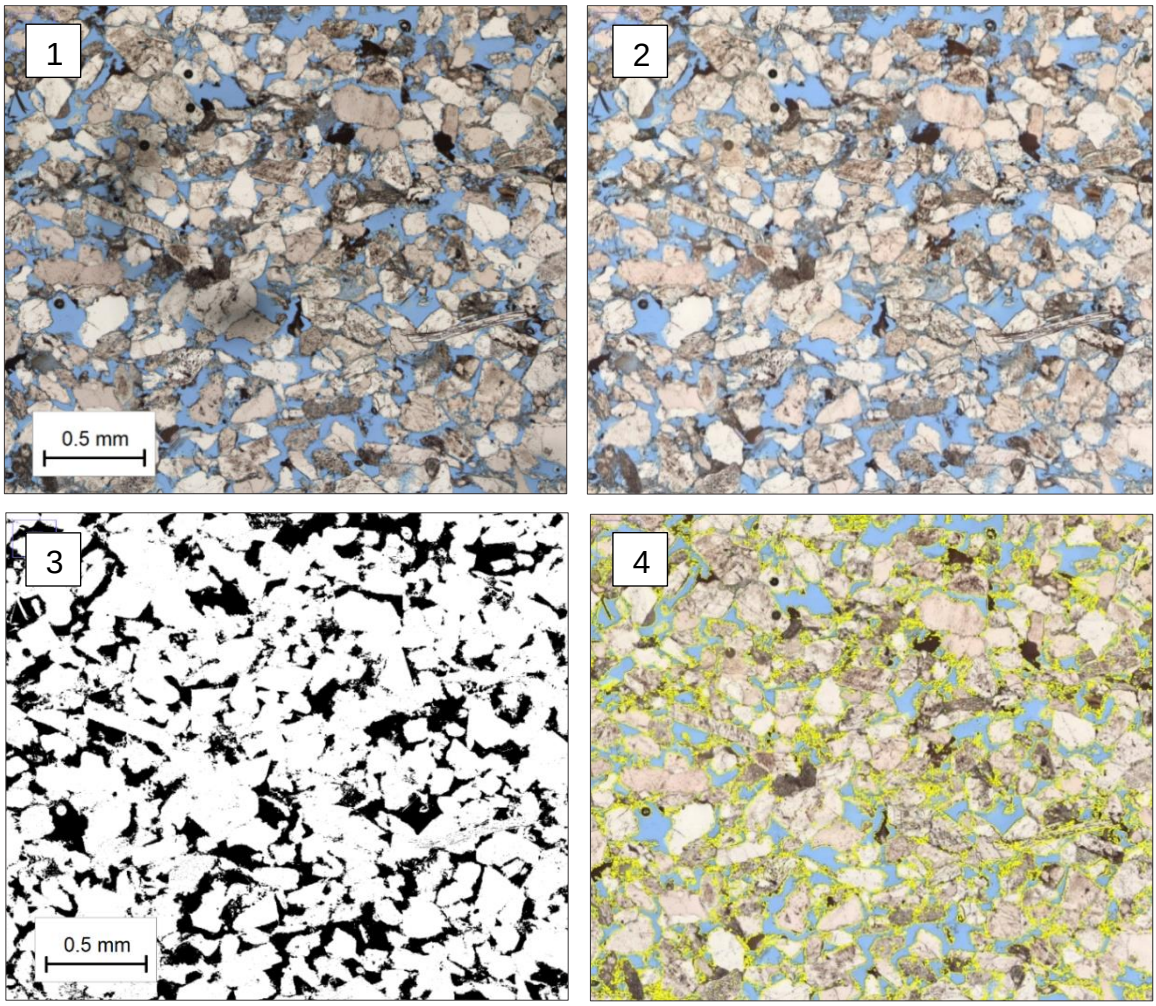

***Figure 10**. Pre-processing steps of undeformed sample BW-00 mosaic, with step 1) fraction of the original mosaic with unwanted shadows, 2) results using the 'subtract background', creating a smooth base for further image analysis 3) subsequent 'color threshold' function (Default thresholding method, B&W threshold colour and HSB colour) space isolating grains (white) from the background (black), and step 4) selecting the pore space for calculating the pore fraction.*

colour) and playing around to find appropriate threshold values (hue, saturation and brightness, values depending on the colouring of the mosaic), the blue background representing the pore space can be segmented from the grain network and subsequently selected. This way the pore fraction of a disclosed area can be estimated, which equals the selected area.

2.4.3 Microstructural analysis

Microstructural analysis has been performed on sections of undeformed- and all experimentally deformed (both conventional- and true triaxial) Bleurswiller samples. Pre-processed mosaics are used to obtain average porosities (using the previous described 'color threshold' function) and average grain sizes of the selected areas. To obtain the average grain size, the longest diameter of 200 arbitrary chosen grains is selected using the 'Line tracing' tool in ImageJ (*Schindelin et al. 2012*).

Quantitative intragranular crack mapping has been done on pre-processed optical microscopic mosaics of undeformed BW-00 and true triaxially deformed BW-02 thin sections (BW-02-1-a and BW-02-2-b). The 'Line tracing' tool is used to identify intragranular microcracks throughout the mosaic with a Wacon pen tablet. An intragranular crack is defined as a visual continuous dark line within a grain, and all uncertain indistinct features will be ignored (**Figure 11**). By identifying intragranular microcracks, the average crack length can be calculated (the sum of all crack lengths divided by the number of cracks). Furthermore, by quantifying intragranular cracks throughout a disclosed area of known size, the average crack density can be estimated. This average crack density is defined as the number of cracks per unit area and can be calculated by dividing the total amount of cracks by the total area of the analysed mosaic (in cm^2). Also, crack angles are measured to obtain an overview of possible preferred crack orientation throughout the sample. Microcrack orientations can be expressed as the *Feret's angle* in ImageJ, defined as the angle of the *Feret's diameter* (the longest distance between two points) denoted between 0 and 180°, with 0° being exactly horizontally and 90° exactly vertically oriented.

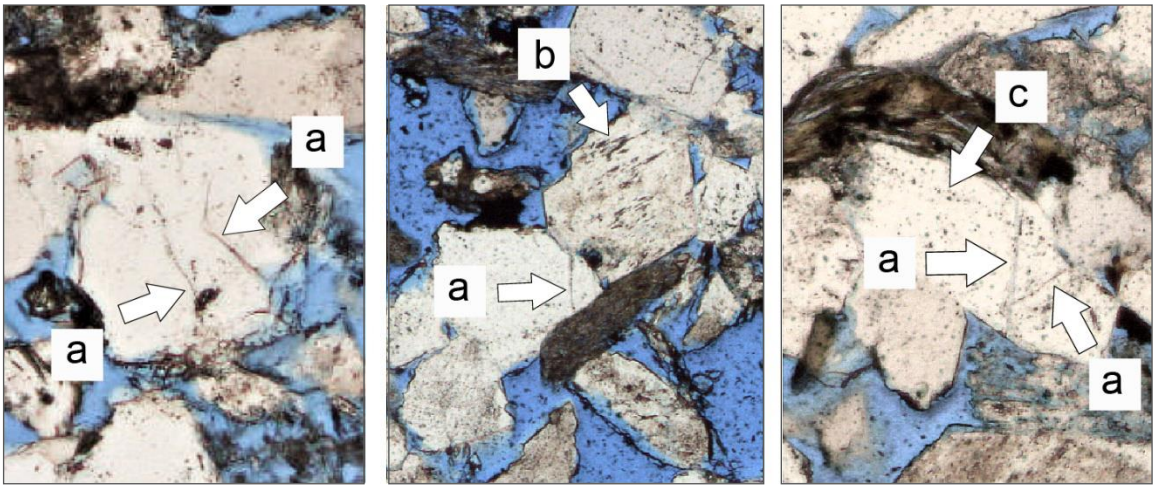

Figure 11. *Examples of grains containing visually similar features, with a) examples of continuous dark lines within grains, identified as intragranular microcracks during microstructural analysis, b) and c) discontinuous dark features within grains (patched or dotted), not identified as microcracks.*

3. Results

3.1 Conventional triaxial experiments: mechanical behaviour and microstructural observations

Two conventional triaxial experiments on Bleurswiller sandstone are conducted at effective pressures of 15 MPa and room temperature, one dry and one wet. The following mechanical data shows compressive stresses and compactive strains as positive.

3.1.1 Dry Bleurswiller behaviour

The mechanical data of the dry BW-06 sample during conventional triaxial loading is presented in grey in **Figure 12**. Two plots are presented, with differential stress plotted against volumetric strain and volumetric strain vs. axial strain. At lower differential stress, until ~70 MPa, a roughly linear axial strain trend indicates deformation of the sample in the elastic regime (**Figure 12a**). After reaching the yield point around 70 MPa, a significant deviation from linearity is observed. The differential stress attains its peak around ~86 MPa, followed by a rapid stress drop indicating failure. Prior to failure, the volumetric strain initially increases, indicating a porosity decrease and overall compaction of the sample. Around the peak stress, a volumetric strain decrease is observed and dilatancy takes place (**Figure 12b**).

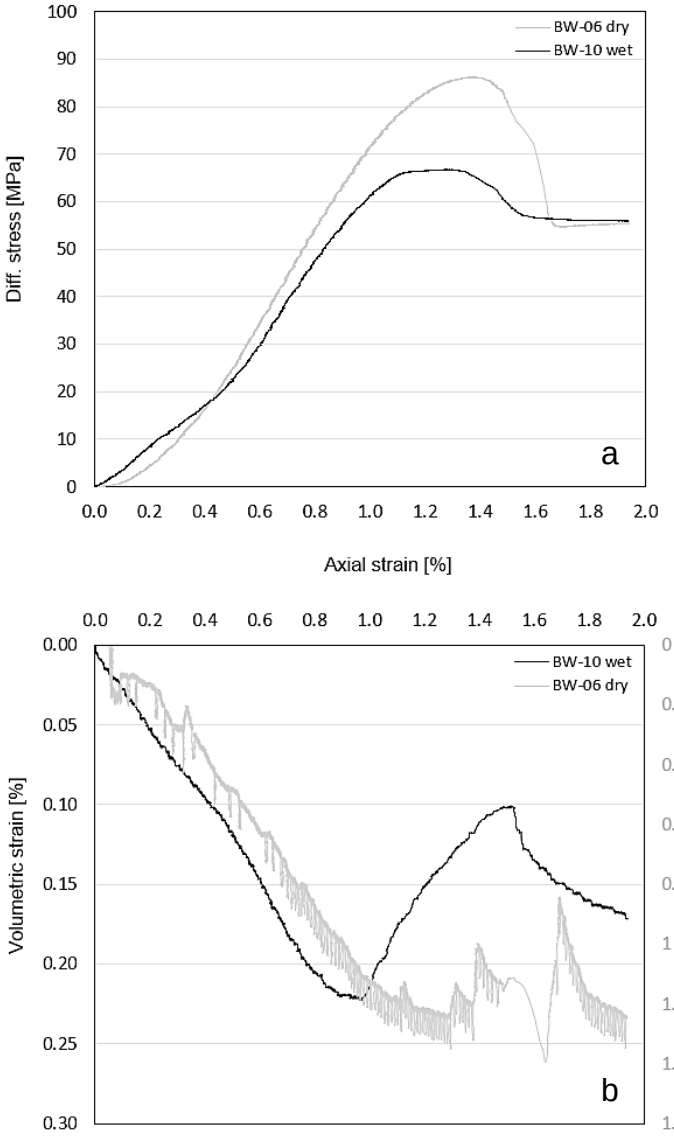

Figure 12. *Mechanical data for the dry BW-06 sample (grey), P_c = 15 MPa, and the wet BW-10 sample (black), Pc = 15 MPa and Pp = 10 MPa with a) differential stress plotted vs. axial strain and b) volumetric strain plotted vs. axial strain.*

3.1.2 Wet Bleurswiller behaviour

The wet BW-10 mechanical data during conventional triaxial loading is presented in black in **Figure 12**. Both graphs show similar shapes as the dry Bleurswiller sandstone graphs. Until a differential stress of ~55 MPa is reached, the nearly-linear trend indicates that elastic deformation is dominant (**Figure 12a**). The slope is roughly similar to the dry Bleurswiller experiment, suggesting comparable stiffness of the dry- and wet samples. After reaching the yield point around 55 MPa, an increasing amount of inelastic deformation takes place. The differential stress attains its peak around 68 MPa. The peak stress is

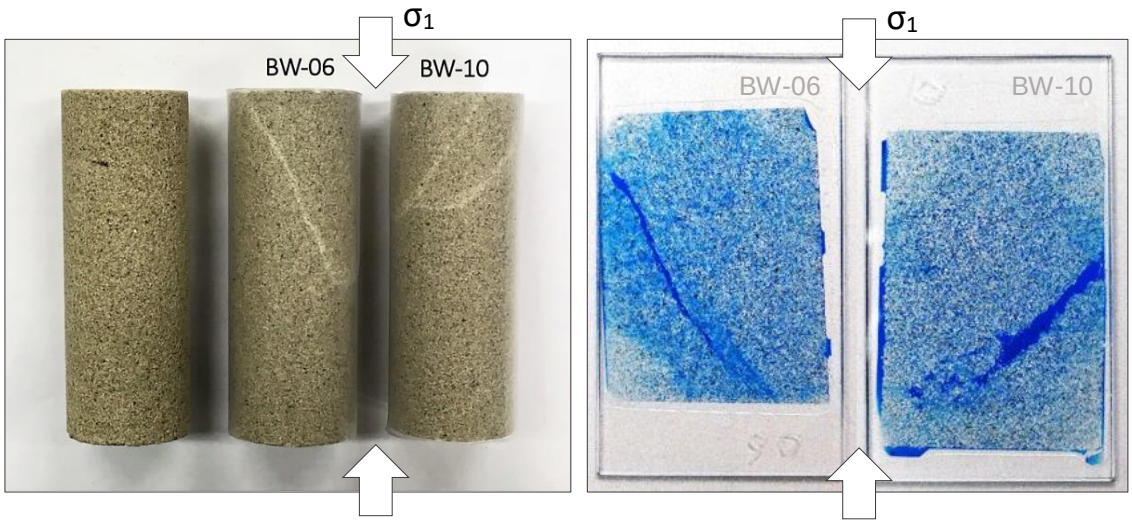

Figure 13. *Undeformed Bleurswiller, dry deformed Bleurswiller BW-06 and wet deformed Bleurswiller samples and their corresponding thin sections.*

accompanied by stable stress values and again succeeded by a slow stress drop, indicating failure. Similar to BW-06, the volumetric strain initially increases prior to failure, indicating porosity decrease and overall compaction of the sample (**Figure 12b**). Around the peak stress, volumetric strain decrease initiates and dilatancy takes place. When comparing results of the wet Bleurswiller sample to the dry sample, it is observed that the yield point and the differential stress peak are located at much lower stresses than observed for the dry BW-06 sample. Furthermore, whereas similar axial strain magnitudes are observed for both samples, the dry BW-06 sample shows volumetric strains of 5-6 times as high compared to BW-10.

3.1.3 Microstructural observations

Visual inspection of the dry deformed Bleurswiller sample (BW-06) shows that at low confining pressure (P_c) of 15 MPa, the failure mode of the Bleurswiller sandstone is typical for the brittle deformation regime.

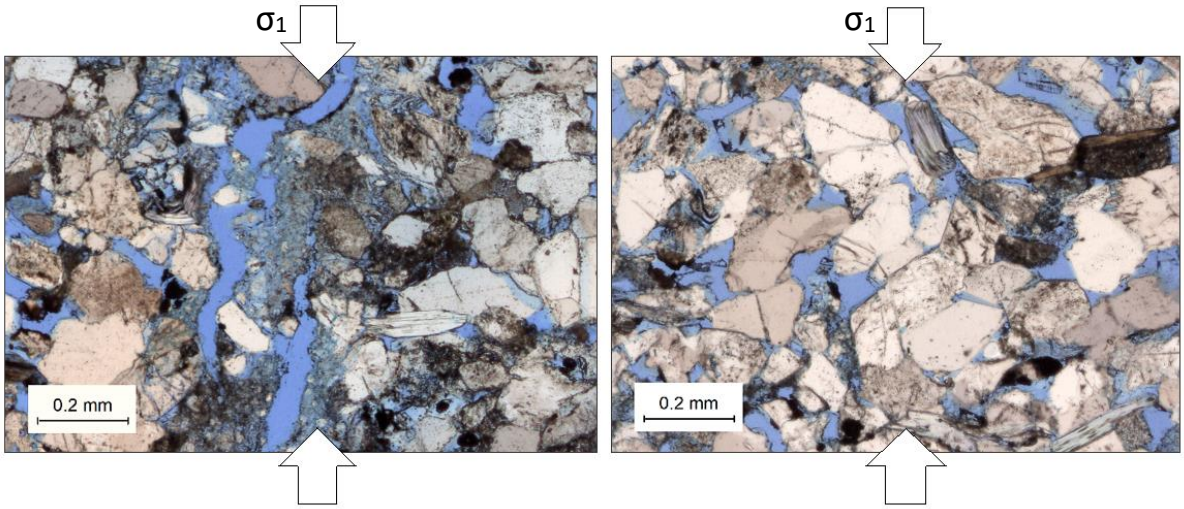

Figure 14. *Dry deformed BW-06 in thin section. Left: distinct fault plane with fine-grained crushed material which has been partly removed during thin section preparation. Right: fractured grains further away from the fault plane.*

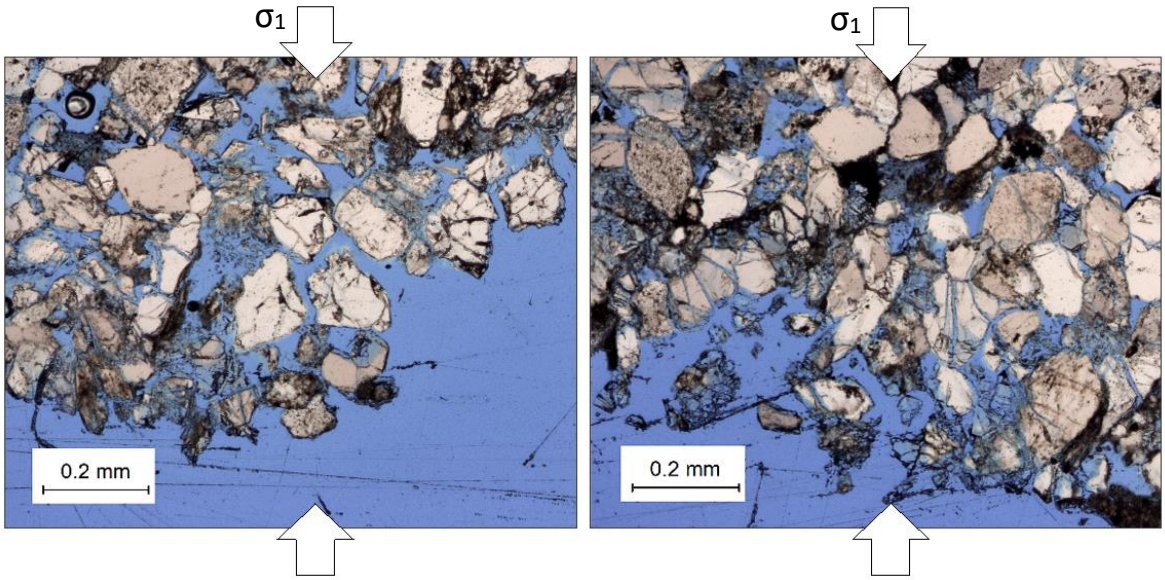

Figure 15. *Wet deformed BW-10 in thin section. Both pictures show extreme grain crushing along the fault plane, whereas fine-grained material has been lost during thin section preparation*

Failure occurred by shear localization along a distinct single macroscopic shear band cutting through a large area of the sample (**Figure 13Figure 13**). In thin section, a distinct fault plane of ~0.5 mm width is present. Grain crushing can be observed within the fault plane (**Figure 14**), but most fine-grained material is lost during thin section preparation due to locally poor impregnated zones. Grain crushing is also observed along the fault plane, within a small band of ~0.5 mm width. Further away from the fault plane, fractured grains are observed containing multiple intragranular cracks (**Figure 14**).

Macroscopic inspection of wet deformed Bleurswiller sample (BW-10) confirmed that, similar to the dry BW-06 sample, the failure mode is typical for the brittle deformation regime. Failure occurred by shear localization along two distinct macroscopic parallel shear bands, cutting through a smaller area of the sample (**Figure 13Figure 13**). Similar to BW-06, grain crushing is observed within- and along the fault plane (**Figure 15**). Nevertheless, compared to the dry BW-06, the fault plane observed in BW-10 thin section is wider (1.5-2.0 mm) and grain crushing is more abundant along the fault plane compared to the dry sample. At distance from the fault plane the sample looks again very similar to sample BW-06, with fractured grains containing multiple intragranular cracks.

3.2 True triaxial experiments: mechanical and acoustical data for dry Bleurswiller sandstone

Three experiments on cubic Bleurswiller samples were performed under true triaxial loading at the Christian-Albrechts University of Kiel. The data shows compressive stresses and compressive strains as positive, with maximum and minimum principal stresses denoted by σ_1 and σ_3, respectively.

3.2.1 Deviatoric stress stage: inducing damage

The first experimental step compromises deviatoric loading and unloading of the sample, to induce permanent sample damage. After all three principal stresses are simultaneously increased until ~15 MPa, σ_2 and σ_3 are kept at 15 MPa while stress in the σ_1 direction is increased stepwise. Loading is subsequently followed by stepwise lowering σ_1 until ~15 MPa, followed by complete unloading.

3.2.1a Mechanical data

Measured axial- and lateral strain changes of the sample in all principal directions and volumetric strain changes during deviatoric loading- and unloading are plotted in **Figure 16**. Observed are very similar results for samples BW-02 and BW-03 in all strain plots, whereas the BW-01 results significantly differ. In the axial compressional direction (Z-direction), strain almost linearly increases with increasing pressure, with compressive strains obtaining maximum values of ~0.85–1.0% for BW-02 and BW-03, and a value of 2.85% for BW-01 (**Figure 16a**). During unloading, a nearly linear decreasing tensile strain is observed for BW-02 and BW-03, whereas BW-01 shows an irregular trend (**Figure 16b**). In the X- and Y-direction, the samples show small compressive strains (~0.1%) until all principal stresses are increased to 15 MPa, followed by decreasing strains of ~0.20% for BW-02 and BW-03 after a maximum stress of 85 MPa was applied (**Figure 16c**). BW-01 follows the same trend, with tensile strains reaching relatively higher values of ~0.75% and ~0.55% in respectively the X- and Y-direction. Deviatoric unloading of samples BW-02 and BW-03 show strain recovery in the X- and Y-direction while stress in the Z-direction is decreased to 15 MPa, followed by small decreasing strains during the last 15 MPa (**Figure 16d**). BW-01 shows irregularly increasing strains during deviatoric unloading, indicating ongoing compression in the X- and Y-direction.

Increasing volumetric strain of all three samples indicates fast compaction the first 15 MPa of loading, followed by nearly linearly increasing compaction with increasing load (**Figure 16e**). At the end of the deviatoric loading stage, volumetric strains of BW-02 and BW-03 become constant around values of ~0.8%. BW-01 shows a larger increase in volumetric strain during loading (of ~1.7%, **Figure 16e**). Unloading shows a reversed trend, with linear decreasing strains for samples BW-02 and BW-03 and overall dilatation for all three samples (**Figure 16f**), with sample BW-01 showing lower strain values than observed during deviatoric loading. At the end of the unloading stage, lateral strain values in all principal directions and volumetric strains are not equal to their starting values (**Figure 16b, 16d** and **16f**). This difference indicates that full strain recovery did not take place and permanent deformation was induced during deviatoric loading.

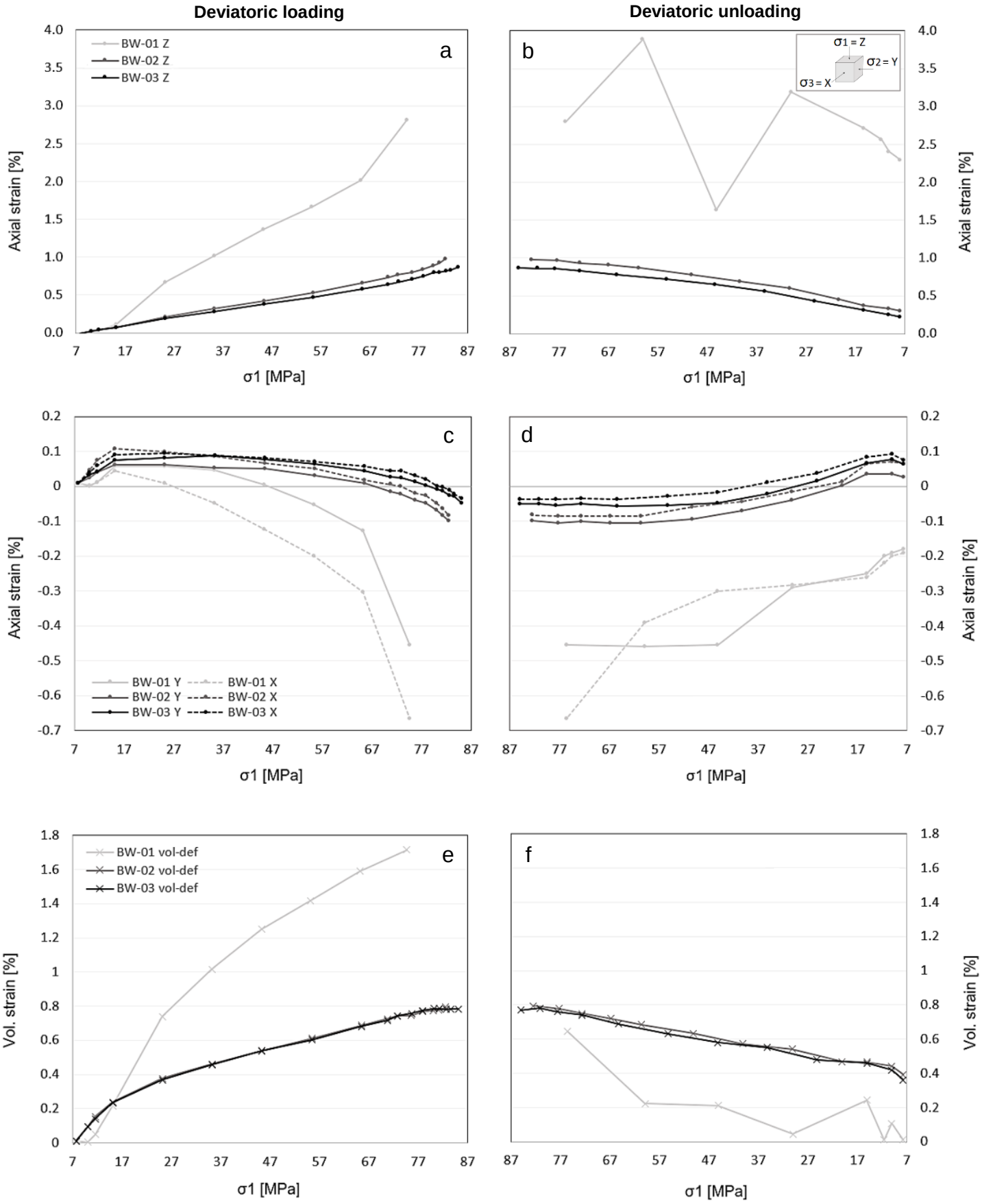

Figure 16. *Axial strain changes in all principal directions (X, Y and Z) and volumetric strain changes with changing stress during deviatoric loading (left diagrams) and unloading (right diagrams) for samples BW-01, BW-02 and BW-03.*

3.2.1b P-wave velocity measurements

P-wave travel times in all three principal directions are measured during deviatoric loading and unloading and are plotted against σ_1 in **Figure 17**. When looking at the Vp at the start of each experiment, observed are values around 3.2 km/s within differences of <3% for samples BW-02 and BW-03 in the X- and Y-direction, showing relatively good homogeneity. Sample BW-01 also shows homogeneous starting velocities, with slightly lower Vp (~2.7 km/s). In the Z-direction, all three samples show velocities of ~2.8 km/s. Again, similar velocity trends are observed for samples BW-02 and BW-03, whereas BW-01 shows different results.

Vp in the axial compressional (Z-)direction shows a rapid, non-linear increase with pressure until ~25 MPa (**Figure 17a**), indicating great sensitivity of acoustic waves at lower stress regime. Subsequent loading still initiates a velocity increase, less rapid than before, followed by a stable velocity trend around 70 MPa, with subsequent decreasing Vp after ~75 MPa for sample BW-02. During unloading, velocities in the Z-direction decrease, following roughly the same trend as during loading (**Figure 17b**). The Vp-Z of sample BW-01 shows lower values than the other two samples during both loading and unloading, but follows a similar trend. Velocities in the X- and Y-direction show different trends than in the Z-direction, with increasing Vp up to ~50 MPa, followed by a decreasing Vp trend (**Figure 17c**). A concave-shaped trend is observed for samples BW-02 and BW-03, whereas BW-01 shows a rapid Vp increase the first 15 MPa of loading, followed by a decrease in Vp during subsequent deviatoric loading. The first 70 MPa of deviatoric unloading, Vp slowly increases, followed by decreasing velocities the last 15 MPa of full unloading (**Figure 17d**). Again, BW-01 shows different results, with a rapid velocity drop during the first ~20 MPa of unloading, followed by nearly-constant velocity values in both the X- and Y-direction during further unloading.

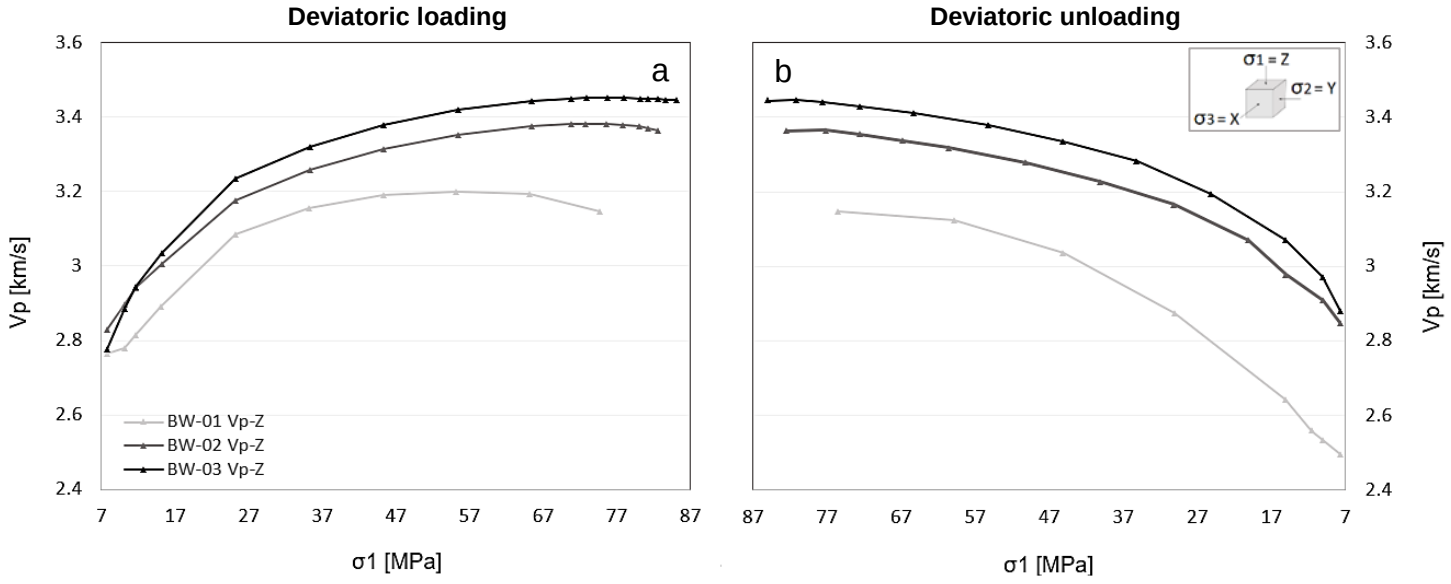

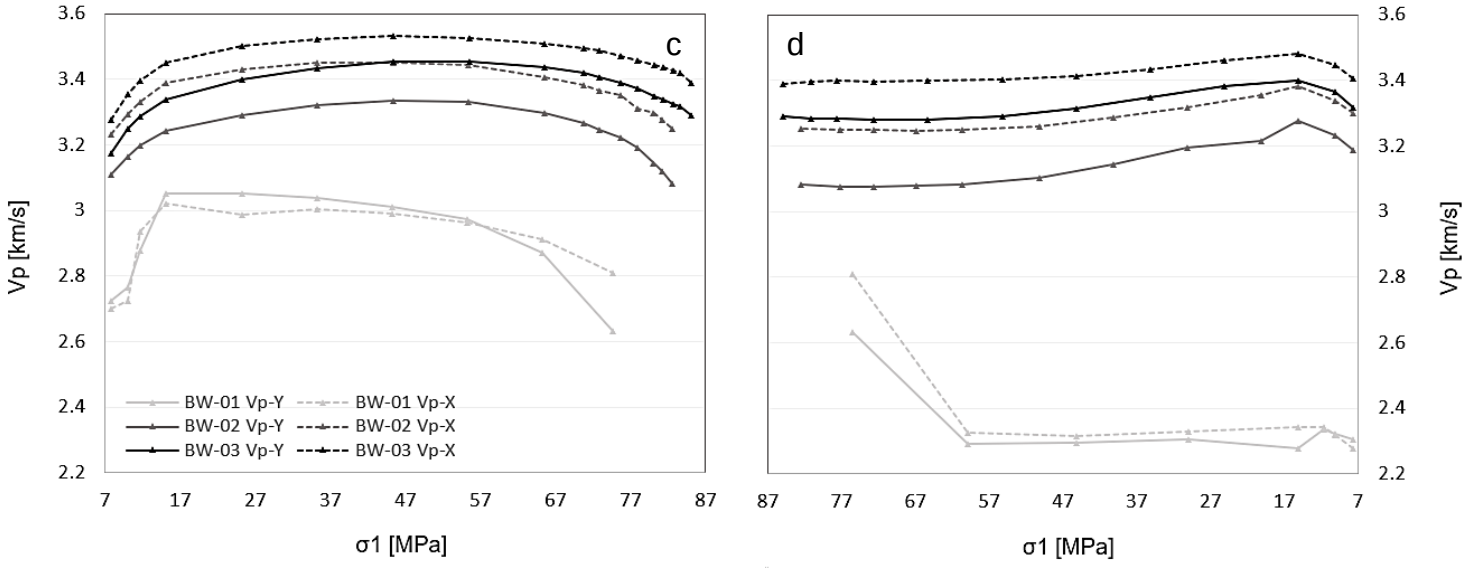

Figure 17. *P-wave velocity in all principal directions (X, Y and Z) with changing pressure during deviatoric loading (left diagrams) and unloading (right diagrams) for samples BW-01 (light grey), BW-02 (grey) and BW-03 (black).*

3.2.1c S-wave velocity measurements

S-wave travel times are measured in six different directions, with the three main propagation directions all including two polarization directions. S-wave velocities in these six different directions with increasing load can be found in **Figure 18**. Similar to the P-wave velocities, Vs shows nearly-identical starting values in the X- and Y-direction (<5% difference, **Figure 18b** and **18c**) suggesting a homogeneous starting material.

The Vs-XZ and Vs-YZ of samples BW-02 and BW-03 look very similar to the Vp data, with a rapid increase during initial loading (until ~15 MPa) followed by a more slow increase (**Figure 18a**). Vs-XZ becomes stable after ~45 MPa followed by a small velocity decrease starting around 65 MPa, whereas Vs-YZ continues to slowly increase and starts to decrease after ~70 MPa. During unloading, both Vs-XZ and Vs-YZ steadily decrease, followed by a rapid decrease the last 15 MPa (**Figure 18b**). In the X-direction, S-wave velocities (Vs-YX and Vs-ZX) show a rapid increase during the first ~15 MPa of loading, again indicating a great sensitivity of elastic waves at lower stress regime. The rapid increase is followed by a less rapid velocity increase, and ends with a Vs decrease (**Figure 18c**). A difference is observed between waves polarized in the Y- and Z-planes (Vs-YX, Vs-ZX). Whereas the Vs-ZX continues to increase until ~50 MPa and subsequently decreases after ~65 MPa, the Vs-YX decrease starts much earlier, ~40 MPa. Similar trends can be observed for Vs in the Y-direction, with increasing velocities during the beginning of loading followed by Vs-XY decrease around 40 MPa and Vs-ZY decrease starting around 65 MPa (**Figure 18e**). S-wave velocities during unloading look different than the loading trends (**Figure 18d** and **18e**). Whereas Vs-ZX and Vs-ZY stay relatively constant and only show a decrease the last ~15 MPa of unloading, the Vs-YX and Vs-XY show increasing values the first ~70 MPa of unloading. Sample BW-03 shows more varying values but with a similar overall trend as BW-02. BW-01 again shows very different results compared to the other samples, during both loading- and unloading in all principal directions.

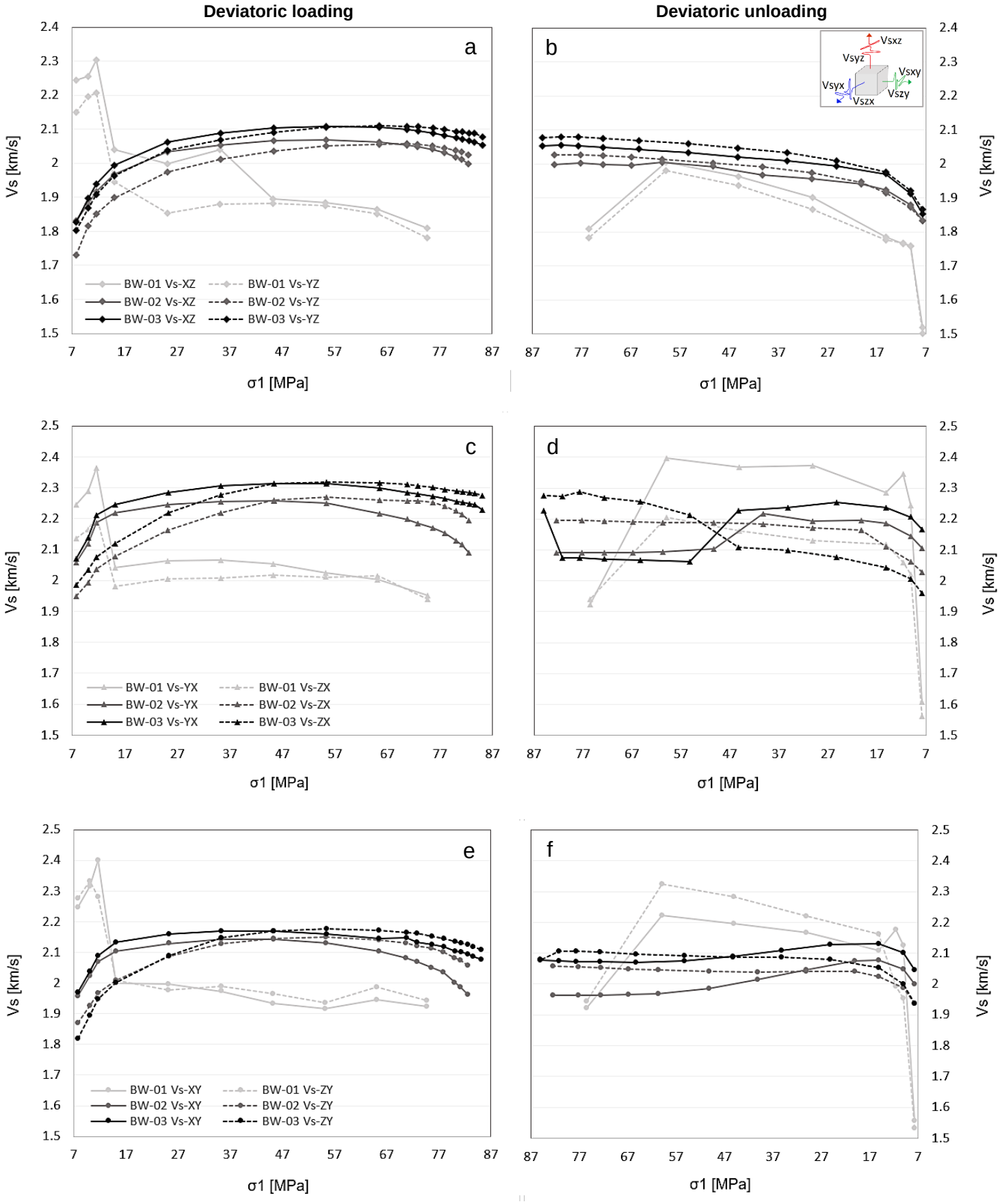

Figure 18. *S-wave velocities for both polarization directions in all principal directions (X, Y and Z) with changing pressure deviatoric loading (left diagrams) and unloading (right diagrams) for samples BW-01 (light grey), BW-02 (grey) and BW-03 (black).*

3.2.1d P-wave anisotropy and anisotropy rate of change measurements

New insights can be obtained by visualizing the Vp-anisotropy evolution throughout the experiments. Additionally, the Vp-anisotropy rate of change provides information about the speed at which the Vp-anisotropy in the sample increases or decreases. The Vp-anisotropy and Vp-anisotropy rate of change during deviatoric loading and unloading are plotted in **Figure 19**. Positive rate of change values reflect increasing anisotropy, negative values reflect decreasing anisotropy during both loading and unloading.

Observed are decreasing A-Vp values for samples BW-02 and BW-03 the first ~65 MPa of deviatoric loading, due to decreasing Vp differences between the three principal directions (**Figure 19c** and **19e**). From 20 to 65 MPa, the anisotropy of both samples is almost similar and steadily keeps on decreasing. When looking at the Vp-anisotropy rate of change, a decreasing rate of change is observed until ~60-65 MPa, indicating that anisotropy slowly approaches stable values. Around 65 MPa, BW-02 and BW-03 reach minimum A-Vp values of 2.5-4.0% with corresponding A-Vp rate of change values simultaneously becoming roughly zero. Subsequent loading causes anisotropy to rapidly increase again. Initial deviatoric unloading causes an anisotropy decrease, reflected by negative A-Vp rate of change values for samples BW-02 and BW-03 (**Figure 19d** and **19f**). Stable minimum anisotropy values of ~3.0-4.5% are reached around 45 MPa, corresponding to rate of change values of roughly zero. Further unloading initiates a large continuous anisotropy increase, with corresponding increasing positive rate of change values. Whereas sample BW-02 and BW-03 show similar results and trends, sample BW-01 shows deviating values, starting with low anisotropy values which rapidly increase during loading and decrease during unloading (**Figure 19a** and **19b**). All three samples show sudden rapid changes in the A-Vp rate of change the first 15 MPa of loading and the final 15 MPa of unloading.

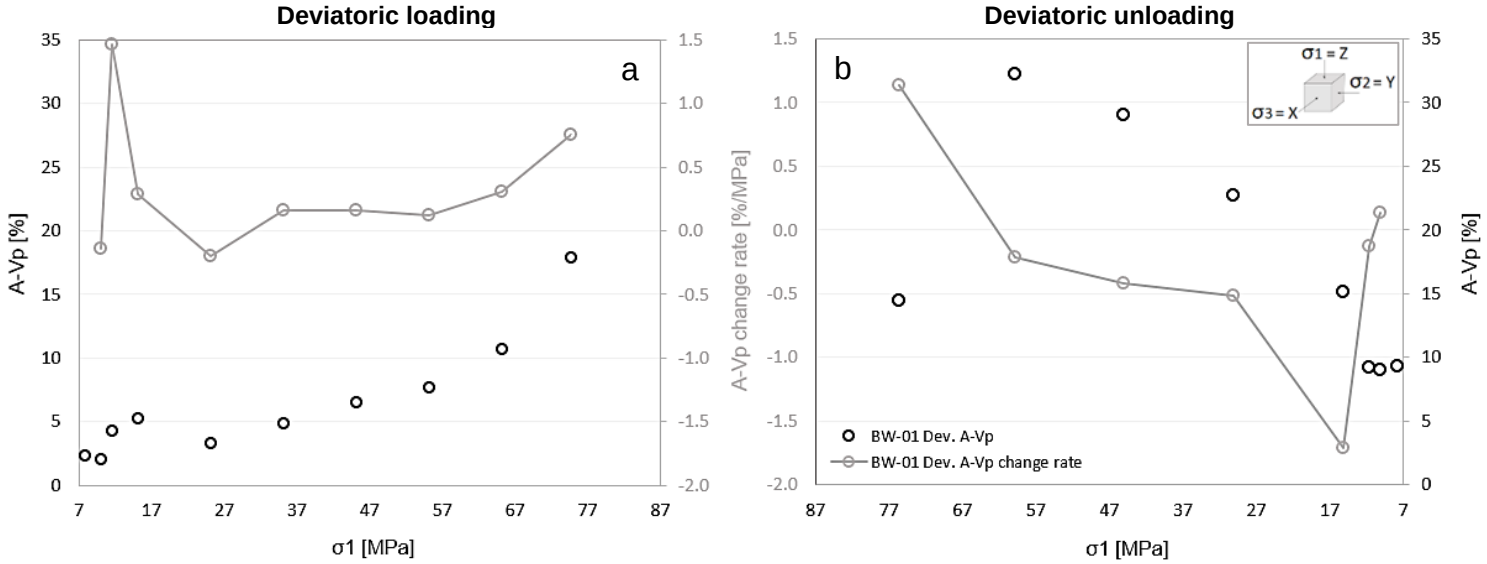

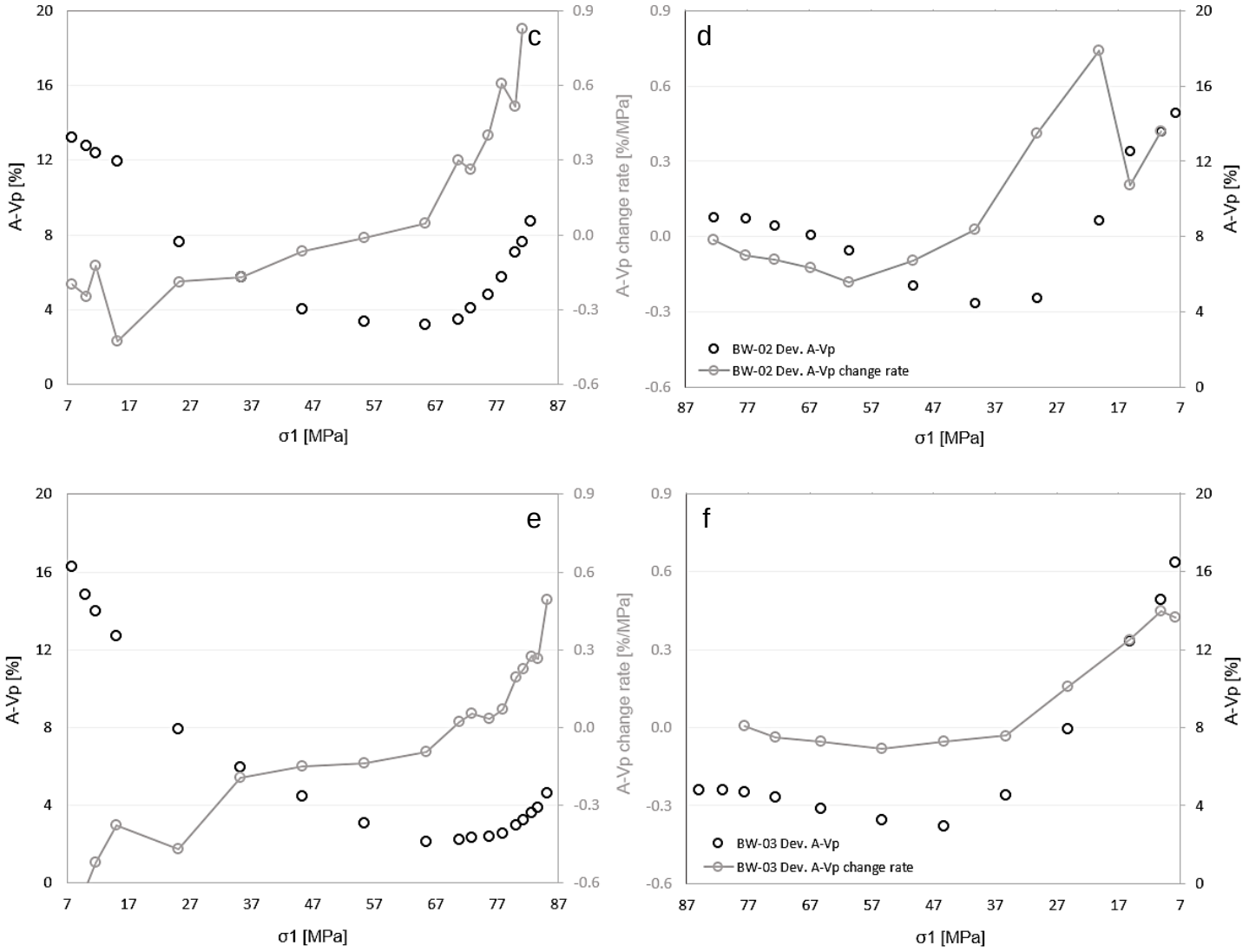

Figure 19. *Vp-anisotropy and Vp-anisotropy rate of change during deviatoric loading and unloading of samples BW-01 (top), BW-02 (middle) and BW-03 (below). Vp-anisotropy (A-Vp) is reflected by individual circles, A-Vp rate of change by connected circles. Positive Vp rate of change values reflect increasing anisotropy, negative values reflect decreasing anisotropy.*

3.2.2 Hydrostatic stress stage: retrieving damage

The deviatoric stress stage is followed by a second stage of hydrostatic loading and unloading. After all three principal stresses are simultaneously stepwise increased, unloading starts by stepwise lowering all principal stresses until the sample is fully unloaded.

3.2.2a Mechanical data

Figure 20 shows axial strain changes of the three samples in all principal directions and volumetric strain changes during hydrostatic loading and unloading. Since equal stress is applied in all three principal directions, axial strain evolution in all directions show the same trend. During loading, strain in the X-, Y- and Z-directions increases roughly linearly with increasing stress, up to values of ~0.5-0.8% for samples BW-02 and BW-03 (**Figure 20a** and **20c**). During unloading, axial strain steadily decreases (**Figure 20b**

and **20d**). After complete unloading, strain values of >0% indicate that full strain recovery did not take place. Similar to the results of the deviatoric loading stage, sample BW-01 shows different behaviour than the other two samples. In the X- and Y-direction the strain increases rapidly, reaching values more than twice as high as the other two samples (~2.0%, **Figure 20c**). In the Z-direction, an overall increasing axial strain is observed but values deviate greatly from a linear trend (**Figure 20a**). Unloading shows a more slowly decreasing strain, with much unrecoverable strain after full unloading in the X- and Y-directions (**Figure 20d**) and a small amount of unrecoverable strain in the Z-direction (**Figure 20b**).

The volumetric strain data of all samples look very similar, with nearly-linear increasing strain during loading (reaching values up to 2.3% for BW-02 and BW-03, and 4.5% for BW-01) indicating rapid sample compaction (**Figure 20e**). Subsequent hydrostatic unloading shows steadily decreasing strains (**Figure 20f**). Sample BW-01 shows a large amount of permanent volumetric deformation, with strain values of ~2.5%, whereas BW-02 and BW-03 show strain values of ~0.5% after full unloading.

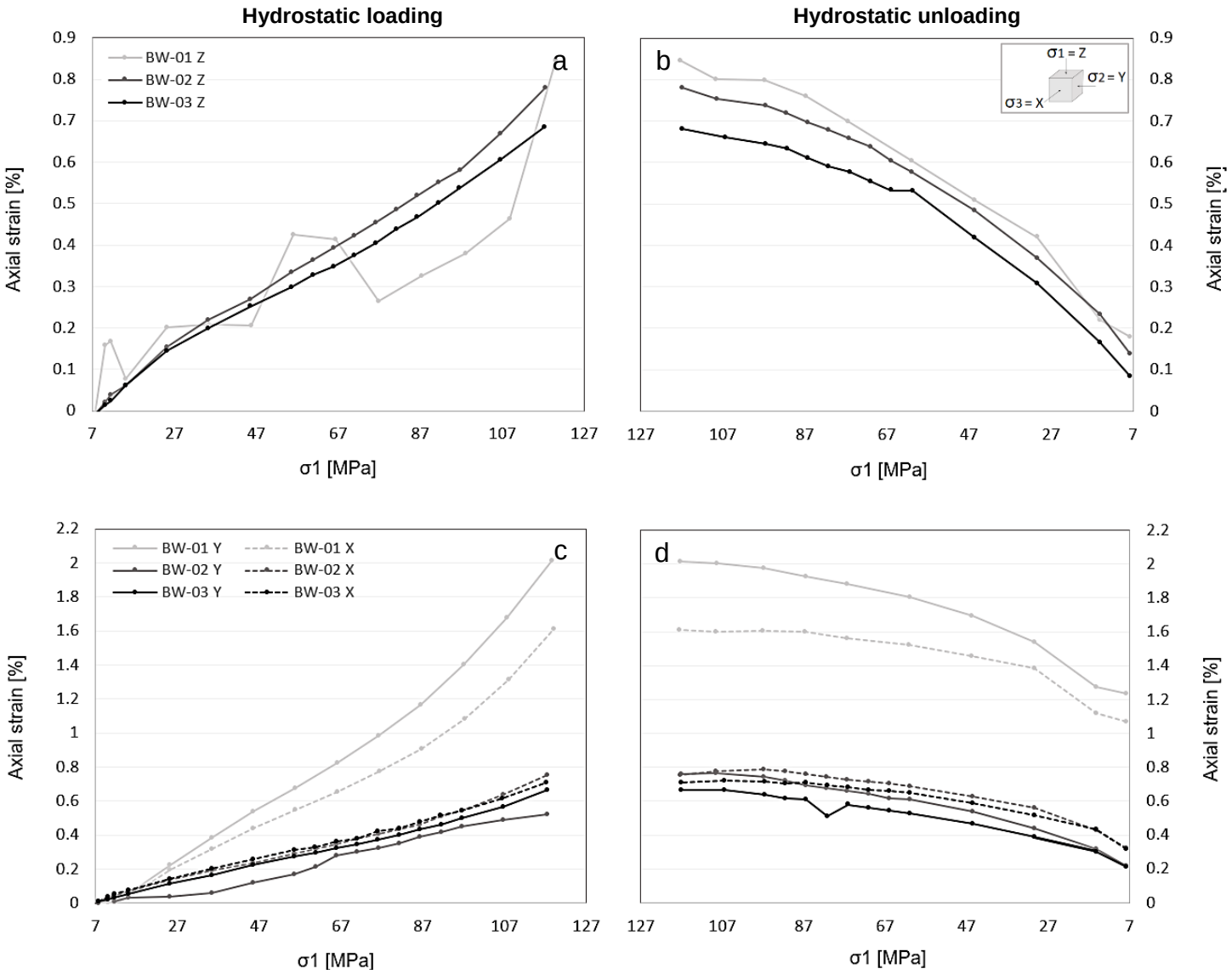

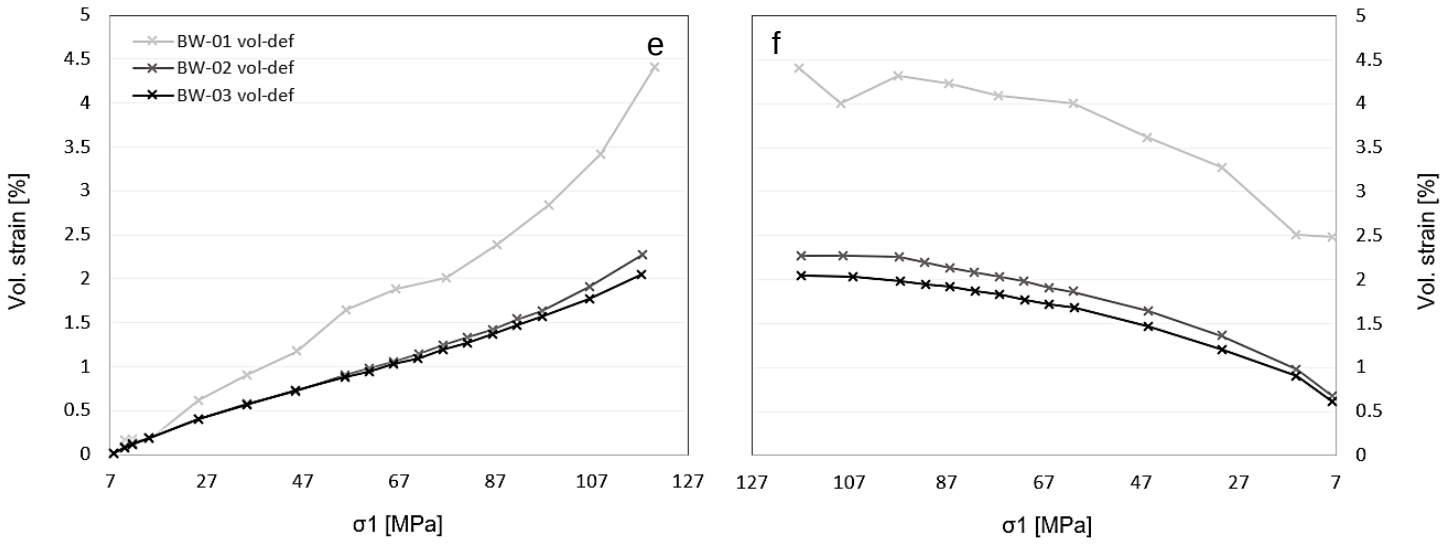

Figure 20. *Axial strain changes in all principal directions (X, Y and Z) and volumetric strain changes with changing stress during hydrostatic loading (left diagrams) and unloading (right diagrams) for samples BW-01 (light grey), BW-02 (grey) and BW-03 (black).*

3.2.2b P-wave velocities

P-wave velocity data during hydrostatic loading and unloading are plotted in **Figure 21**. With increasing stress, the Vp in all principal directions increase (**Figure 21a** and **21c**). A rapid P-wave velocity increase is observed for the first ~20 MPa, followed by slowly increasing velocities. The velocity increase continues with increasing stress, but becomes less when stresses reach higher values. In the X- and Y-direction, the velocity increase approximately becomes zero at the end of the hydrostatic loading stage and nearly stable Vp values are observed (**Figure 21c**). The P-wave velocity increase is largest in the Z-direction with a maximum increase of ~0.8 km/s (**Figure 21a**), compared to a maximum increase of ~0.4 km/s in the X- and Y-direction (**Figure 21c**). Looking at the P-wave velocity data during unloading, a reversed trend is

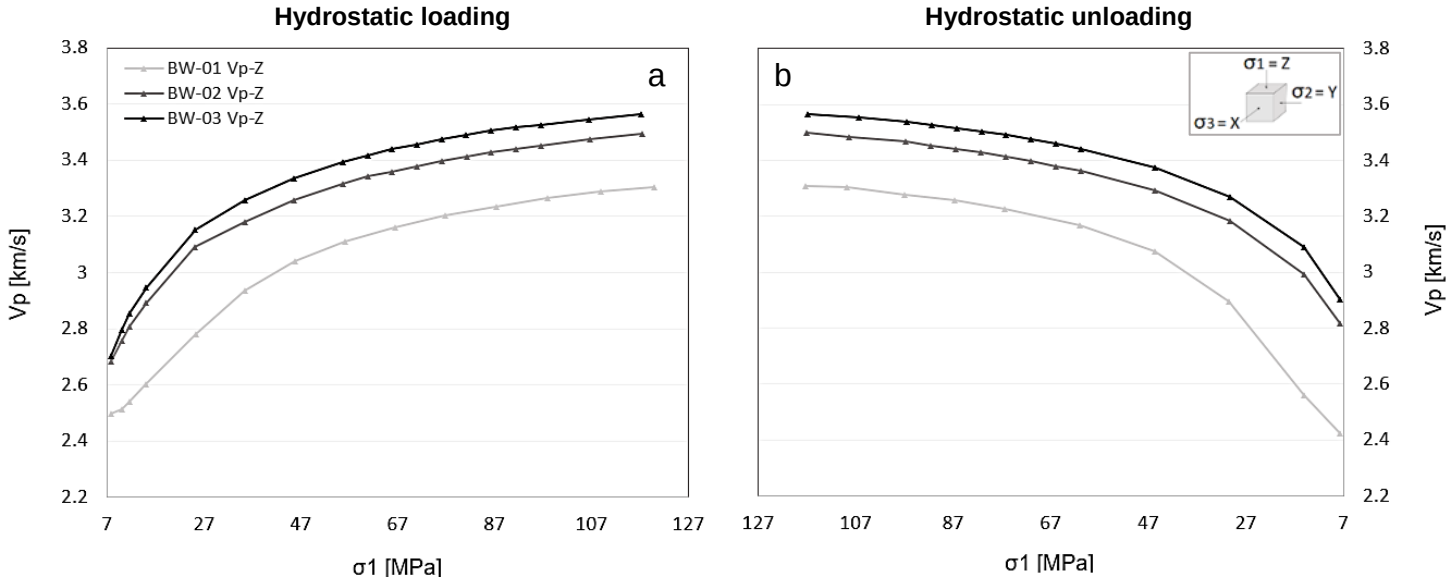

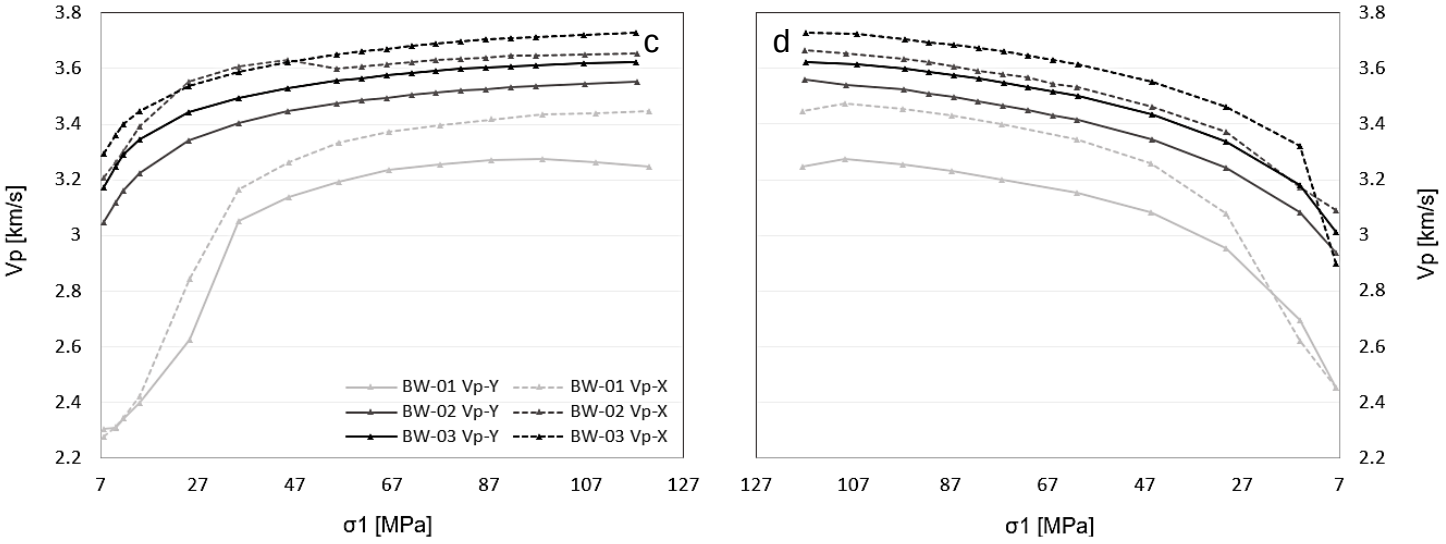

Figure 21. *P-wave velocity in all principal directions (X, Y and Z) with changing pressure during hydrostatic loading (left diagrams) and unloading (right diagrams) for samples BW-01 (light grey), BW-02 (grey) and BW-03 (black).*

observed (**Figure 21b** and **21d**). The unloading data follows the loading trend very accurately, with an accelerating rate of decreasing velocities. Velocity data of BW-01 shows similar trends as the other two samples, but initial velocities before the start of hydrostatic loading are lower compared to velocities measured for BW-02 and BW-03, especially in the X- and Y-direction (**Figure 21c**).

3.2.2c S-wave velocities

Monitored S-wave velocities in six different directions can be found in **Figure 22.** Similar to the P-wave velocities, Vs trends show a rapid increase during the first ~20 MPa of hydrostatic loading due to great sensitivity at the lower stress regime (**Figure 22a, 22c** and **22e**). The initial rapid Vs increase is followed by a more slow increase during subsequent hydrostatic loading. During continuous stress increase, the velocity increase becomes less when stresses reach higher values. Again, as observed for the P-wave velocity, nearly constant Vs values are observed at the end of the hydrostatic loading stage in the X- and Y-direction (**Figure 22c** and **22e**), and the P-wave velocity increase is highest in the Z-direction (**Figure 22a**). The velocity trends are again roughly similar for BW-02 and BW-03, with minor differences in values between wave directions and the different samples. Unloading data shows a reversed trend, with an accelerating rate of decreasing velocities (**Figure 22b, 22d** and **22e**). BW-01 Vs data shows overall similar trends as the other two samples, but velocity values are much lower and sudden changes in velocity in between the loading steps are observed.

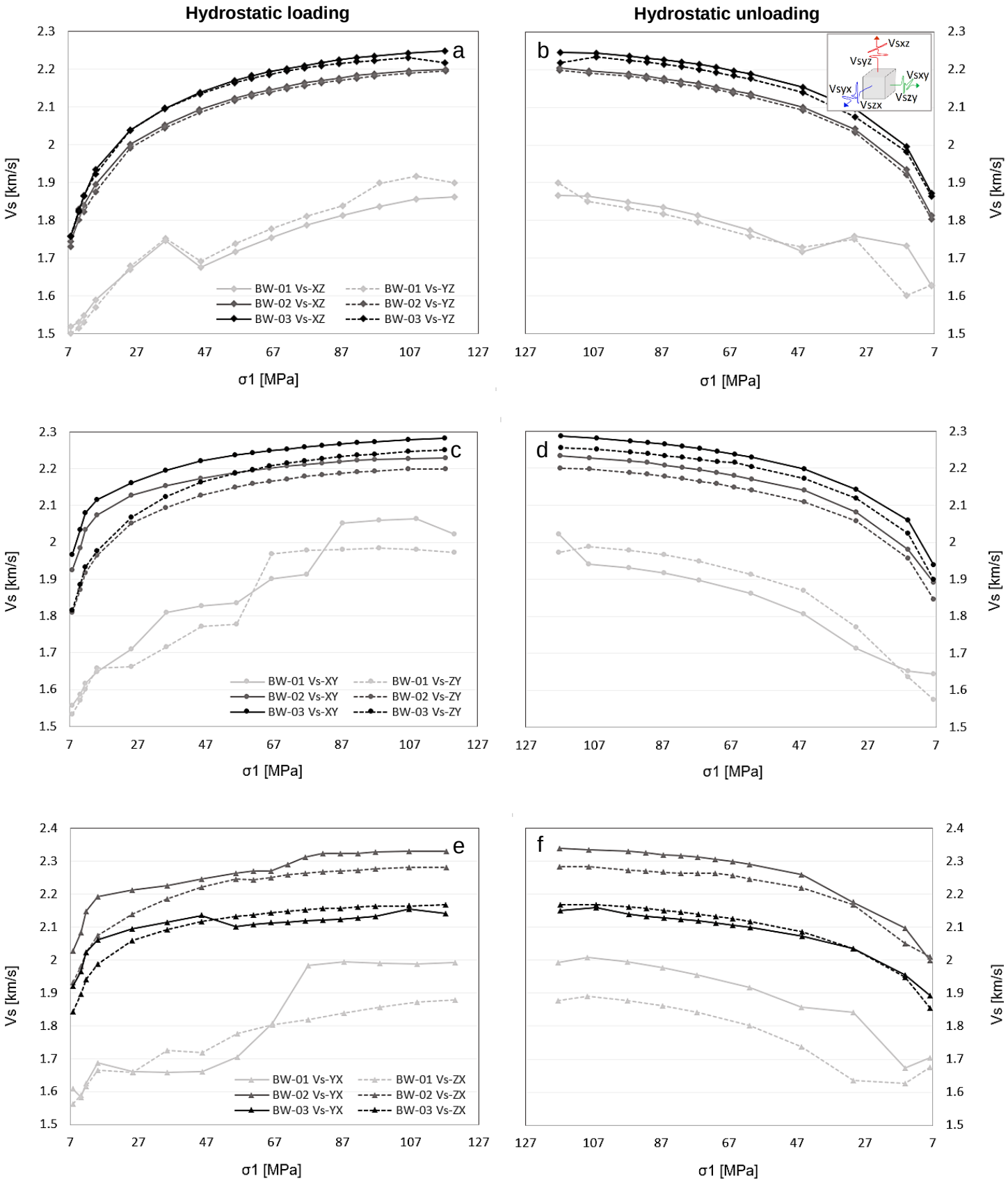

Figure 22. *S-wave velocities for both polarization directions in all principal directions (X, Y and Z) with changing pressure hydrostatic loading (left diagrams) and unloading (right diagrams) for samples BW-01 (light grey), BW-02 (grey) and BW-03 (black).*

3.2.2d P-wave anisotropy and anisotropy rate of change measurements

The Vp-anisotropy and Vp-anisotropy rate of change during hydrostatic loading and unloading are plotted in **Figure 23**. Positive Vp rate of change values reflect increasing anisotropy and negative values reflect decreasing anisotropy during both loading and unloading. When looking at the evolution of P-wave anisotropy, observed is a decrease of the P-wave anisotropy with increasing hydrostatic load for all three samples (**Figure 23a**, **23c** and **23e**). The A-Vp decrease first shows a rapid trend, followed by a more slow decrease from ~65 MPa, with values decreasing from ~8% to minimum values of ~5% in between 65 and 120 MPa of loading (**Figure 23a, 23c** and **23e**). From ~65-85 MPa, the rate of change decrease is small, becoming roughly constant around 85 MPa around values of -0.04 %/MPa. At the end of the loading cycle, BW-01 starts to deviate from this path whereas BW-02 and BW-03 are still in close agreement. During initial hydrostatic unloading, A-Vp stays constant (~5%), corresponding with A-Vp rate of change values of zero (**Figure 23b, 23d** and **23f**). When the stress reaches values of ~65 MPa, the Vp anisotropy of samples BW-02 and BW-03 slowly start to increase again, reflected in increasing positive A-Vp rate of change. Contrary, the P-wave anisotropy of sample BW-01 starts to slowly decrease (**Figure 23b**). Additionally, the

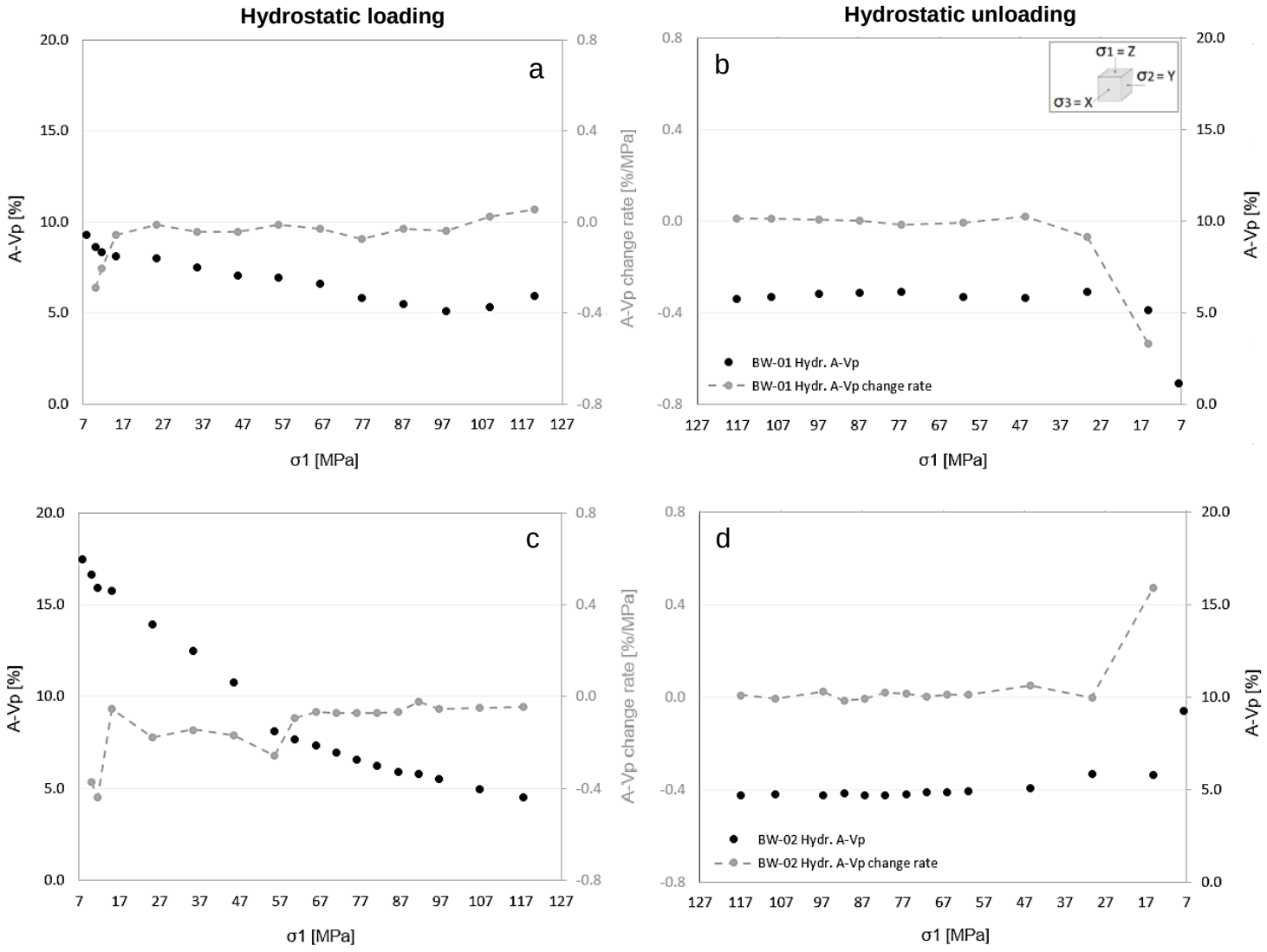

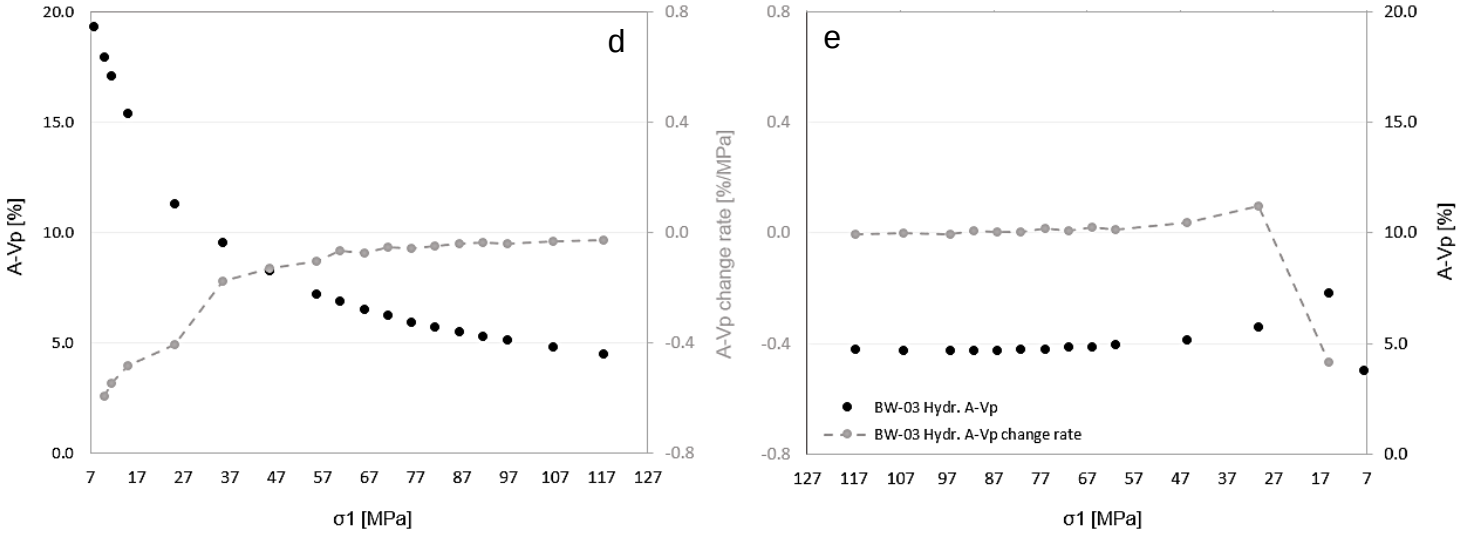

Figure 23. *Vp-anisotropy and Vp-anisotropy rate of change during hydrostatic loading and unloading of samples BW-01 (top), BW-02 (middle) and BW-03 (right). Vp-anisotropy (A-Vp) is reflected by individual circles, A-Vp rate of change by connected circles. Positive Vp rate of change values reflect increasing anisotropy, negative values reflect decreasing anisotropy.*

A-Vp rate of change values of BW-02 and BW-03 show sudden rapid changes during the last 15 MPa of unloading (**Figure 23d** and **23f**).

3.2.2e S-wave anisotropy and anisotropy rate of change measurements

Similar to the P-wave measurements, the S-wave anisotropy (A-Vs) and anisotropy rate of change during hydrostatic loading and unloading can be visualized, with positive Vs rate of change values reflecting increasing anisotropy and negative values reflect decreasing anisotropy. A-Vs results for all principal directions are plotted in **Figure 24**, with corresponding rate of change plotted in **Figure 25**.

During the first part of hydrostatic loading, samples BW-02 and BW-03 show rapidly decreasing A-Vs values in the X- and Y-direction, followed by a more slow decrease during subsequent loading (**Figure 24c** and **24e**). Whereas the A-Vs Y decrease continues slowly, the A-Vs X shows a sudden small increase in values (~70 MPa for BW-02 and ~50 MPa for BW-03), followed by roughly constant values. Around 85 MPa, both the A-Vs X and A-Vs Y show constant values of respectively ~2.2% and ~1.5% for BW-02 and ~1.5 for BW-03. Measurements of the A-Vs in the Z-direction show different results during hydrostatic loading, with small anisotropy values (mostly <1.0%) staying roughly constant. Unloading shows very constant minimum A-Vs Y and A-Vs Z values until the last ~50 MPa of unloading (**Figure 24d** and **24f**). BW-01 again shows different results compared to the other two samples, with sudden changes in the anisotropy (**Figure 24a** and **24b**).

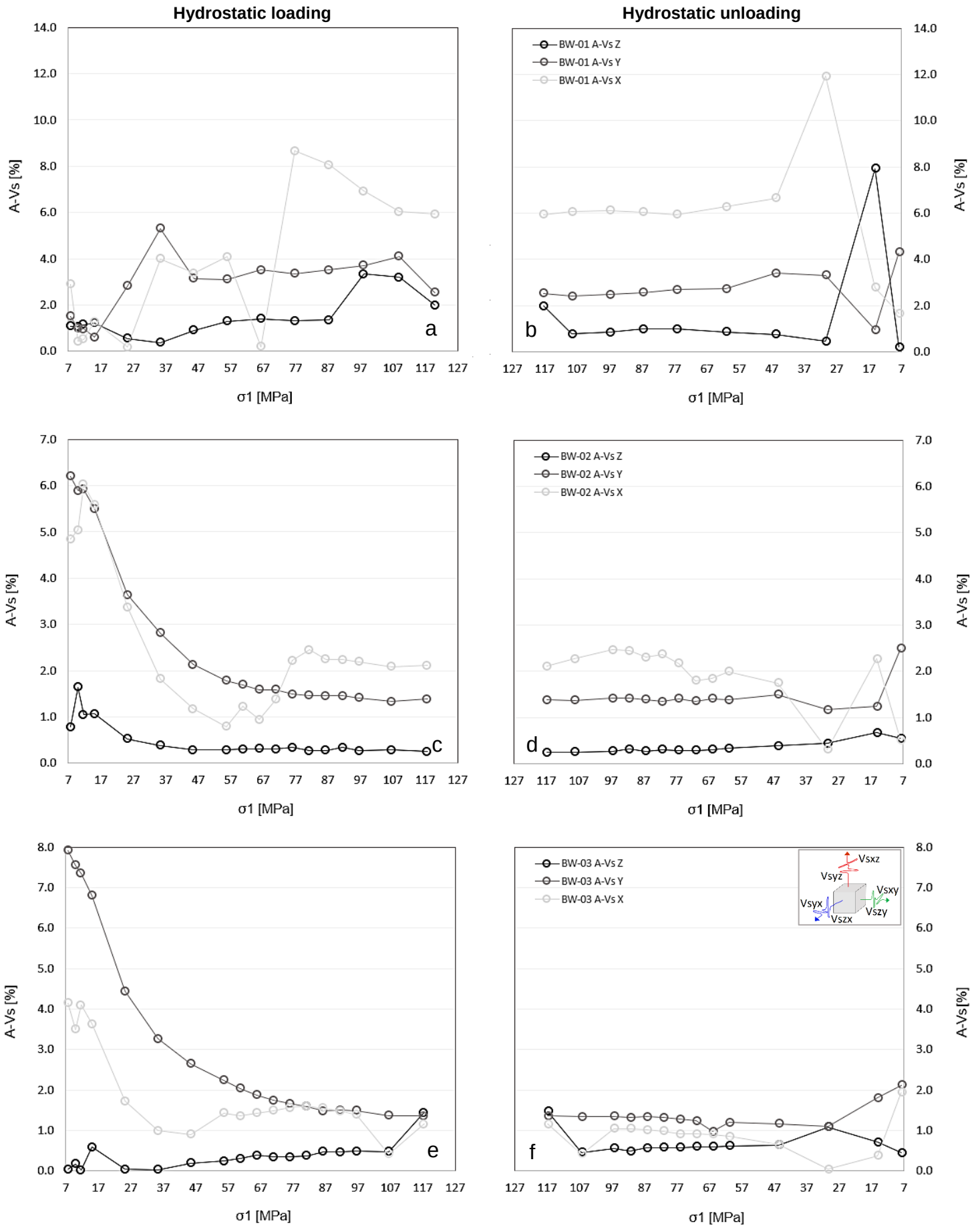

Figure 24. *Vs-anisotropy during hydrostatic loading and unloading of samples BW-01 (top), BW-02 (middle) and BW-03 (bottom). A-Vs has been calculated for all principal directions (X in light grey, Y in grey and Z in black).*

The A-Vs rate of change reflects the speed at which the anisotropy changes with increasing- and decreasing stress (in %/MPa). Rapidly changing A-Vs values during initial hydrostatic loading are reflected in large rate of change values, which show a continuous decrease during subsequent loading for samples BW-02 and BW-03 (**Figure 25c** and **25e**). Whereas the A-Vs Z rate of change becomes zero early during loading (~50 MPa), the A-Vs rate of change in all three principal directions seem to converge and cross around 85 MPa. This can mostly be observed when looking at the data of sample BW-02, with all rates becoming almost zero and following the same trend (**Figure 25c**). Subsequent unloading shows A-Vs values rate of change which keep roughly constant during the first ~50 MPa (**Figure 25b** and **25d**). Again, BW-01 rate of change results during loading shows sudden changes due to varying anisotropy values, whereas unloading shows similar trends as samples BW-02 and BW-03.

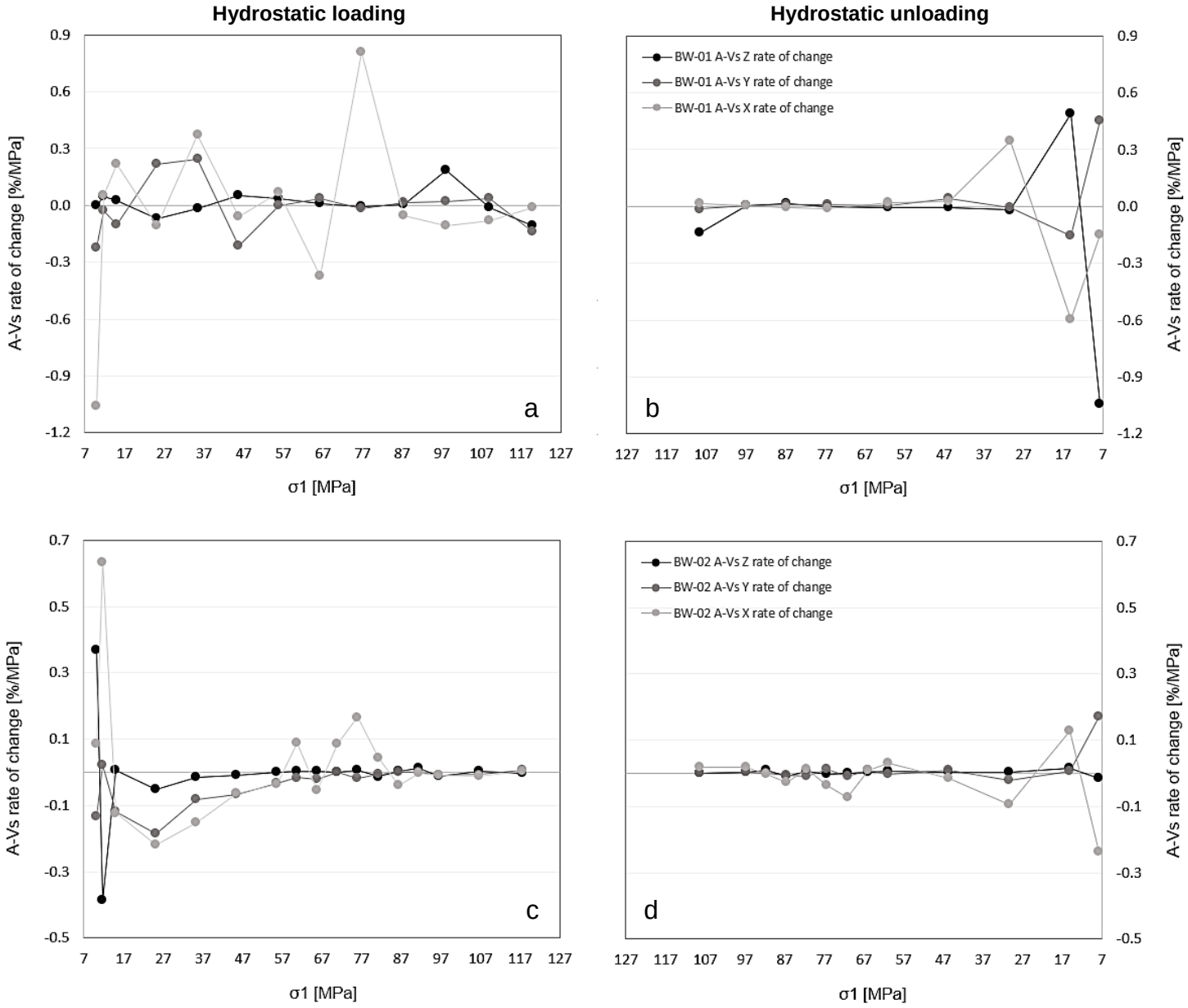

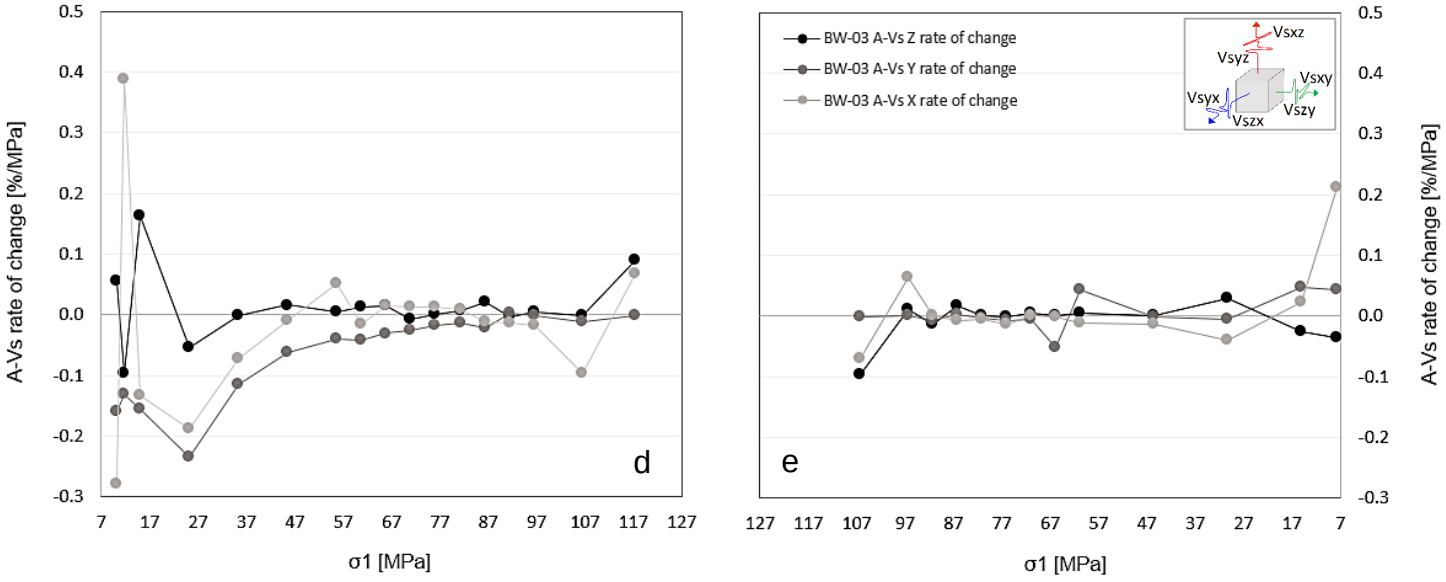

Figure 25. *Vs-anisotropy rate of change during hydrostatic loading and unloading of samples BW-01 (top), BW-02 (middle) and BW-03 (bottom), calculated for all principal directions (X in light grey, Y in grey and Z in black). Positive A-Vs rate of change values reflect increasing anisotropy, negative values reflect decreasing anisotropy.*

3.3 Microstructural analysis: crack density- and crack orientation of true triaxially deformed samples

Thin sections for microstructural analysis were made of one undeformed (BW-00) and two true triaxially deformed Bleurswiller samples (BW-01 and BW-02, **Figure 26**). All prepared sections are oriented in the same way, perpendicular to the experimental Z-direction and parallel to the X- and Y-directions.. Within a disclosed area of known size and orientation, the porosity, grain size and crack density are estimated. Also, crack angles are measured to observe possible preferred crack orientations throughout the sample.

3.3.1 Undeformed Bleurswiller sandstone BW-00

The undeformed Bleurswiller sample (BW-00) functions as framework for comparison between the original Bleurswiller material and the true triaxially deformed samples. Microstructural analysis has been performed on a disclosed area of 9.8 x 8.5 mm. The results of sample BW-00 are summarized in **Table 3**. A heterogeneous pore space distribution is observed with porosity clusters present within the sample (**Figure 27**). The average porosity of the disclosed area is estimated using the *'color threshold'* function in ImageJ, resulting in a value of 23.2%. This value is somewhat lower but still similar to the average porosity of 24.4% calculated for 10 Bleurswiller samples using the Saturation method *(ISRM 1979)* reported earlier. The average grain size over a total number of 200 grains is 193 micron and the total number of counted intragranular microcracks is 816, with an average crack length of 86 micron. This results in an average crack density of 1301 cracks/cm^2. Microcracks are well distributed throughout the sample, mostly present within larger feldspar clasts (**Figure 27**) and do not show a clear preferred orientation (**Table 3**).

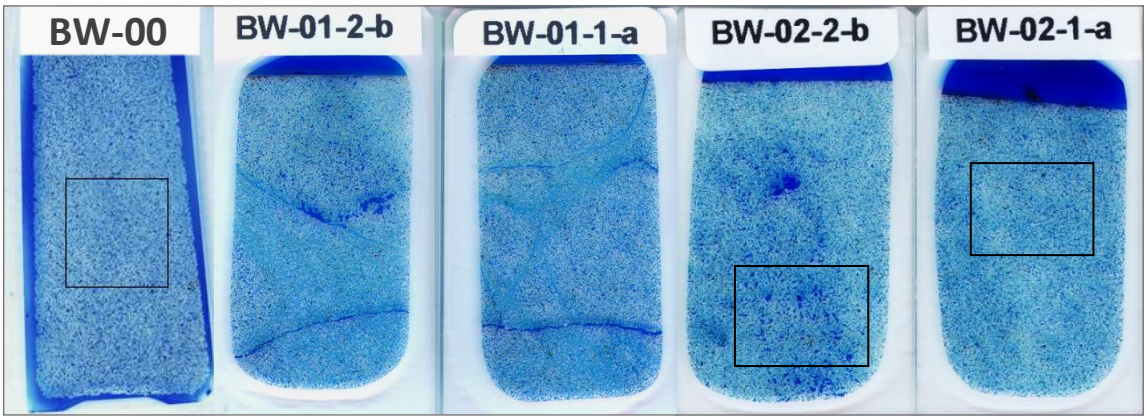

Figure 26. *Thin sections used for microstructural analysis: section of undeformed sample BW-00, two sections deformed and failed BW-01 sample (BW-01-1-a and BW-01-2-b) and two sections of deformed BW-02 (BW-02-1-a and BW-02-2-b). Microcrack analysis has been performed within the indicated disclosed areas of BW-00, BW-02-2-b and BW-02-1-a.*

3.3.2 True triaxially deformed Bleurswiller sandstone BW-02

After sample BW-02 was taken out of the true triaxial multi-anvil apparatus, the sample appears macroscopically intact. Microstructural analysis of true triaxially deformed sample BW-02 has been performed on two prepared thin sections (BW-02-1-a and BW-02-2-b). When looking at the constructed thin sections, a large fraction of blue coloured pores is again recognized (**Figure 26**). Section BW-02-2-b shows large patches of blue filling up areas where no grains are present, which probably originated during cutting of the sample. Microstructural analysis has been performed over disclosed areas of respectively 9.3 x 7.5 mm and 9.6 x 7.3 mm of samples BW-02-1-a and BW-02-2-b (**Figure 26**). All results of sample BW-02 are summarized in **Table 2**. The average porosity of the area is estimated in ImageJ, resulting in a value of 14.5-15.1%, much lower than the average porosity of the undeformed Bleurswiller BW-00 sample. BW-02-2-b shows a slightly higher porosity due to the removal of grains during thin section preparation. The averaged grain size over a total number of ~200 grains is 205-221 micron and the total number of counted cracks for sections BW-02-1-a and BW-02-2-b are respectively 507 and 463. This results in average crack densities of respectively 835 and 741 cracks/cm^2, lower than the crack density of the undeformed

	Undeformed	**Deformed**	
Sample name	*BW-00*	*BW-02-1-a*	*BW-02-2-b*
Analysed area (mm x mm)	9.8 x 8.5	9.3 x 7.5	9.6 x 7.6
Av. porosity (%)	23.2	14.5	15.1
Av. grain size (micron)	193	221	205
Cracks (no.)	816	507	463
Crack density (no./cm^2)	1301	835	741
Av. crack length (micron)	86	85	115
Av. crack orientation (°)	89	85	91

Table 2. *Overview of the microstructural results of the analysed deformed- and undeformed thin sections.*

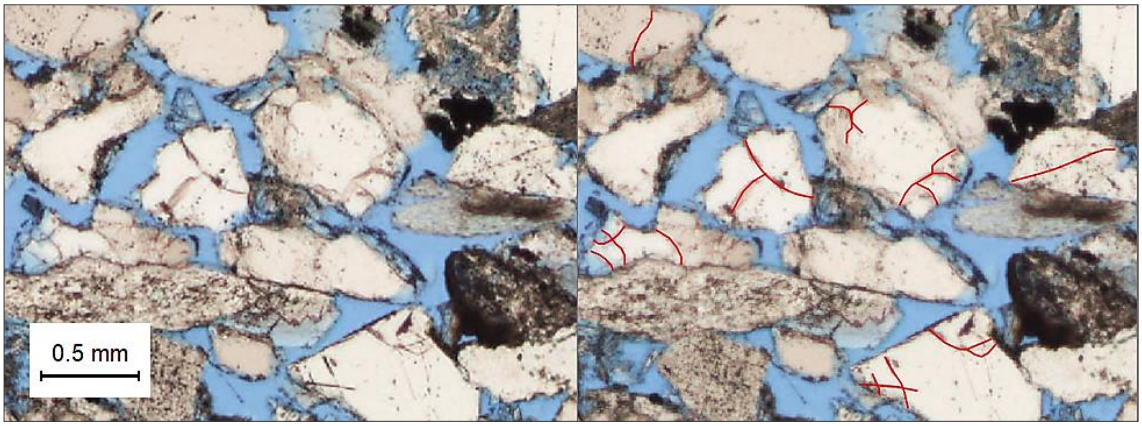

Figure 27. Undeformed Bleurswiller sample BW-00, with large blue pore spaces in between grains and indicated red cracks within large feldspar- and quartz grains

Bleurswiller. The cracks are well distributed throughout the sample and have an average crack length of 85 and 115 micron. The microcracks of both sections show a slight preferred orientation (**Table 3**), whereas ~35% of the cracks in section BW-02-1-a have orientations between 30° and 75° and ~27% of the cracks in section BW-02-2-b between 90° and 120°. Again it should be kept in mind that the performed microstructural analysis is a 2D image and the 3D image could differ from the results listed here.

Orientation (°)	Distribution cracks (% of total cracks)		
	BW-00	*BW-02-1-a*	*BW-02-2-b*
0-15	6.3	4.3	6.0
15-30	8.3	6.3	7.1
30-45	9.5	10.7	6.9
45-60	7.4	11.6	8.0
60-75	10.4	13.0	8.6
75-90	10.2	9.7	8.4
90-105	7.7	10.1	13.6
105-120	9.1	9.7	13.4
120-135	8.9	7.5	9.8
135-150	7.3	7.7	6.5
150-165	7.5	5.1	7.6
165-180	7.4	4.3	4.1

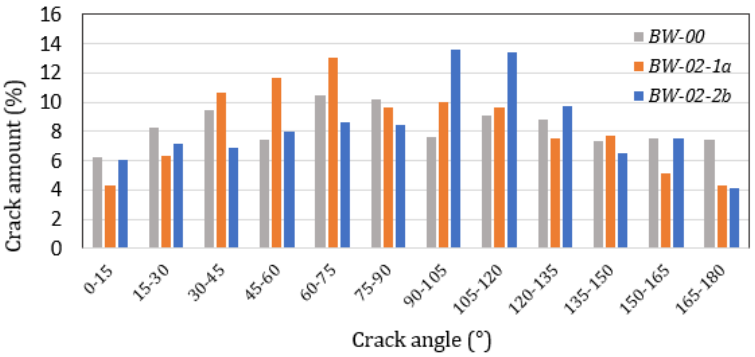

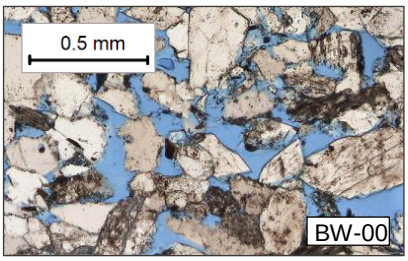

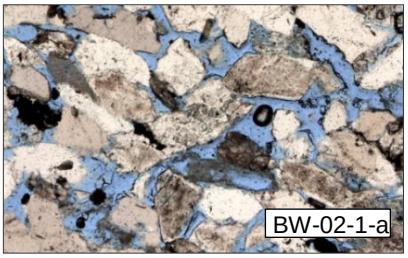

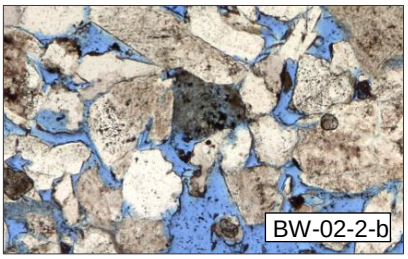

***Table 3**. Crack distribution data of samples BW-00, BW-02-1-a and BW-02-2-b and example thin section images.*

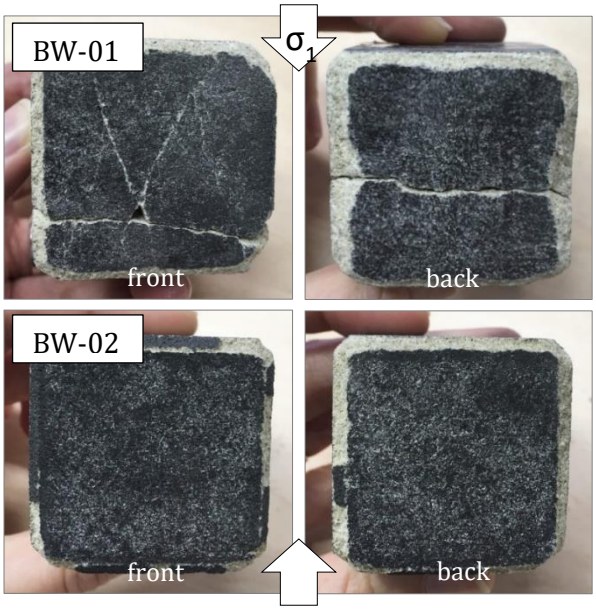

Figure 28. *Samples BW-01 (top) and BW-02 (bottom) post-deformation. Sample BW-01 shows multiple fractures: one large horizontal fracture cutting through the entire sample and four fractures dipping towards two opposite directions placed in a 15-30° angle, whereas sample BW-02 (right) shows no macroscopic deformation on both sides of the sample*

3.3.3 True triaxially deformed Bleurswiller sandstone BW-01

After sample BW-01 was taken out of the true triaxial multi-anvil apparatus, multiple macroscopic fractures in different orientations present in the sample are observed (**Figure 28**). The sample contains two sets of fractures, one large horizontal fracture cutting through the lower part of the cube and roughly four fractures dipping with a 15-30° angle towards two opposite directions. Whereas the horizontal fracture crosses the entire sample, the other fractures are only observed at one side of the sample. After the cubic sample was cut in the same way as sample BW-02, a complicated internal fracture system is exposed (**Figure 29**). The fracture system consists of one large horizontal fracture crosscutting multiple large- and small scale fractures, mostly dipping with an angle of 45-75°. The main fractures can be easily identified and are indicated in **Figure 29**.

Figure 29. *Macroscopic overview of the internal fracture system of sample BW-01. One large horizontal fracture cutting the lower part of the sample is observed, crosscutting multiple large- and small scale fractures indicated in red.*

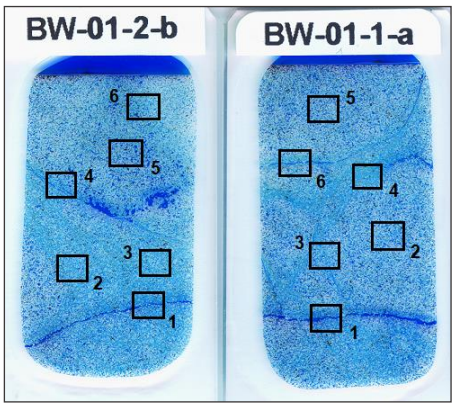

Figure 30. *Thin sections BW-01-1-a and BW-01-2-b. Specific areas are labelled and are visually inspected, of which the results can be found in* ***Figure 31*** *and* ***Figure 32****.*

During microstructural analysis of samples BW-01-1-a and BW-01-2-b (**Figure 30**) it is observed that grains with a major amount of intragranular cracks are present, leading to breakage of grains into small fragments, described as grain crushing. Both grain crushing and intragranular grain fracturing are widespread throughout the sample. Observed grain crushing did not only occur around the main fractures, but can also be observed throughout both the entire sections. Both sections have relatively low porosity and narrow pore spaces compared to the undeformed BW-00 sample. Sample BW-01-1-a shows grain crushing along larger- and smaller scale fractures (**Figure 31-1 , 31-3** and **31-6**). In between the fractures, areas with minor grain crushing are present (**Figure 31-2, 31-4**). These areas are small in size and closely adjoin macroscopically similar areas which are severely damaged (**Figure 31-5**). Sample BW-01-2-b shows a similar damage distribution. Again, grain crushing is observed along the larger- and smaller scale fractures (**Figure 32-1, 32-3** and **32-4**). In between the main fractures, there are small areas which show minor- to major grain damage (**Figure 32-2, 32-5** and **32-6**). Since both thin sections show abundant grain damage throughout almost their entire surfaces and differ microstructurally from sample BW-02, they will not be used as crack density reference for the deformed Bleurswiller sandstone.

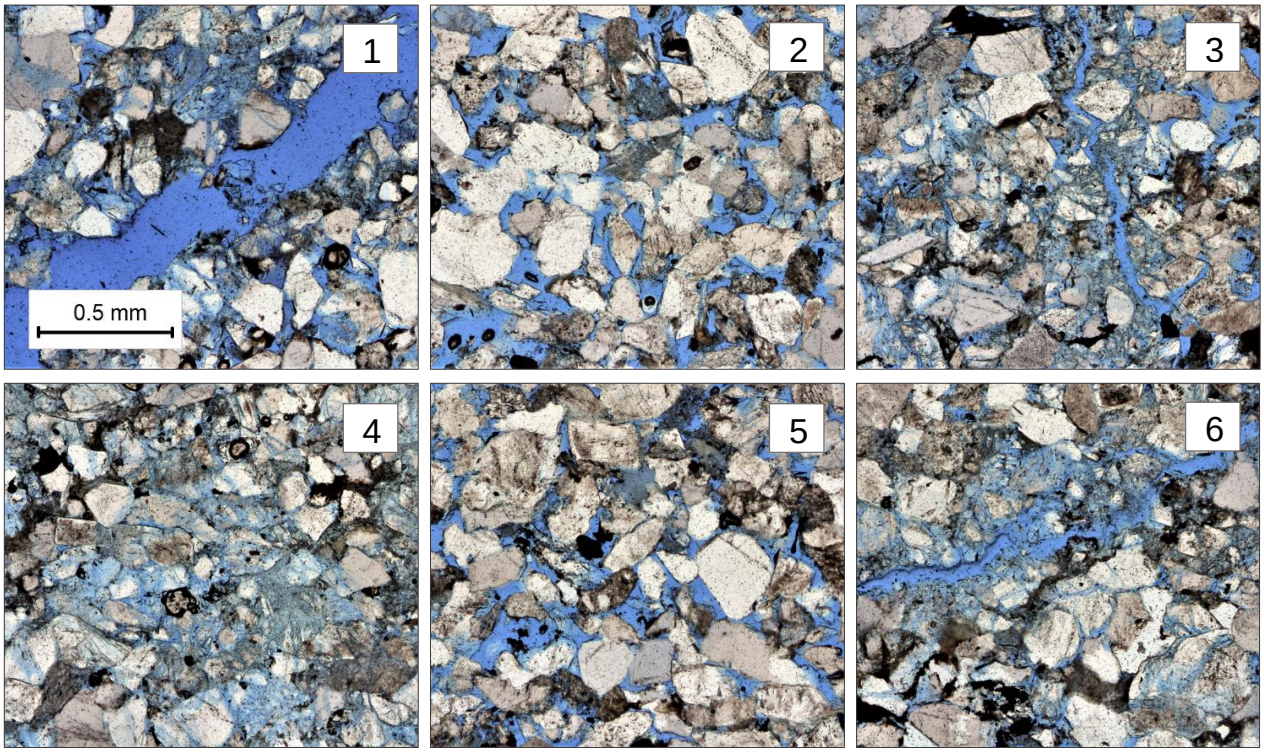

Figure 31. *Six areas of sample BW-01-1-a, showing: 1) large horizontal fracture with crushed grains within- and around the fracture area, 2) minor damaged area in between the main fracture system, 3) small-scale fracture surrounded by crushed grains, 4) major damaged area in between main fractures, 5) minor damaged area at the top of the sample, and 6) small-scale fracture surrounded by crushed grains.*

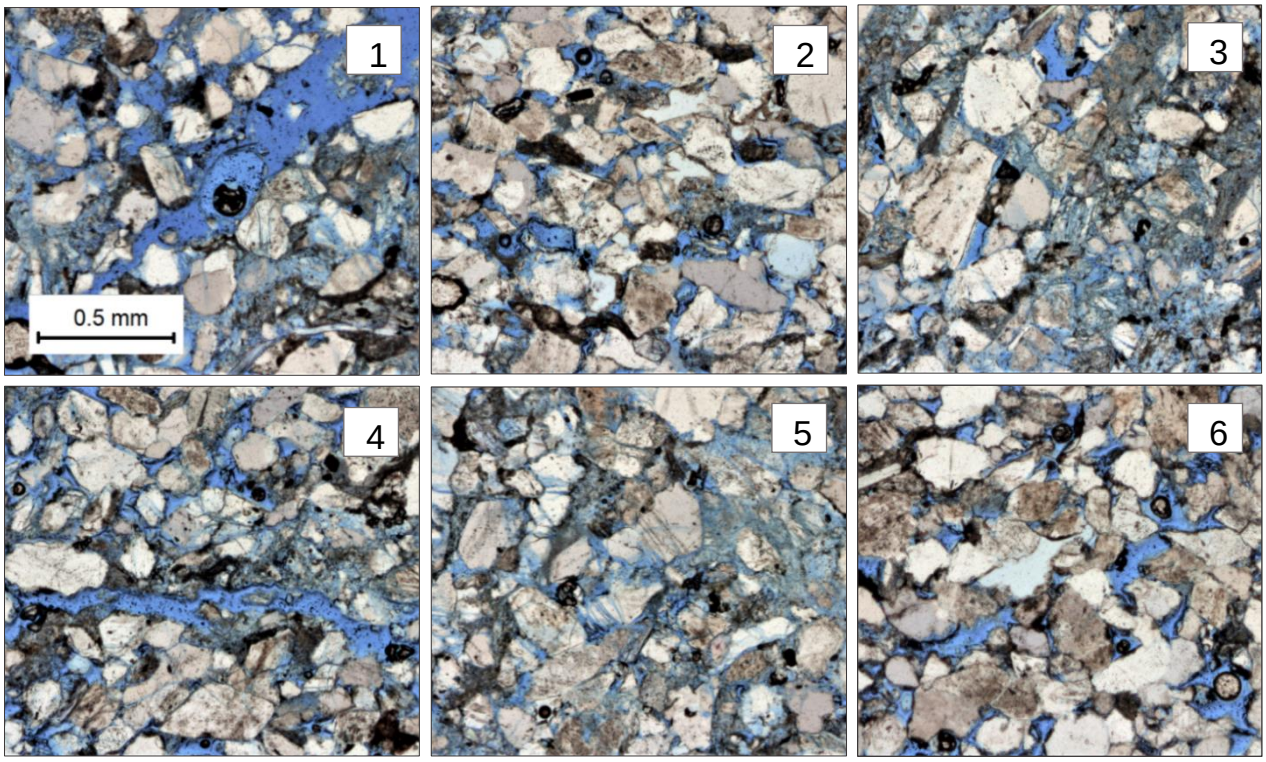

Figure 32. *Six areas of sample BW-01-2-b, showing: 1) large horizontal fracture with crushed grains within- and around the fracture area, 2) minor damaged area in between the main fracture system, 3) and 4) small-scale fractures surrounded by crushed grains, 5) major damaged area at a distance from the main fractures, and 6) minor damaged area at the top of the sample.*

4. Discussion

4.1 BW-01 behaviour

Whereas true triaxially deformed samples BW-02 and BW-03 show similar strain- and acoustic velocity results, sample BW-01 deviates greatly and shows a complex geometry of fracture planes after the experimental procedure. Strain measurements during the deviatoric stage already reveal values up to six times as high as the other two samples in all principal directions, but shows a similar increasing- and decreasing strain trend during subsequent loading and unloading. Furthermore, large permanent strain values (>2.0%) after both the deviatoric stage and the hydrostatic stage are observed in the Z-direction. Additionally, much lower acoustic velocities compared to the other two samples are monitored. All experimental data of sample BW-01, supported by the macroscopic fracture planes observations, indicate that sample failure occurred during the experimental procedure. *Baud et al. (2015)* observed a progressive transition in failure mode of the Bleurswiller sandstone with increasing effective pressure. At low confinement (10-20 MPa), shear bands at angles of ~30° (relative to σ_1) developed, which are recognized in the conjugate fracture sets of the BW-01 sample. This is in agreement with the orientation of the macroscopic fracture plane of conventional triaxially deformed sample BW-06, developed during failure by deviatoric loading under confining pressure of 15 MPa. The conjugate fractures are crosscut by one large horizontal fracture cutting through the entire cube. *Baud et al. (2015)* observed that under high confinement (70-90 MPa) failure of Bleurswiller showed a mixed mode of high-angle shear bands and compaction bands subperpendicular to σ_1. Since high confinement (~110 MPa) has only been induced during the hydrostatic stage and the nearly-horizontal orientation suggest the unlikelihood of formation during deviatoric loading, it is reasonable to suggest that the failure plane originated during the hydrostatic stage. Nevertheless, no clear evidence can be found for the origin of this failure plane.

Browning et al. (*2017*) stated that ultimate failure commonly occurs after a weakening period following the peak stress. Since intense damage generation of BW-01 most likely already occurred during early deformation stages whereas no failure was induced during deformation of the other two samples, it is reasonable to suggest that the BW-01 behaviour is explained by processes which have weakened the sample. Comparison of the conventional triaxial tests performed on dry- and wet Bleurswiller sandstone (BW-06 and BW-10) show failure of the wet Bleurswiller sample at much lower differential stress than the dry sample (respectively around 67 and 87 MPa differential stress). This weakening effect of water has also been observed by *Fortin et al.* (*2005*) for the Bleurswiller sandstone. Since the differential stress of sample BW-01 during deviatoric loading did not exceed values of 60 MPa, this closely corresponds to the maximum differential stress observed for the wet BW-10 sample. Furthermore, microstructural analysis of samples BW-06 and BW-10 indicates that limited water content induces more distributed grain failure. The large extent of distributed grain damage observed during post-deformation analysis of sample BW-01 together with the observed mechanical response suggests that weakening by water could have been an important factor accounting for the sample failure. Since samples used for the true triaxial experiments have only been dried in the oven for a few hours, this may have not been sufficient to completely dry the material. Nevertheless, if the rock would be fluid-saturated, P-wave velocities would show higher values compared to dry rocks (*Gassmann 1951*). This has not been observed for sample BW-01, whereas it shows significantly lower P-wave velocities compared to BW-02 and BW-03. Therefore, other weakening effects which could possible influence the observed BW-01 failure behaviour should be considered. *Fortin et al.* (*2005*) showed

that mineral composition is an important parameter controlling sandstone behaviour, whereas clay minerals can lower the yield limit of the Bleurswiller sandstone. This has also been observed by *Sayers and Munster* (*1991*) for the Berea sandstone, who furthermore presented that sandstone samples with a higher clay content showed substantially lower acoustic velocities compared to samples with lower clay content. However, it would not be reasonable that small compositional differences between the experimentally deformed Bleurswiller samples would explain great differences in sample behaviour. Since strain- and velocity observations of sample BW-01 are difficult to explain looking at sample properties only, it must be taken into consideration that differences could be caused by the interplay between initial sample properties and experimental flaws. For instance, minor mistakes could have been made during preparation for the experimental procedure, such as inaccurately levelling of the sample and pistons, causing an uneven load distribution during the experimental procedure. Furthermore, poor strain- and pulse signal reception due to bad conductivity between the sample and the signal receivers could have influenced the quality of the output data. Because of the uncertain nature of the observed deviating BW-01 results and the great resemblance between the data of samples BW-02 and BW-03, the BW-01 data will not be taken into consideration during further discussion.

4.2 Quantitative crack model

Since wave velocities change in the presence of microcracks, acoustic velocity measurements can be used to model evolving rock crack densities. *Sayers and Kachanov* (*1995*) obtained a method whereas changes in acoustic wave velocities can be used to calculate a compliance tensor, which is subsequently converted to crack density tensor. Each crack in the solid medium is regarded as being embedded in a solid with the overall properties of the cracked body (*Browning et al. 2017; Kachanov 1992; Sayers and Kachanov 1995*). *Browning et al.* (*2017*) applied the *Sayers and Kachanov* model for quantitative microcrack characterization to velocity measurements during triaxial compression of the Darley Dale sandstone. In this section, simple crack density evolution models obtained by following the approach presented by *Browning et al.* (*2017*) will be presented. General underlying expressions for an elastic solid containing microcracks will not be discussed but can be found in *Sayers and Kachanov* (*1995*).

Initially, all rocks show elastic anisotropy due to oriented microcracks, which can be expressed in terms of a second-rank tensor according to *Sayers and Kachanov* (*1995*),

$$\gamma_{ij} = \frac{3E_0(2-\nu_0)}{32(1-\nu_0^2)}\alpha_{ij} \qquad (2)$$

with α being the crack density in a given structural direction (*i* and *j*), E_0 the Young's modulus and ν_0 the Poisson's ratio in a homogenized background medium. It is assumed that stress dependence of the elastic properties of a sandstone is due to deformation of discontinuities within the rock, such as grain boundaries and microcracks (*Sayers 2002*). The macroscopic strains of a sandstone are related to the macroscopic stress components by the effective compliance tensor S_{ijkl},

$$\varepsilon_{ij} = S_{ijkl}\sigma_{kl} \qquad (3)$$

Furthermore, the average strain in an elastically homogeneous volume element containing cracks can be represented as the sum of the matrix compliance (related to the deformation of the matrix) and additional compliance caused by the presence of cracks (*Sayers and Kachanov 1995*):

$$\varepsilon_{ij} = \left(S^0_{ijkl} + \Delta S_{ijkl}\right)\sigma_{kl} \qquad (4)$$

This way, the elastic compliance of the sandstone can be written as

$$S_{ijkl} = S^0_{ijkl} + \Delta S_{ijkl} \qquad (5)$$

For modelling the crack density evolution of the Bleurswiller sandstone, the P-wave velocities of samples BW-02 and BW-03 in the three main structural directions are used. *Browning et al.* (*2017*) stated that data from conventional triaxial experiments ($\sigma_1 > \sigma_2 = \sigma_3$) displays a cylindrical transverse isotropy (CTI) crack distribution, represented by two independent crack population (N_1 and N_3) and two crack densities (α_1 and α_3). Although conventional triaxial experiments have been performed on the Bleurswiller samples, the acoustic wave velocity data shows that the velocities in the X- and Y-directions contains minor differences. Although velocity differences are relatively small, three independent crack populations (N_1, N_2 and N_3) can be recognized and will be modeled: α_1 in the Z-, α_2 in the Y- and α_3 in the X-direction.

Following the steps proposed by *Browning et al.* (*2017*) for the true triaxial case, assuming three individual crack populations (with $\alpha_1 \neq \alpha_2 \neq \alpha_3$), looping through the main orientations (Z=1, Y=2 and X=3) gives

$$\begin{aligned} \Delta S_{1111} &= \alpha_1 \\ \Delta S_{2222} &= \alpha_2 \\ \Delta S_{3333} &= \alpha_3 \end{aligned} \qquad (6)$$

with ΔS_{ijkl} representing the tensorial change in compliance due to the associated induced crack damage as described in equation (5). For simplifying the compliance tensor, Voigt notation can be used, whereas the four subscripts of the compliance and stiffness tensors are reduced to two (*Mavko 2010*). Each pair of indices *ij(kl)* can be replaced by one index *I(J)*, giving $S_{IJ} = S_{ijkl}$ and $C_{IJ} = C_{ijkl}$. Therefore, we get

$$\begin{aligned} \Delta S_{11} &= \alpha_1 \\ \Delta S_{22} &= \alpha_2 \\ \Delta S_{33} &= \alpha_3 \end{aligned} \qquad (7)$$

The Voigt matrix of elastic stiffness is represented by $C_{IJ} = S_{ij}^{-1}$ and may be calculated from the compressional P-wave velocities along the principal axes in the damaged rock (*Sayers and Kachanov 1995*),

$$\begin{aligned} C_{11} &= \rho V_{11}^2 \\ C_{22} &= \rho V_{22}^2 \\ C_{33} &= \rho V_{33}^2 \end{aligned} \qquad (8)$$

whereas the rock density ρ will be assumed to be constant since the crack volume is considered to be small. Following *Browning et al.* (*2017)*, it is seen that the crack densities in the three principal directions can be written as

$$\alpha_1 = \left(\frac{1}{C_{11}}\right) - S_{11}^0$$
$$\alpha_2 = \left(\frac{1}{C_{22}}\right) - S_{22}^0 \qquad (9)$$
$$\alpha_3 = \left(\frac{1}{C_{33}}\right) - S_{33}^0$$

4.3 Crack density analysis: quantitative modelling and microstructural results

Previously derived equations are used to evaluate changing crack densities during deviatoric- and hydrostatic loading and unloading of samples BW-02 and BW-03 using measured P-wave velocities. In **Figure 33** and **Figure 34** the crack density change of samples BW-02 and BW-03 are plotted against changing axial strain. Crack density change at the start of the deviatoric- and hydrostatic loading stages is assumed to be zero. Crack densities α_1, α_2 and α_3 represent densities in respectively the Z-, Y- and X-directions. Decreasing crack density values indicate a decrease in the microcrack population, increasing values represent an increasing microcrack population.

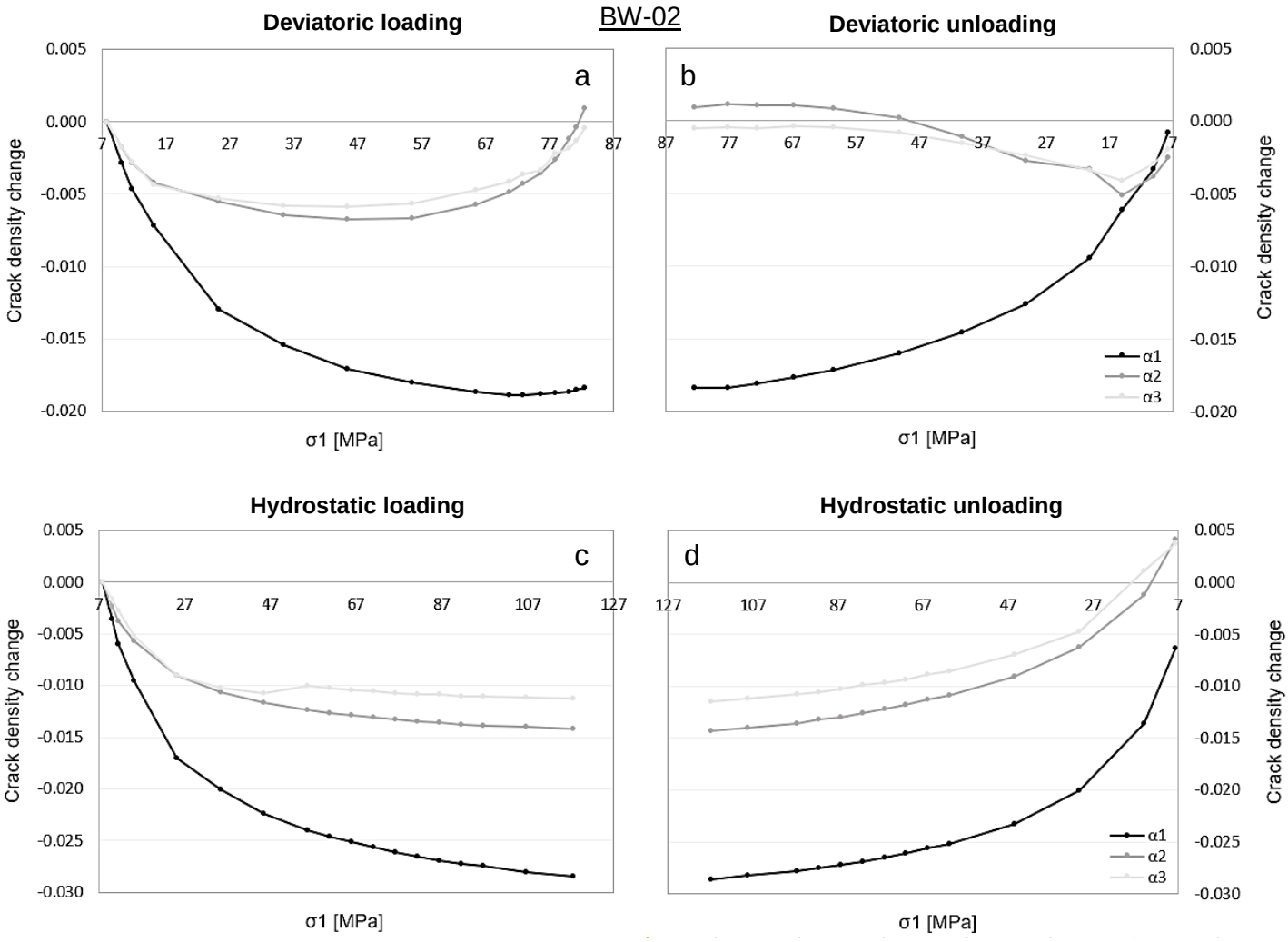

Figure 33*. Crack density evolution of sample BW-02 during deviatoric- and hydrostatic loading. Crack densities α_1, α_2 and α_3 represent densities in respectively the Z-, Y- and X-directions. Decreasing crack density values indicate a decrease in the microcrack population, increasing values represent an increasing microcrack population.*

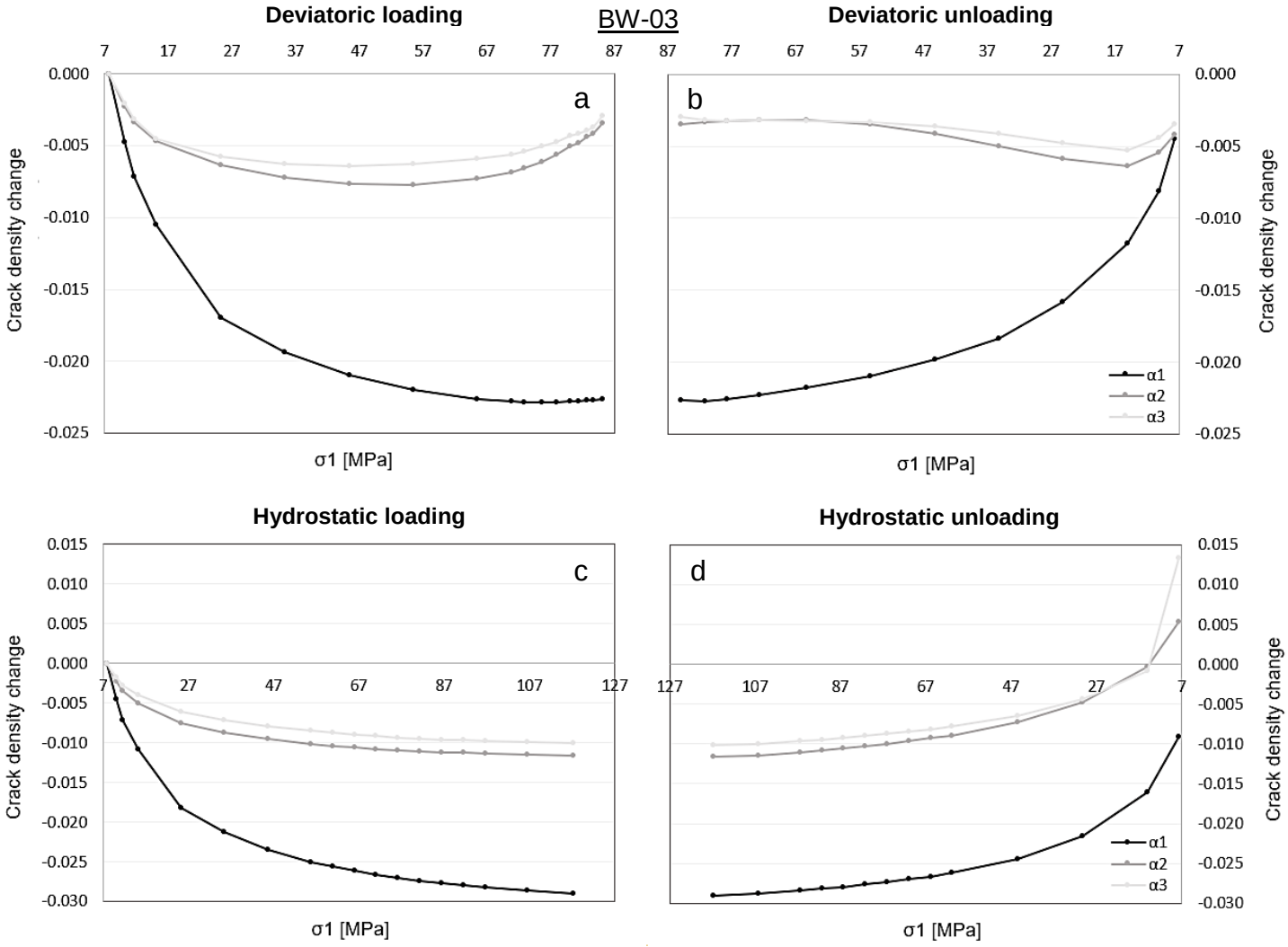

Figure 34. *Crack density evolution of sample BW-03 during deviatoric- and hydrostatic loading. Crack densities α_1, α_2 and α_3 represent densities in respectively the Z-, Y- and X-directions. Decreasing crack density values indicate a decrease in the microcrack population, increasing values represent an increasing microcrack population*

Deviatoric loading of both samples and increasing σ_1 causes closure of cracks with corresponding decreasing crack densities (**Figure 33a, Figure 34a**). In the Z-direction, the closure the N_1 population cracks continues, whereas the closure of the N_2 and N_3 population ends around ~50-55 MPa, after which crack densities start to increase again. This is in agreement with the convention that under conventional triaxial stress, cracks can grow with their minor axis in any orientation in the X- or Y-plane (*Browning et al. 2017*). At the end of the deviatoric loading stage, crack densities in the Z-direction (α_3) are significantly lowered. During deviatoric unloading, the crack density in the Z-direction steadily increases again due to elastic reopening of cracks, towards values somewhat lower than the original crack density (**Figure 33b** and **Figure 34b**). Densities in the X- and Y-directions show less rapid changes, with a small increase followed by a decrease the last 15 MPa of unloading. Hydrostatic loading shows decreasing crack densities in all directions (**Figure 33c** and **Figure 34c**), with small crack density decrease in the X- and Y-directions. These crack density decreases reflect closure of microcracks which were induced during the deviatoric stage. During the first 30-50 MPa of hydrostatic loading, crack densities first rapidly decreases. After ~60

MPa the crack density decrease continues, but very slowly. Hydrostatic unloading shows a reversed trend, with slowly increasing crack densities until ~60 MPa followed by more rapidly increasing crack densities due to elastic crack reopening. Crack density values after the entire experimental procedure show higher values in both the X- and Y-directions than at the beginning of the hydrostatic stage, indicating induced permanent damage.

The induced permanent damage deformation, observed in the strain-, acoustic velocity- and in the quantitative crack density data, is not supported by microstructural crack mapping results. Microstructural crack mapping showed lower crack densities for the two deformed BW-02 samples (BW-02-1-a and BW-02-2-b) compared to the undeformed BW-00 sample. Since samples BW-02 and BW-03 both show a permanent volumetric strain of ~0.3% and a difference in acoustic wave velocities before- and after the experimental procedure, it is certain that a small amount of permanent deformation was induced. Differences in observations can originate from the quantitative crack density model. This model assigns all acoustic velocity changes to (elastic) microcrack closure and opening and does not take into account other important mechanisms influencing the velocity, such as porosity changes, frictional sliding between grains and the effect of inter-granular contacts (*Scott Jr et al. 1993; Walton 1987*). Although the modelling results provide a nice visualization of relative crack density changes, they are not fully representative of absolute crack densities. Microstructural analysis does not show a crack density increase after the experimental procedure, but reveals a porosity reduction of ~10% after full hydrostatic unloading. This indicates the likelihood that deformation is largely accommodated by pore collapse. Furthermore, observed differences can arise from the microstructural crack mapping results. During crack mapping using optical microscopy images multiple variables influence the quality of the results, such as optical image resolution, thin section quality and thin section composition. Therefore, optical image quality and thin section composition have most likely been of major influence on the final crack density results. Whereas microcracks are easiest to recognize in quartz grains, the high clay- and feldspar content of the Bleurswiller sandstone makes identification difficult due to optical properties complicating crack recognition. Additionally, permanent deformation could be accommodated by weaker areas within the 3D 43 x 43 mm sized sample, which may not be included in the 2D thin sections of only ~9.5 x 8.0 mm.

4.4 Changes in acoustic velocities as implication for the previously applied maximum stress

To explore if the in-situ state of stress of a reservoir can be determined by measuring P- and S-wave velocities during true triaxial experiments, the question if acoustic velocity measurements of the hydrostatic stress stage can reveal the previous deviatoric state of stress of the sample will be first addressed. First, evidence showing that permanent deformation was induced during deviatoric loading will be discussed, followed by predictions and results for retrieving the previous maximum applied deviatoric stress during hydrostatic loading.

4.4.1. Evidence for induced permanent deformation during deviatoric loading

The first step of the experimental procedure served to induce permanent damage at known conditions during deviatoric loading. To address the research question, it is necessary to verify if permanent damage has indeed been induced on the Bleurswiller samples. When combining the 3D acoustic velocity measurements and strain data of samples BW-02 and BW-03, a complicated pattern of anisotropic strain- and acoustic velocity changes is observed, caused by changes in the elastic properties of the sample. This

stress-induced velocity anisotropy arises by the presence of a non-hydrostatic stress-field, since the response of a discontinuity within the rock to a certain stress depends on the discontinuity orientation relative to the applied stress field (*Sayers 2002*). Elastic property changes are the result of the interplay between different mechanisms, such as the trade-off between elastic crack closure and pore collapse mechanisms causing compaction, and mechanisms such as microcracking and grain crushing causing sample dilatation (*Fortin et al. 2005; Wong and Baud 2012*). Looking at the acoustic velocity data of the deviatoric stage, a P- and S-wave velocity decrease in the X- and Y-direction after ~50 MPa of deviatoric loading is observed. The velocity decrease provides potential evidence for possible induced experimental damage due to microcracking and pore collapse, causing a reduction in the speed of acoustic waves. Nevertheless, acoustic velocities are not only influenced by microcracking and porosity changes, but are also largely controlled by mechanisms such as frictional sliding between grains and the effect of inter-granular contacts. For instance, *Bernabe and Brace* (*1990*) suggested that within a porous sandstone, not microcracking within grains but frictional sliding between grains is most likely responsible for the rock dilatancy (*Scott Jr et al. 1993*). Therefore, P-and S-wave measurements cannot stand alone in providing evidence for experimentally induced sample damage. However, when looking at the strain data of samples BW-02 and BW-03, it is clear that permanent deformation has been induced. Observed are increased strain values after complete unloading compared to their starting values, indicating that full strain recovery did not take place and permanent deformation was induced. Whereas microstructural analysis does not show any signs of increased microcrack densities in the deformed Bleurswiller samples, observed extreme porosity reduction of ~10-15% indicates that pore collapse has likely been the main mechanism resulting in permanent deformation. Additionally, to obtain more information about the onset and evolution of new crack damage caused by inelastic processes during experimental loading, Acoustic Emission measurements can be used (e.g. *Browning et al. 2017*). Combining AE measurements with acoustic Vp and Vs measurements in all directions can be a useful tool for monitoring the anisotropic closure and/or opening of cracks.

4.4.2 Retrieving the previous maximum applied stress: predictions

To determine if the previous maximum applied stress can be retrieved by introducing a subsequent hydrostatic stress stage, it is important to start with exploring the expected influence of the previously induced stress imprint on the acoustic wave velocity behaviour during hydrostatic loading and unloading. Since hydrostatic loading is isotropic in nature, it will always give rise to compaction due to continuous decreasing porosity, causing an increase in acoustic velocities in all principal directions of roughly similar size. When a hydrostatic load is applied the previously induced heterogeneities during deviatoric loading, such as oriented microcracks, will be reduced and P- and S-wave velocities will increase. Since the maximum applied stress during hydrostatic loading exceeds the maximum stress of the deviatoric stage (respectively 117 MPa and 85 MPa), previously induced heterogeneities are likely minimized around the maximum applied deviatoric stress. Therefore, it is expected that acoustic velocities during hydrostatic loading will show a rapid increase prior to 85 MPa, whereas around 85 MPa the increase will become less. Since heterogeneities during the deviatoric stage are mostly generated in the X- and Y-directions (indicated by decreasing Vs and Vp in the X- and Y-directions), Vs and Vp data in these directions from the hydrostatic stage provide the most information about minimization of heterogeneities.

Further predictions can be made for the P- and S-wave anisotropy and anisotropy rate of change. Anisotropy is highest at low pressure due to differences in initial microcrack orientations, anistropically distributed pore spaces and compositional differences influencing the acoustic velocities (*Kern 2011*). A continuous decreasing anisotropy supports the idea that, during hydrostatic loading, pore- and crack closure takes place and the opening of new microcrack is inhibited due to the equal load in all directions. Since anisotropy is highest at low pressure, a rapid velocity anisotropy decrease is induced during early parts of loading and the final part of unloading. Other minor acoustic velocity anisotropies mostly arise due to differences in mineralogy, pore space distribution and fluid saturation (*Winkler and Murphy 1995*). As previously suggested, induced heterogeneities during deviatoric loading will likely be minimized around ~85 MPa (the maximum applied deviatoric stress). Therefore, when looking at the Vp and Vs anisotropy, it is expected that continuous decreasing anisotropy during hydrostatic loading would be around its minimum ~85 MPa, whereas loading beyond the maximum applied stress only causes a minor anisotropy decrease. Additionally, since only minor anisotropy changes are expected beyond ~85 MPa, the P- and S-wave anisotropy rate of change would show constant values around 0 %/MPa. Anisotropy changes during unloading are expected to be less, since heterogeneities such as microcracks are inelastically closed during hydrostatic loading. Cracks are mostly expected to be elastically reopened during the last part of unloading, causing the anisotropy to stay minimal during the first part of unloading. Therefore, it is less likely to observe the stress imprint during subsequent hydrostatic unloading.

4.4.3 Retrieving the previous maximum applied stress: results

Taking into account the previously stated predictions, the acoustic velocity data can be analysed to test if the previous maximum applied stress (85 MPa) can be retrieved by introducing a subsequent hydrostatic stress stage. Looking at the Vp and Vs data, increasing velocities are observed during hydrostatic loading, with velocity changes becoming less in all principal directions during further stress increase. The velocity change becomes significantly smaller in the X- and Y-directions during early hydrostatic loading stages. Although further hydrostatic loading shows very small velocity changes indicating that the occurrence of heterogeneities is minimized, no clear P- or S-wave velocity change minimum is observed around 85 MPa. Subsequent unloading also shows no clear signs of the previous induced maximum stress.

Looking at the Vp- and Vs anisotropy, a clear decrease in anisotropy is observed during increasing hydrostatic load. Initial hydrostatic loading causes a rapid velocity anisotropy decrease with corresponding high rate of change due to a rapid decrease in the amount of heterogeneities present in the rock. Subsequent hydrostatic loading causes further anisotropy decrease. Whereas the Vp anisotropy shows no clear minimum and continues to decrease until the end of the hydrostatic loading stage, the Vs anisotropy in the Y-direction of BW-02 and BW-03 both display a minima around 85 MPa. However, this is not observed for the X-direction. Nevertheless, from 85 MPa, the A-Vs in all three direction show stable values which only show minor anisotropy changes. The start of stable Vs anisotropy values corresponds to the previously maximum applied stress of 85 MPa during deviatoric loading and indicates the point at which the amount of heterogeneities is minimized, as previously expected. During unloading, both Vp and Vs anisotropy values stay constant until ~60 MPa, whereas heterogeneities elastically reopen again reflected by a subsequent anisotropy increase.

		KB-1c	KB-1a
Deviatoric	Pc (MPa)	15	15
	$\sigma_{1\,max}$ (MPa)	155	138
Hydrostatic	$\sigma_{1\,max} = \sigma_2 = \sigma_3$ (MPa)	208	188

Table 4. *Experimental conditions of experiments performed by Trahwiwit (2017) on 6% porosity Beberthal sandstone.*

The Vs- and Vp anisotropy rate of change data show similar results. An initial rapid A-Vp rate of change during the first part of hydrostatic loading approaches small rates of -0.1 to -0.05 %/MPa around 60 MPa. From 60-85 MPa, the A-Vp rate of change still slightly decreases and from 85 MPa on, the Vp rate of change obtains minimum values of -0.05 to -0.025 %/MPa for both BW-02 and BW-03. The A-Vs rate of change values show varying values in the three principal directions. Again, initial loading initiates a rapid A-Vs rate of change, which decreases during further loading. All follow roughly the same trend towards smaller rate of change values, whereas they seem to converge and intersect around 85 MPa. This can mostly be observed when looking at the data of sample BW-02, with values becoming nearly zero (rate of change values in between 0.044 and 0.001 %/MPa) and following the same trend from 85 MPa. Subsequent unloading shows constant A-Vs rate of change until ~50 MPa, which afterwards increase again.

To further explore if the previous maximum applied stress can be retrieved by introducing a hydrostatic stress stage, results from experiments performed by *Trahwiwit (2017)* are considered. An identical experimental procedure of initial deviatoric loading and unloading, followed by a hydrostatic stage has been introduced on Beberthal samples of ~6% porosity (samples KB-1c and KB-1a). Experimental conditions of samples KB-1-c and KB-1a are listen in **Table 4**. Results of the Vp- and Vs anisotropy and their rate of change during hydrostatic loading and unloading are found in **Figure 35**, **Figure 36** and **Figure 37**. When looking at the A-Vp, similar trends as for the Bleurswiller samples are observed. Hydrostatic loading initiates a decrease in anisotropy due to a decreasing amount of heterogeneities (**Figure 35a**). No clear

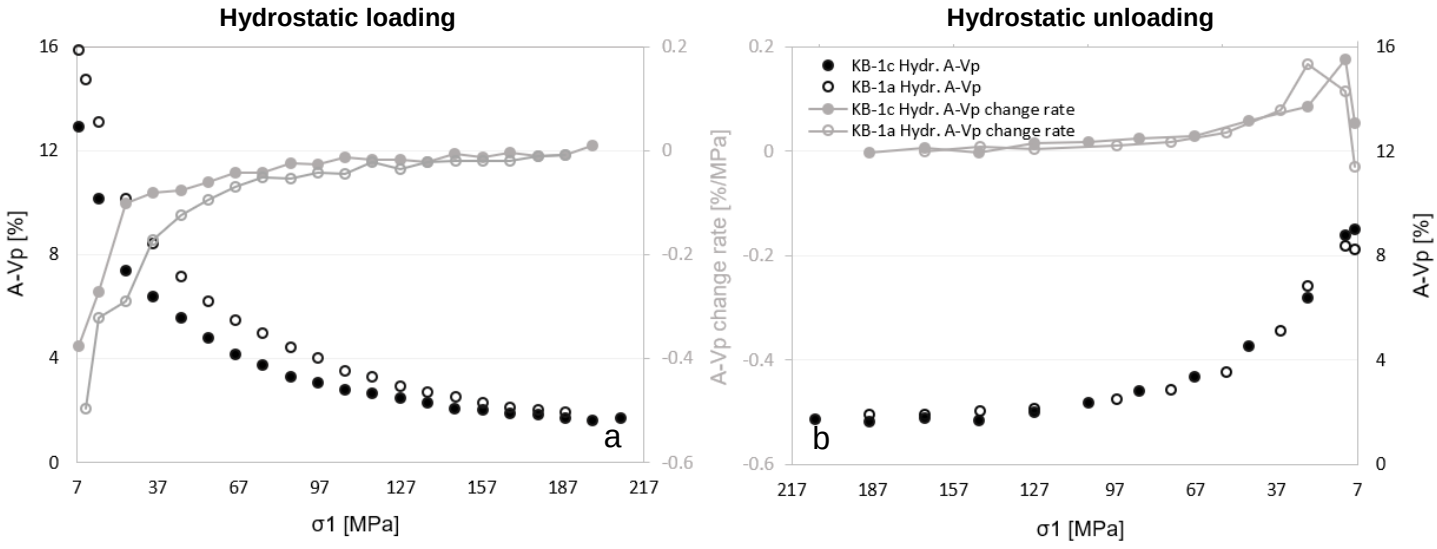

Figure 35. *Vp-anisotropy and Vp-anisotropy rate of change of Beberthal samples KB-1c and KB-1a, during deviatoric- and hydrostatic loading and unloading. Vp-anisotropy (A-Vp) is reflected by individual circles, A-Vp rate of change by connected circles. Positive Vp rate of change values reflect increasing anisotropy, negative values reflect decreasing anisotropy.*

minimum is observed and the anisotropy keeps on decreasing during continuous hydrostatic loading. The Vp anisotropy rate of change (**Figure 35a**) shows roughly constant values after around 130 MPa of loading and minimum values around the maximum applied deviatoric stress for both samples (155 MPa for KB-1c and 138 MPa for KB-1a). This is also observed during hydrostatic unloading, with a constant rate of change during the initial part of unloading, whereas values start to increase again after the maximum applied deviatoric stress is obtained (**Figure 35b**). When looking at the Vs anisotropy, different results are observed. Both samples show rapidly decreasing A-Vs values in the X-direction during initial loading which subsequently increase again (~ 75 MPa for KB-1a and ~95 MPa for KB-1c), followed by a further decrease (**Figure 36a** and **36c**). Around 135 MPa and 155 MPa for respectively KB-1a and KB-1c, minimum anisotropy values are obtained. In the Z-direction, minimum A-Vs is also observed for both samples around

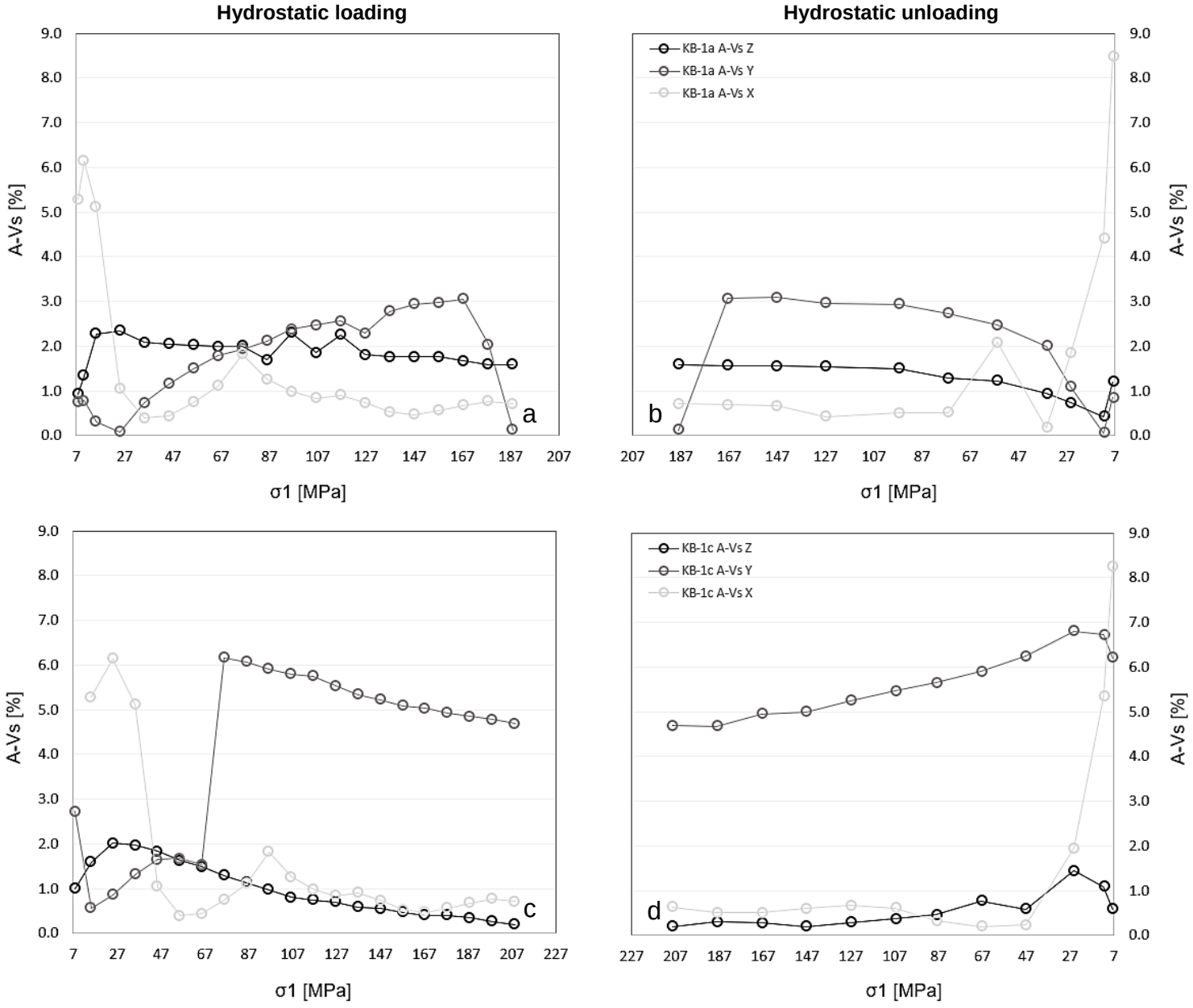

Figure 36. *Vs-anisotropy of Beberthal samples KB-1a (top) and KB-1c (bottom), during hydrostatic loading and unloading. A-Vs has been calculated for all principal directions (X in light grey, Y in grey, Z in black).*

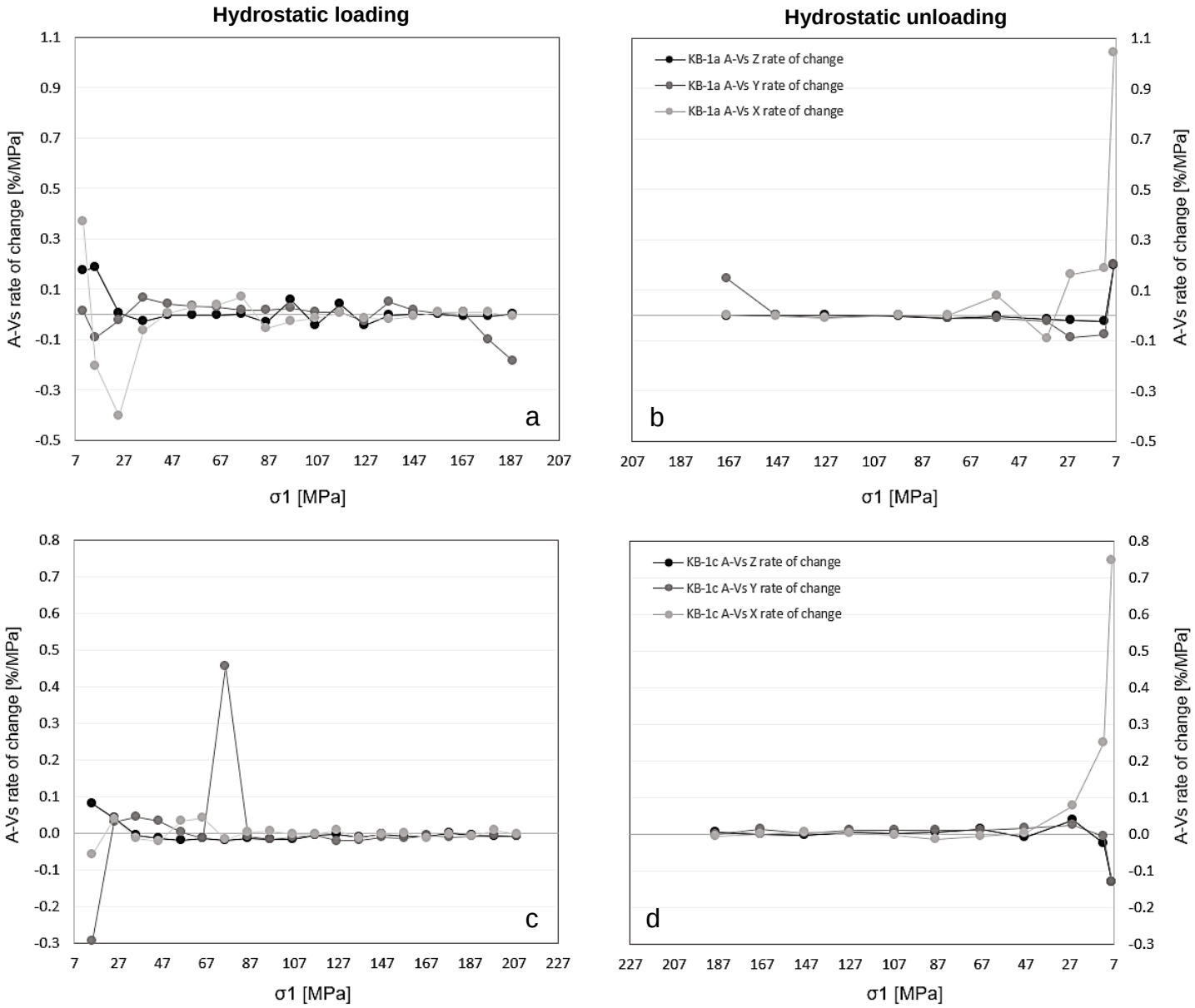

Figure 37. *Vs-anisotropy rate of change of Beberthal samples KB-1a (top) and KB-1c (bottom), during hydrostatic loading and unloading. A-Vs has been calculated for all principal directions (X in light grey, Y in grey, Z in black). Positive A-Vs rate of change values reflect increasing anisotropy, negative values reflect decreasing anisotropy.*

the same point as in the X-direction. Anisotropy in the Y-direction does not show a clear minimum and seem to be very variable (**Figure 36a** and **36c**). Furthermore, the A-Vs in all directions during unloading do not show any indication for the previously applied maximum deviatoric stress (**Figure 36b** and **36d**). When looking at the A-Vs rate of change values, high rates at the beginning of loading rapidly change into extremely small rates approaching zero (**Figure 37a** and **37c**). During subsequent loading, the Vs rate of change trends in all directions converge. Eventually, observed for sample KB-1c, the Vs rate of change trends in all three directions coincide and follow almost similar trends from ~155 MPa. This is also observed for sample KB-1a, around the same value as for KB-1c. Unloading shows very constant A-Vs rate of change results in all directions until ~100 MPa, followed by increasing rates.

Whereas the results from the Beberthal samples do not seem as conclusive as the Bleurswiller experiments, the results from the hydrostatic stage do show implications for the previously applied maximum stress. Nevertheless, the induced permanent strain for the Beberthal samples after deviatoric loading showed somewhat lower values than the Bleurswiller samples. This supports the idea that higher porosity causes the amount of inelastic deformation of sandstones to increase (*Scott Jr et al. 1993*). Since a clear stress imprint is crucial for the experimental procedure to succeed, an insufficient amount of permanent induced damage could explain the lack of a conclusive deviatoric stress signal during hydrostatic loading. As stated by *Verberne and Spiers (2017)*, differences in basic microstructural properties between the samples, such as grain and pore size, may affect processes controlling inelastic strain accommodation *(Paterson and Wong 2005)*, which could explain the differences between the high-porosity Bleurswiller and low-porosity Beberthal.

4.5 Implications for the reservoir in-situ state of stress

From the P- and S-wave velocity data and corresponding anisotropy values, it is clear that the previously applied maximum deviatoric stress during triaxial loading has left a significant stress imprint which can be retrieved by introducing a hydrostatic stress. Besides stable minimum Vs anisotropy values observed around the previously applied deviatoric stress, both the Vp anisotropy- and Vs anisotropy rate of change reach minimum values approaching zero and following the same trend from 85 MPa. Therefore, the suggested approach to investigate if the in-situ state of stress of the Rotliegend reservoir can be determined by measuring P- and S-wave velocities during true triaxial experiments shows good potential. When applying the procedure on samples from the Rotliegend reservoir of the Groningen gas field, pre-existing core damage is removed during hydrostatic loading, similar to the removal of the induced of the Bleurswiller sample. By introducing a hydrostatic load, the start of the minimum P- and S-wave anisotropy and their corresponding stable minimum rate of change can reveal the in-situ state of stress of the sample due to the minimization of heterogeneities. To further improve the experimental procedure, decreasing the size of the applied stress steps would help to identify the in-situ state of stress more precisely. Furthermore, since the Bleurswiller composition and porosity slightly differs from the Rotliegend sandstone, minor differences in mechanical behaviour and acoustic velocities are expected (*Sayers and van Munster 1991*). Nevertheless, such differences are not expected to be of influence on the efficiency of the approach.

5. Conclusion

The aim of this study is to investigate if the in-situ state of stress of a reservoir can be determined by measuring P- and S-wave velocities during true triaxial experiments. Acoustic wave velocities during triaxial experiments under hydrostatic stress are measured to reveal the stress imprint of the previous deviatoric stress stage. The acoustic data is combined with microstructural- and quantitative analysis to obtain more information about microcrack densities and orientations prior to- and after deformation. Acoustic velocity measurements reveal that specific changes in P- and S-wave velocity and anisotropy are associated with certain changes in the triaxial stress state. Therefore, wave propagations can be used to gain information about the applied stress path. Strain data of the Bleurswiller samples after the deviatoric loading stage reveal that permanent deformation, simulating core damage, has been induced. Whereas microcrack analysis does not show increased crack densities due to extensive inelastic stress-induced microcrack formation, extreme porosity reduction indicates pore collapse as possible responsible mechanisms for most observed inelastic deformation.

When evaluating the acoustic velocity data of hydrostatic stress stage, the data indicates that the maximum stress of the applied deviatoric stress during triaxial loading has left a stress imprint which can be retrieved by introducing a subsequent hydrostatic stress. The stress imprint can be recognized by stable minimum Vs anisotropy and Vp- and Vs anisotropy rate of change values showing minima approaching zero. Applying the same procedure as for the Bleurswiller samples, core damage from a Rotliegend sample can be minimized during hydrostatic loading and the sample state of stress prior to removal can be retrieved. This way, monitoring P- and S-wave velocities and corresponding minimum anisotropy values of a Rotliegend sample during hydrostatic loading can contribute to our knowledge of the in-situ state of stress of the Rotliegend reservoir.

Acknowledgements

I would like to thank my supervisors Suzanne Hangx and Bart Verberne for the great supervision throughout my project. Furthermore, many thanks to Hem Bahadur Motra from the Christian-Albrechts University for the hospitality and help during the true triaxial experiments. Also, I would like to thank Leonard Bik from Utrecht University and Daniel Doran from the University of Southampton for the thin sections preparation which I used in this report. Many thanks also go to the many great people from the Experimental Rock Deformation Group: Mariska Schimmel, Luuk Hunfeld and Ronald Pijnenburg and others, for their great help and feedback I received throughout my project.

References

Baud, P., T. Reuschlé, Y. Ji, C. S. N. Cheung, and T. Wong. 2015. "Mechanical Compaction and Strain Localization in Bleurswiller Sandstone." *Journal of Geophysical Research: Solid Earth* 120:6501–22.

Bernabe, Y. and W. F. Brace. 1990. "Deformation of Berea Sandstone." *"The Brittle-Ductile Transition in Rocks", American Geophysical Union Monograph (Eds A. G. Duba, W. B. Durham, J. W. Handin and H. F. Wang)*.

Browning, J. et al. 2017. "Acoustic Characterization of Crack Damage Evolution in Sandstone Deformed under Conventional and True Triaxial Loading." *Journal of Geophysical Research: Solid Earth* 122(6):4395–4412.

Brzesowsky, R. H. 1995. "Micromechanisms of Sand Grain Failure and Sand Compaction." *PhD Thesis, Utrecht University, Netherlands* 180 pp.

Brzesowsky, R. H., S. J. T. Hangx, N. Brantut, and C. J. Spiers. 2014. "Compaction Creep of Sands due to Time-Dependent Grain Failure: Effects of Chemical Environment, Applied Stress, and Grain Size." *Journal of Geophysical Research : Solid Earth* 119:7521–41.

Doornhof, D., T. G. Kristiansen, N. B. Nogel, P. D. Pattillo, and C. Sayers. 2006. "Compaction and Subsidence." *Oilfield Review* 50–68.

Fortin, J., Y. Guéguen, and A. Schubnel. 2007. "Effects of Pore Collapse and Grain Crushing on Ultrasonic Velocities and Vp/Vs." *Journal of Geophysical Research* 112:1–16.

Fortin, J., A. Schubnel, and Y. Guéguen. 2005. "Elastic Wave Velocities and Permeability Evolution during Compaction of Bleurswiller Sandstone." *International Journal of Rock Mechanics & Mining Sciences* 42:873–89.

Gassmann, F. 1951. "Über Die Elastizität Poröser Medien." *Vierteljahrsschrift Der Naturforschenden Gesellschaft in Zurich* 96:1–23.

Hangx, S. J. T., C. J. Spiers, and C. J. Peach. 2010. "Creep of Simulated Reservoir Sands and Coupled Chemical - Mechanical Effects of CO2 Injection." *Journal of Geophysical Research* 115:1–23.

Hettema, M. H. H., P. M. T. M. Schutjens, B. J. M. Verboom, and H. J. Gussinklo. 2000. "Production-Induced Compaction of a Sandstone Reservoir : The Strong Influence of Stress Path." *SPE Reservoir Evaluation and Engineering* 3(4):342–47.

Hol, S., A. P. Mossop, A. J. van der Linden, P. M. M. Zuiderwijk, and A. H. Makurat. 2015. "Long-Term Compaction Behavior of Permian Sandstones - An Investigation into the Mechanisms of Subsidence in the Dutch Wadden Sea." *ARMA* 15(618).

ISRM. 1979. "Suggested Methods for Determining Water Content, Porosity, Density, Absorption and Related Properties and Swelling and Slake-Durability Index Properties." *International Society for Rock Mechanics*.

Kachanov, M. 1992. "Effective Elastic Properties of Cracked Solids: Critical Review of Some Basic Concepts." *Applied Mechanics Reviews* 45(8):304–35.

Kern, H. 1982. "P- and S-Wave Velocities in Crustal and Mantle Rocks under the Simultaneous Action of High Confining Pressure and High Temperature and the Effect of Rock Microstructure." *High Pressure Researches in Geoscience* 15–45.

Kern, H. 2011. "Measuring and Modeling of P- and S-Wave Velocities on Crustal Rocks : A Key for the Interpretation of Seismic Reflection." *Hindawi Publishing Corporation, International Journal of Geophysics* 2011:9.

Kern, H. and M. Fakhimi. 1975. "Effect of Fabric Anisotropy on Compressional-Wave Propagation in Various Metamorphic Rocks for the Range 20-700C at 2 Kbar." *Tectonophysics* 28:227–44.

Kern, H., B. Liu, and T. Popp. 1997. "Relationship between Anisotropy of P and S Wave Velocities and

Anisotropy of Attenuation in Serpentinite and Amphibolite Hartmut Perature Arid MPa) Are Presented for a Serpentinite and Antigorite and Q Values Increase the Rate of Increase Is Different in." *Journal of Geophysical Research* 102(B2):3051–65.

Kern, H. and H. Wenk. 1990. "Fabric-Related Velocity Anisotropy and Shear Wave Splitting in Rocks From the Santa Rosa Mylonite Zone , California." *Journal of Geophysical Research* 95:213–23.

Mavko, G. 2010. *The Rock Physics Handbook*.

Paterson, M. S. and T. Wong. 2005. *Experimental Rock Deformation - The Brittle Field*.

Peach, C. J. and C. J. Spiers. 1996. "Influence of Crystal Plastic Deformation on Dilatancy and Permeability Development in Synthetic Salt Rock." 256:101–28.

Sayers, C. M. 2002. "Stress-Dependent Elastic Anisotropy of Sandstones." *Geophysical Prospecting* 50:85–96.

Sayers, C. M. and M. Kachanov. 1995. "Microcrack-Induced Elastic Wave Anisotropy of Brittle Rocks." *Journal of Geophysical Research* 100(1):4149–56.

Sayers, C. M. and J. G. van Munster. 1991. "Microcrack-Induced Seismic Anisotropy of Sedimentary Rocks." 96:16,529-16,533.

Sayers, C. M., J. G. van Munster, and M. S. King. 1990. "Stress-Induced Ultrasonic Anisotropy in Berea Sandstone." *International Journal of Rock Mechanics and Mining Sciences & Geomechanics Abstracts* 27(5):429–36.

Schindelin, J. et al. 2012. "Fiji: An Open-Source Platform for Biological-Image Analysis." *Nature Methods* 9(7):676–82.

Schutjens, P. M. T. M. 1991. "Experimental Compaction of Quartz Sand at Low Effective Stress and Temperature Conditions." *Journal of the Geological Society, London* 148:527–39.

Scott Jr, J. R., Q. Ma, and J. C. Roegiers. 1993. "Acoustic Velocity Changes during Shear Enhanced Compaction of Sandstone." *Int. J. Rock Mech. Min. Sci. & Geomech. Abstr.* 30(7):763–69.

Spiers, C. J., S. J. T. Hangx, and A. R. Niemeijer. 2017. "New Approaches in Experimental Research on Rock and Fault Behaviour in the Groningen Gas Fiel." *Netherlands Journal of Geosciences — Geologie En Mijnbouw* 1–15.

van Thienen-Visser, K. and J. N. Breunese. 2015. "Induced Seismicity of the Groningen Gas Field: History and Recent Developments." *The Leading Edge* 34(6):664–71.

Trahwiwit, A. R. 2017. "Integrating Acoustic Measurements and Microstructural Analysis on the Bebertal Sandstone to Predict the State of Stress Before Deformation."

Verberne, B. A. and C. J. Spiers. 2017. "A Quantitative Microstructural Investigation of Depleted and Undepleted Reservoir Sandstones." in *51st US Rock Mechanics/Geomechanics Symposium*.

Walton, K. 1987. "The Effective Elastic Moduli of a Random Packing of Spheres." 35(2):213–26.

Winkler, K. W. and W. F.III Murphy. 1995. "Acoustic Velocity and Attenuation in Porous Rocks." *Rock Physics and Phase Relations - A Handbook of Physical Constants* 20–34.

Wong, T. and P. Baud. 2012. "The Brittle-Ductile Transition in Porous Rock: A Review." *Journal of Structural Geology* 44:25–53. Retrieved (http://dx.doi.org/10.1016/j.jsg.2012.07.010).

Appendices

Appendix 1a – BW-00 mosaic

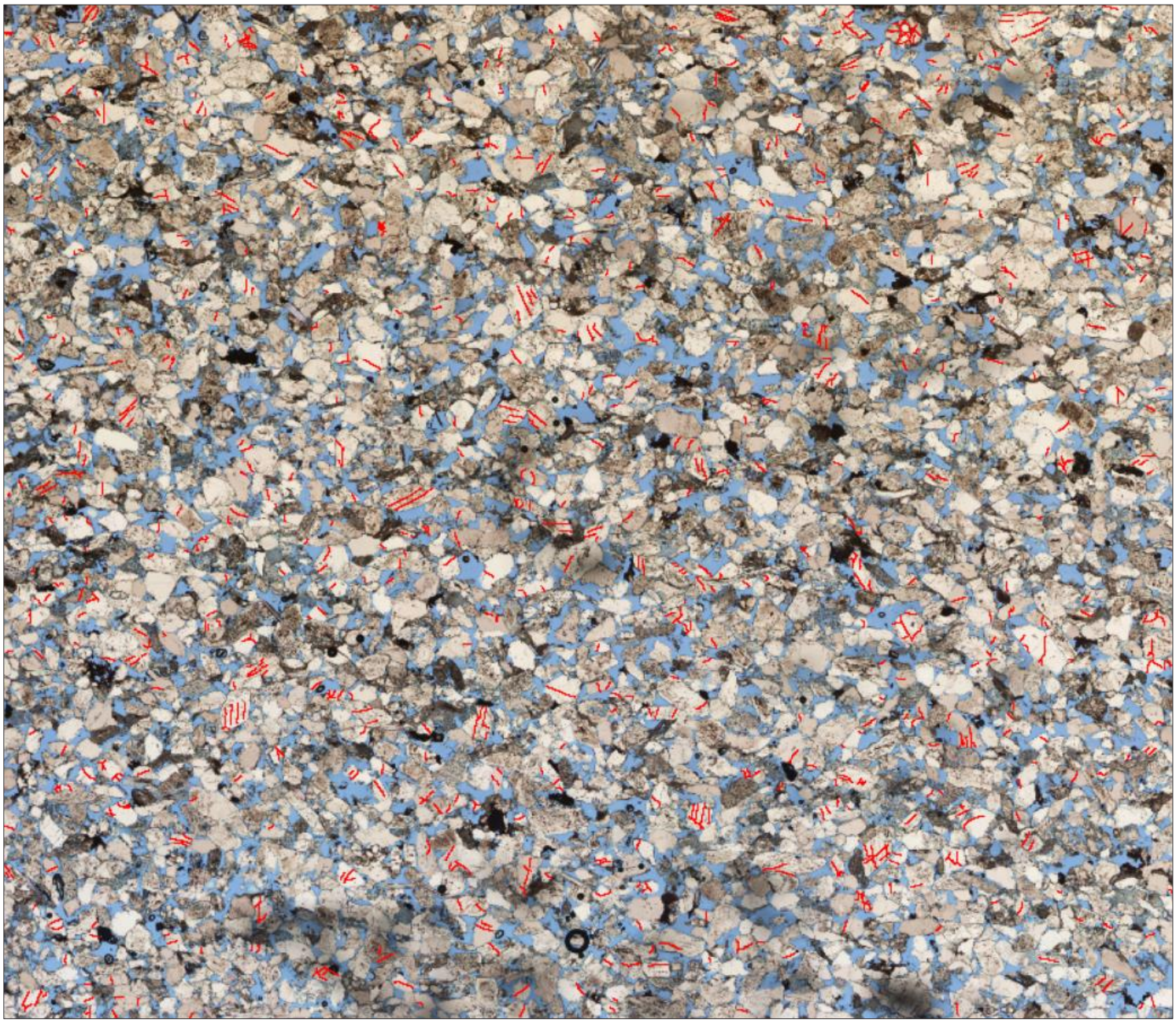

Appendix 1b – BW-02-1-a mosaic

Appendix 1c – BW-02-2-b mosaic

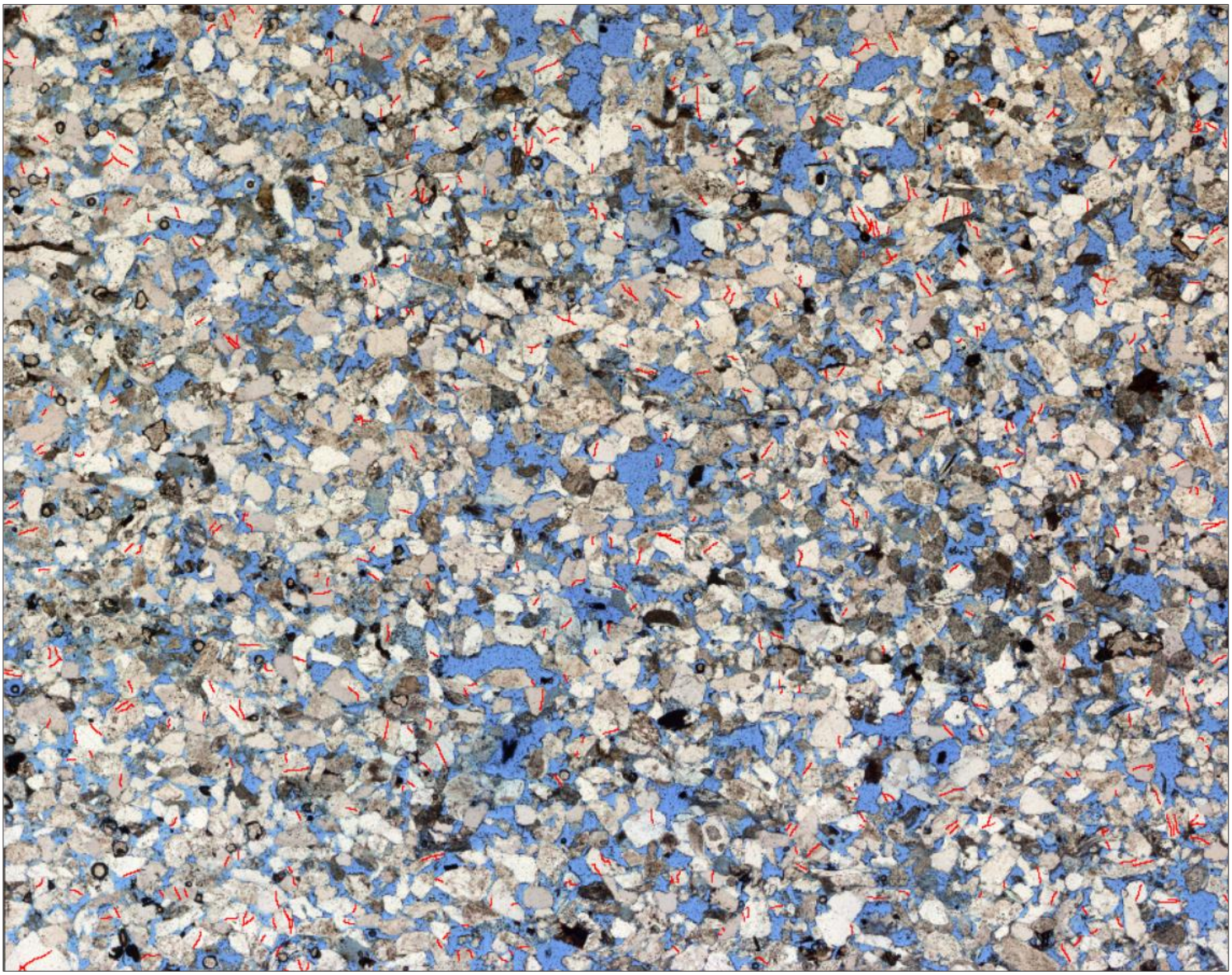

Appendix 2a - Beberthal deviatoric stage: strain- and velocity data

Beberthal data by *Trahwiwit (2017)* of the deviatoric deformation stage: lateral- and volumetric strain data, P- and S-wave velocities during deviatoric loading and unloading.

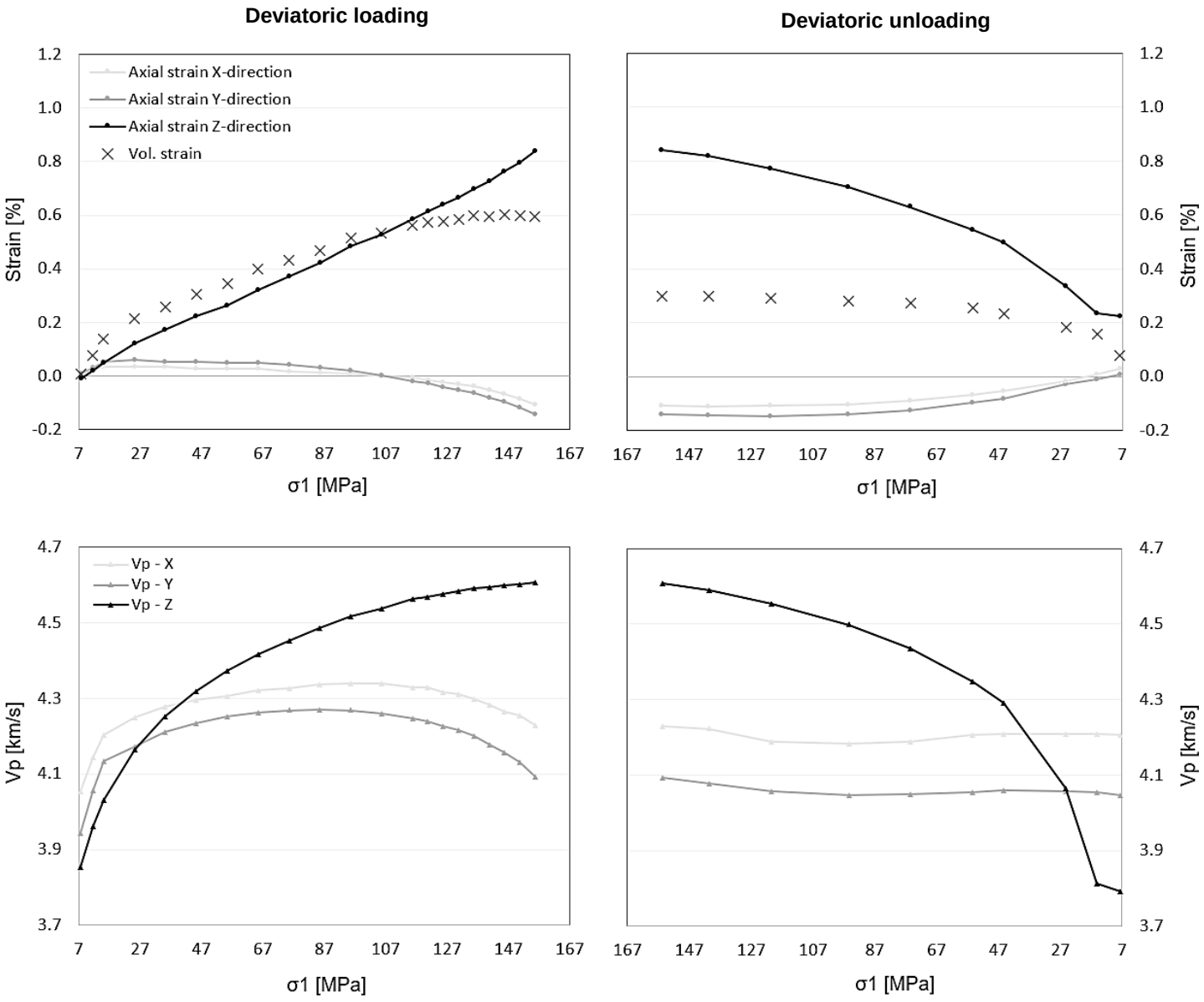

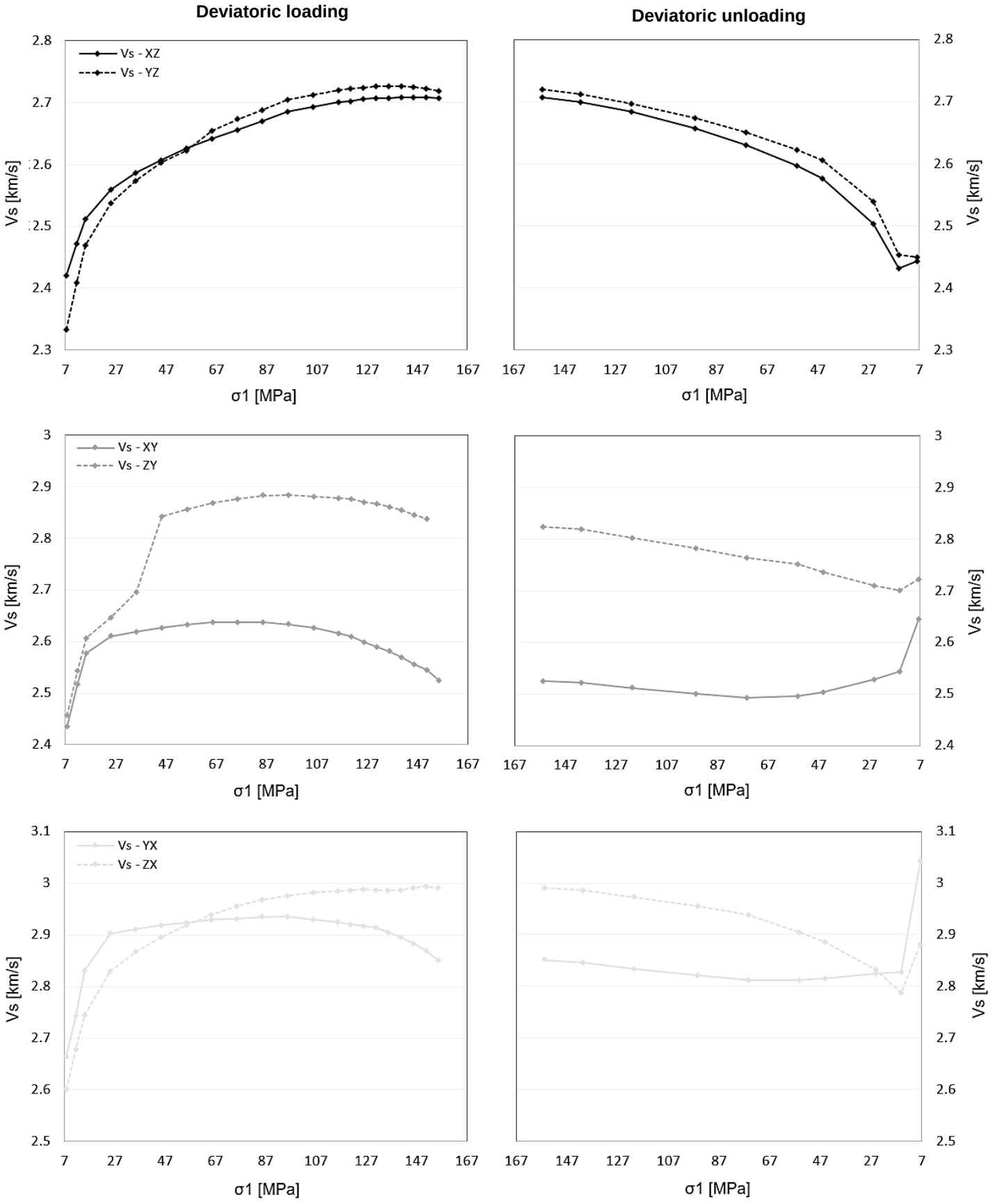
Deviatoric loading
Deviatoric unloading
Vs - XZ
Vs - YZ
Vs - XY
Vs - ZY
Vs - YX
Vs - ZX
Vs [km/s]
σ1 [MPa]

Appendix 2b – Beberthal hydrostatic stage: strain- and velocity data

Beberthal data by *Trahwiwit (2017)* of the hydrostatic deformation stage: lateral- and volumetric strain data, P- and S-wave velocities during hydrostatic loading- and unloading

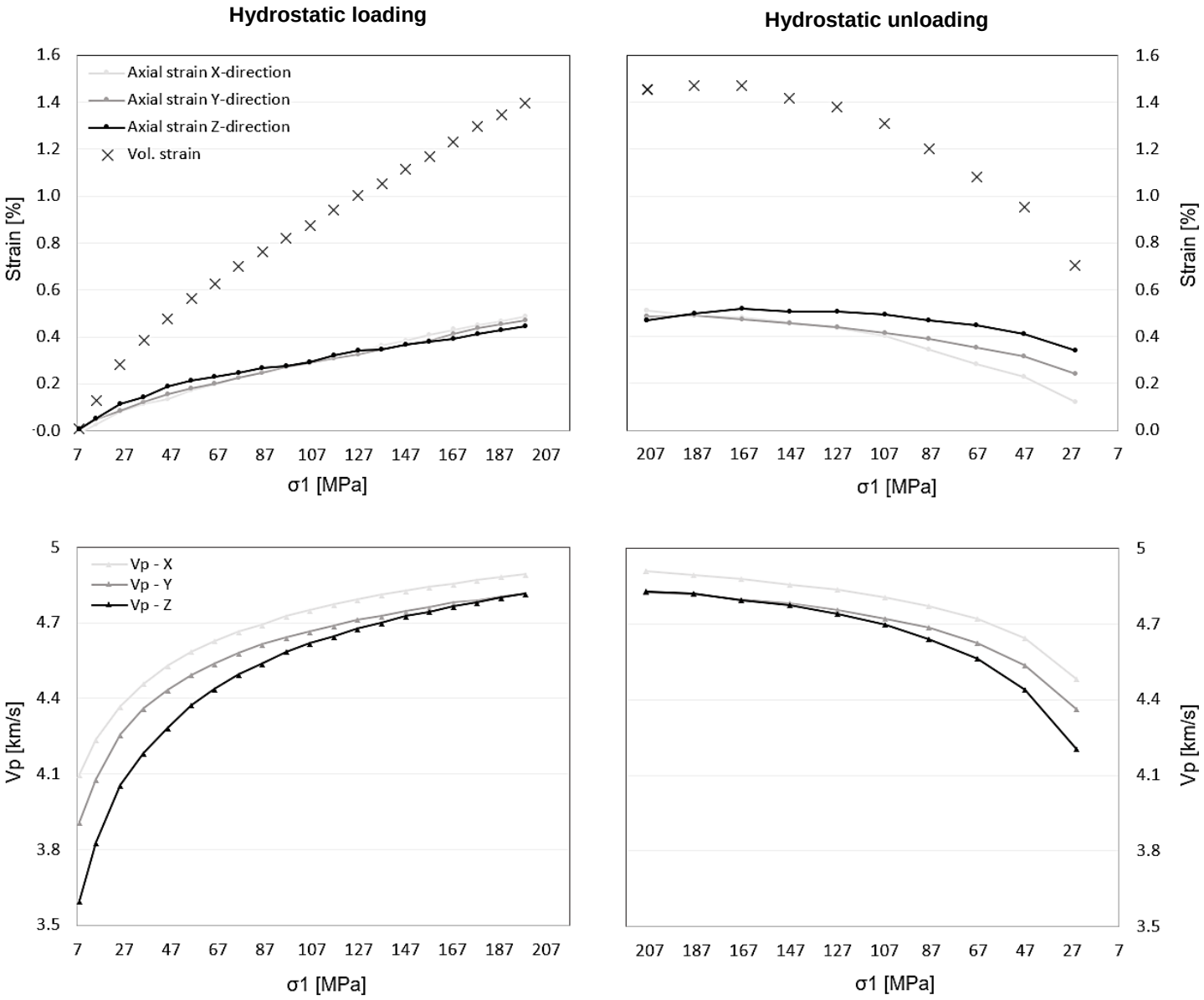

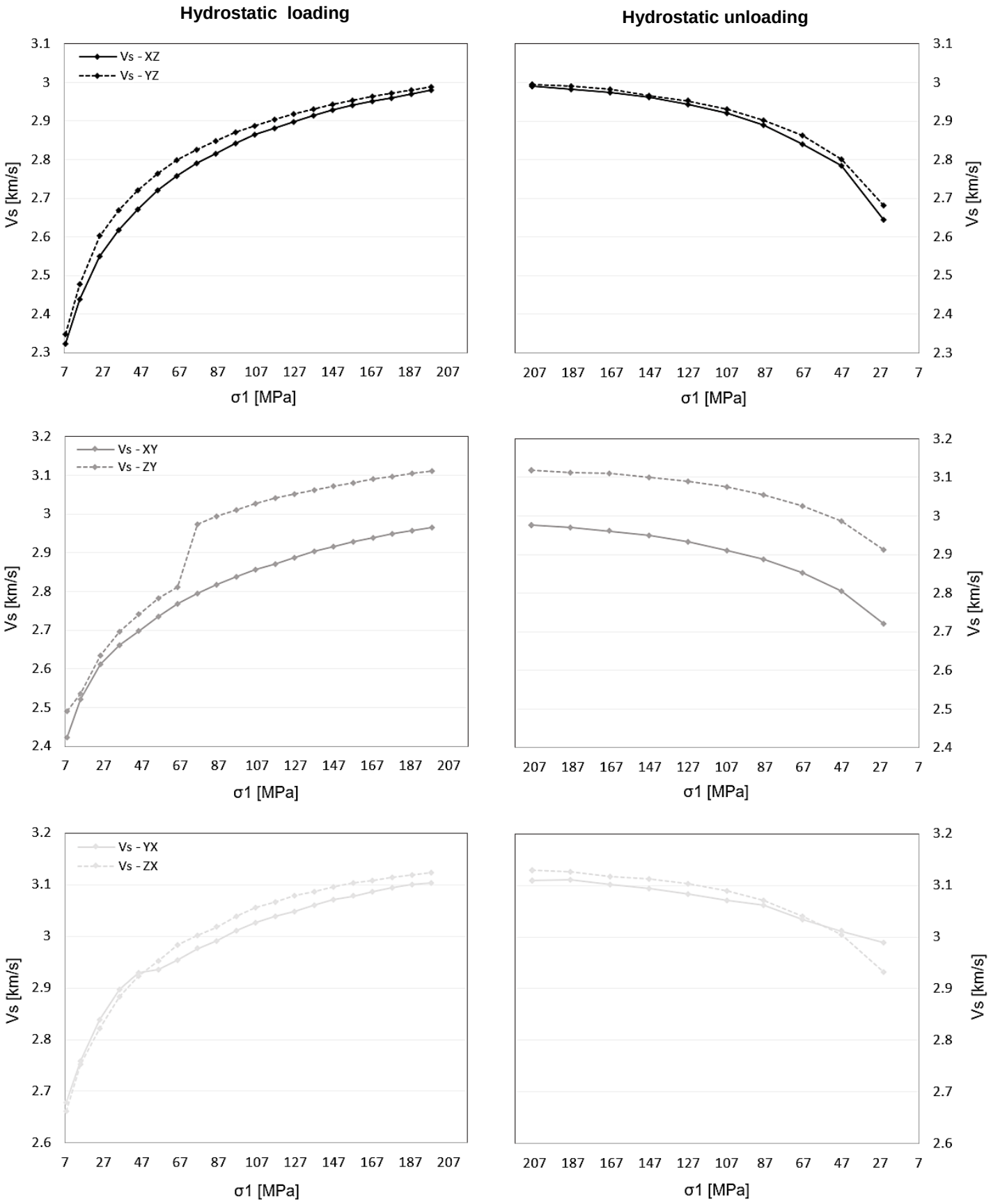
Hydrostatic loading
Hydrostatic unloading
Vs - XZ
Vs - YZ
Vs - XY
Vs - ZY
Vs - YX
Vs - ZX
Vs [km/s]
σ1 [MPa]
3.1
3
2.9
2.8
2.7
2.6
2.5
2.4
2.3
3.2
2.6
7
27
47
67
87
107
127
147
167
187
207